THE ASTROPHYSICAL JOURNAL SUPPLEMENT SERIES, 31:333–415 1976 July

RADIO OBSERVATIONS OF INTERSTELLAR CH. I.

O. E. H. RYDBECK, E. KOLLBERG, Å. HJALMARSON, A. SUME, AND J. ELLDÉR
Research Laboratory of Electronics and Onsala Space Observatory,
Chalmers University of Technology, Gothenburg, Sweden

AND

W. M. IRVINE
Department of Physics and Astronomy, University of Massachusetts
Received 1975 May 19

CONTENTS

ABSTRACT

This paper reports in detail on observations performed at Onsala Space Observatory of the 9 cm CH $^2\Pi_{1/2}$, $J = 1/2$ ground-state hyperfine transitions ($F = 1$–0, upper satellite; $F = 1$–1, main line; $F = 0$–1, lower satellite), in the directions of, and in many cases (marked with *) in extended areas around the following regions: Cas A*, W1*, W3*, Ori A*, W12*, W28 (SNR), W31, W43*, W44 (H II), W49A, W51*, M17, Cyg X* (including, e.g., DR 5, DR 15, DR 21, DR 22), ON 1, ON 2, ON 3 (K3–50), NGC 2068*, NGC 7000*, NGC 7538, L134*, L134 N, L1036, L1082, L1399, L1500*/3C 123, L1630*, Heiles's Clouds 1 and 2*, and the Per OB 2 dust cloud* (including NGC 1333 and IC 348). The observations were made with a traveling-wave maser preamplifier on the Onsala 25.6 m telescope. This gave a zenith system noise temperature of about 34 K.

The CH seems to exhibit weak maser characteristics almost everywhere toward H I and H II regions. Observations on and off 3C 123, which is behind L1500, indicate that the three CH transitions are probably inverted also in dark dust clouds. Absorption (in the main and upper satellite lines) has been observed only toward M17. Significant departures from equilibrium line intensity ratios appear toward H I and H II regions, but generally not for dark dust clouds. Usually the lower satellite transition is enhanced and, toward H II regions with strong far-infrared emission,

is frequently the strongest line. Different alternatives are presented for the interpretation of the observations in Heiles's Cloud 2 (G174.3−13.4), where non-LTE line intensity ratios are found. The CH main line excitation temperature has been determined by observations toward and around Cas A, W12, and 3C 123/L1500, and found to be about −15, −10, and −10 K, respectively. The satellite line transitions are generally more inverted than the main line. The OH 1667 MHz line excitation temperature in the H I clouds toward Cas A has been determined to be about +4 K. The CH observations, together with pertinent information on other interstellar species and far-infrared data on H II regions, are summarized in Tables 1–5. Negative results are contained in Table 6.

Theoretical aspects of the excitation temperature and optical depth calculations are presented. The CH energy level structure of the lowest rotational states is discussed in relation to the excitation of the radical by collisions. The net frequency separation of the ground state doublet is found to be about 3306.5 MHz, yielding the value 0.0551 cm^{-1} for the quantity $p/2 + q$, which contains the molecular parameters p and q. The importance of the first excited rotational state $^2\Pi_{1/2}, J = 3/2$, which has the same parity structure as the ground state, is emphasized. This state may serve as a "population transformer" to give an inversion of the ground state Λ doublet. Suitable far-infrared pumping schemes are proposed, which cause population transfer between the hyperfine levels ($F = 1 \rightarrow 0$) within each half of the CH ground state doublet. "Interlocking" levels in the nearest rotationally excited states are involved. Overlap between the far-infrared transitions connecting the lowest ground-state hyperfine levels seems to be important to account for the observations.

The estimated CH column densities fall in the range 10^{13} to 3×10^{14} cm^{-2} for different regions. The relative abundance of CH with respect to other molecular species seems to diminish systematically from dilute H I clouds to the densest molecular clouds. For example, on the average, [CH]/[OH] ≈ 0.4 for the H I clouds and 0.06 for the molecular clouds. The dark-dust-cloud abundance ratios fit in between these values. The reason for the apparent CH deficiency in the densest clouds may be that the radical is consumed by the formation of the observed, more complex molecules. Existing theories of interstellar CH formation seem to underestimate the CH abundance.

For a more detailed summary the reader is referred to § IX (Summary and Conclusions).

Subject headings: interstellar: molecules — masers — nebulae: general — radio sources: lines

I. INTRODUCTION

The radio astronomical detection of the rotational ground state, $^2\Pi_{1/2}, J = 1/2$, of CH (Rydbeck, Elldér, and Irvine 1973*a*, the complete Λ doublet; Turner and Zuckerman 1974, its upper satellite line) was made only after several unsuccessful attempts in preceding years (cf. Robinson 1967; Rydbeck 1974). The rapid Onsala detection of the entire (generally very weak) Λ doublet was facilitated by approximate precalculations of the hyperfine splittings to be expected (Rydbeck, Elldér, and Irvine 1973*a*). Quite recently Levy and Hinze (1975), using similar methods, have computed these splittings for the nearest excited rotational states. CH was found to be widespread in the Galaxy and was detected in the direction of H I and H II regions as well as in dark dust clouds, with the three allowed hyperfine transitions appearing in emission with very few exceptions (Rydbeck *et al.* 1974*b*; Robinson *et al.* 1974; Gardner and Robinson 1974). Significant departures from equilibrium line intensity ratios appear toward H I and H II regions, and it was established that the CH gas weakly amplifies the background radiation by the maser mechanism. Usually, the lower satellite transition ($F = 0$–1) is enhanced and, toward H II regions, is frequently the strongest line. Far-infrared radiation seems to be correlated with this enhancement. No trace of polarization has been found for any object (Rydbeck *et al.* 1974*b*).

This paper contains the results[1] of more than eight months (1973 October–1974 June) of almost continuous, high-sensitivity observations of the three hyperfine transitions of the CH ground state, performed at Onsala Space Observatory. Some preliminary findings have already been reported briefly (Rydbeck, Elldér, and Irvine 1974*a*; Rydbeck *et al.* 1974*b*), as well as the negative results of the searches at Onsala and Parkes (Rydbeck *et al.* 1974*a*) for CH emission in comet Kohoutek (1973*f*). The main ($F = 1$–1) CH line has been detected in emission from this comet by Black *et al.* (1974).

The rest frequencies of the three ground state transitions have been determined from the radio astronomical observations (Rydbeck *et al.* 1974*c*) to be $\nu_{10}(F = 1\text{–}0) = 3349.193 \pm 0.003$, $\nu_{11}(F = 1\text{–}1) = 3335.481 \pm 0.002$, and $\nu_{01}(F = 0\text{–}1) = 3263.794 \pm 0.003$ MHz. Our later observations indicate that the estimated uncertainties are conservative (cf. the results toward G174.3−13.4 in Heiles's Cloud 2, § IV). Figure 1 depicts the energy levels of the ground state Λ doublet with transitions and frequencies included. The net frequency separation, ν_Λ, of the doublet is $\nu_\Lambda \approx (\nu_{10} + \nu_{01})/2 = 3306.5$ MHz. From this value it is possible to calculate the quantity $p/2 + q = \nu_\Lambda/2$, which contains the important molecular parameters p and q (Mulliken and Christy 1931). We obtain $p/2 +$

[1] A more complete documentation of spectra, etc., is available in Rydbeck *et al.* (1975).

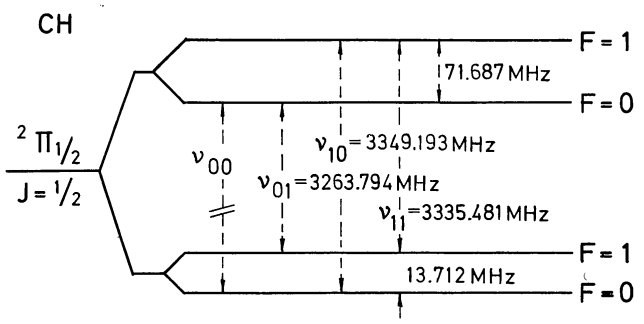

FIG. 1.—The energy levels of the ground state, $^2\Pi_{1/2}$, $J = 1/2$, CH Λ doublet (not drawn to scale). LTE intensity ratios between the allowed transitions are $I(\nu_{11}):I(\nu_{10}):I(\nu_{01}) = 2:1:1$.

$q = 0.0551\ \mathrm{cm}^{-1}$. Hammersley and Richards (1974) found $\nu_\Lambda = 3311$ MHz and $p/2 + q = 0.0552\ \mathrm{cm}^{-1}$ from theoretical calculations, very close to our experimental values.

Figure 2 summarizes the observed directions in which we have detected CH. Black dots indicate approximate positions of the CH clouds (nearby dust clouds have not been marked out).

The outline of this paper is as follows: After a description of the equipment and the observational procedure given in § II, we present the observational results for H I and H II regions in § III, separately from the dark dust clouds in § IV, and the negative results in § V. The different regions are treated in order of increasing galactic longitude, except that the observations toward Cas A and W12 are presented first, since CH excitation temperature determinations were made toward these sources. The Cas A paragraph also describes measurements of the OH 1667 MHz line excitation temperature. Some discussions of the observed and calculated CH properties are also presented in §§ III and IV, and this is developed further in § VI, where the determination of excitation temperatures and optical depths from a theoretical point of view is considered. The CH energy level structure of the lowest rotational state is given in § VII together with a discussion of the excitation of the radical, and the importance of far-infrared radiation to account for the observed anomalies of line intensity ratios. A discussion of the abundance of CH relative to other species is presented in § VIII, and is related to existing theories of CH formation. The results of our observations presented in this paper are summarized in § IX. Finally, § X describes briefly more recent CH observations made at Onsala of dark-dust-cloud–type regions.

II. EQUIPMENT AND OBSERVATIONAL PROCEDURE

The observations were made with the Onsala Space Observatory 25.6 m radio telescope, which at 9 cm wavelength has a half-power beam width of about 15′, an aperture efficiency of 0.44, and a beam efficiency of 0.59. The receiver front end was a rutile traveling-wave maser (Rydbeck and Kollberg 1968; Kollberg 1973), especially built for the CH search. The average zenith total system noise temperature was about 34 K. An antenna temperature of 1 K corresponds to approximately 12 Jy for a point source (neglecting atmospheric effects). The receiver back end for the CH observations consisted of two crystal filter banks, *viz.* 100 contiguous 10 kHz filters and 100 contiguous 1 kHz filters. The first local oscillator frequency was adjusted to compensate for the orbital and diurnal motions of the Earth, the error in frequency always being kept below 100 Hz at 3 GHz. Frequency switching was used, and we switched between 200 and 500 kHz for narrow spectral lines. For more complicated spectra we used a frequency displacement larger than 1 MHz. When using a small distance to the comparison frequency, the spectral lines were centered to appear twice within the 1 MHz band covered by the 10 kHz filters. An improvement of the signal-to-noise ratio was then accomplished by correlation. Using this procedure, peak-to-peak fluctuations less than about 0.05 K would appear in our 10 kHz spectra toward weak continuum sources for integration times of about 1 hour. Switching to the reference frequency band by an amount larger than 1 MHz would result in peak-to-peak fluctuations less than about 0.07 K for the same integration time. Normally, integration times of a few hours were used. A baseline determined by fitting a polynomial of low order was removed from the raw spectra. Since the observed lines are weak and furthermore occupy only a fraction of the post-amplifier filter bank, this baseline generally could be found without the necessity of "off-source" observations.

III. OBSERVATIONS OF H I AND H II REGIONS

Our CH observations of H I and H II regions, listed in order of increasing galactic longitude, are summarized in Table 1 of § III*b*, which also contains abundance data on OH, H_2CO, CO, and H I. Table 2 presents radial velocities and line widths of these and other species, together with distance information. The relations and underlying assumptions used to derive values listed in the tables (e.g., the value −15 K for the main line excitation

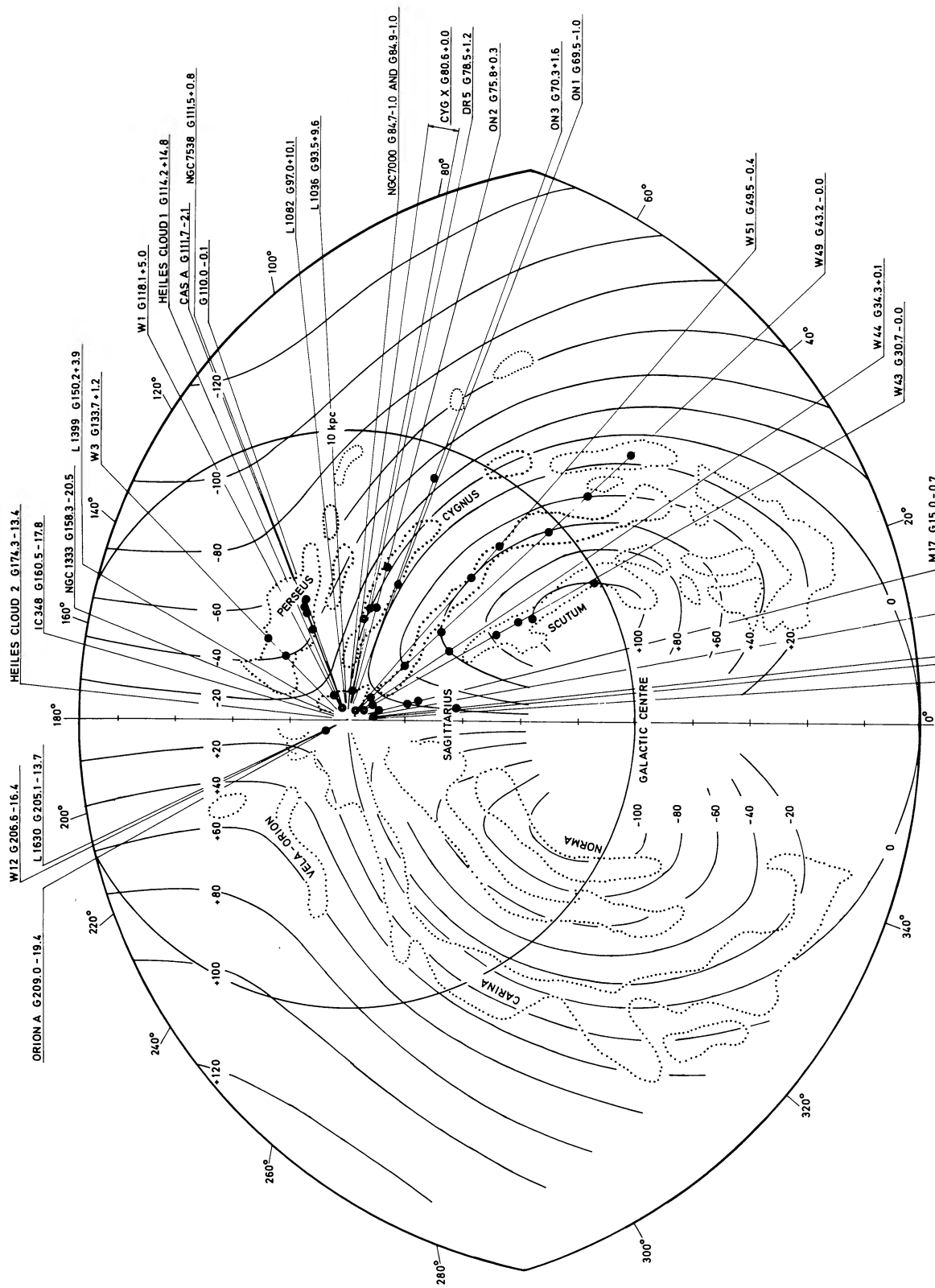

FIG. 2.—The positions of the CH clouds (*circles*) detected in the present paper, projected onto the galactic plane (omitting nearby dark dust clouds). Contours of radial velocity from the circular orbit model of galactic rotation (Schmidt 1965) are included. Dotted contours represent the distribution of neutral hydrogen (map adopted from McGee *et al.* 1967). The direction of each source is marked together with its galactic coordinates. The Sun–galactic center distance is 10 kpc.

temperature) are presented in §§ III*a* (Cas A) and III*b*. A more detailed discussion of the Table 1 and 2 data is left to § III*b*, after our treatment of the individual sources and areas. References to most molecular data are given as footnotes to the tables. In the source descriptions we only refer to molecular data which are directly compared with the CH properties.

a) Individual Sources and Areas

Following our treatments of the Cas A and W12 areas, which include excitation temperature and column-density calculations, the observed regions are discussed in order of increasing galactic longitude. Our CH main line observations toward the low-elevation sources G6.7−0.3 (W28, SNR) and G10.6−0.4 (W31) are given at the end of this section.

i) *G111.7−2.1 (Cas A, 3C 461)*

This well-known supernova remnant of angular diameter about 4′ has an estimated distance of 3.4 kpc and is the strongest 9 cm continuum source in our CH survey. Its optical and radio properties have been reviewed by Minkowski (1968). High-resolution continuum observations of Cas A at 2.7 and 5.0 GHz have been performed by Rosenberg (1970*a*, *b*).

According to Minkowski, the optical extinction in front of Cas A varies from about 3 to 5 mag across the source. Troland and Heiles (1974) estimate the absorption caused by diffuse interstellar dust to be about 3 mag, and believe that the remaining nonuniform component originates in the colder regions of the spiral arms, rather than in higher density regions such as dark clouds. Davies and Matthews (1972) arrive at a similar conclusion.

Absorption lines from H I, OH, and H_2CO, as well as weak emission lines from CO, have been detected from clouds in the Orion (local) and Perseus arms in the direction of Cas A (e.g., Clark 1965; Goss 1968; Zuckerman *et al.* 1970; Davies and Matthews 1972; Wilson *et al.* 1974). The OH main line intensities exhibit the expected

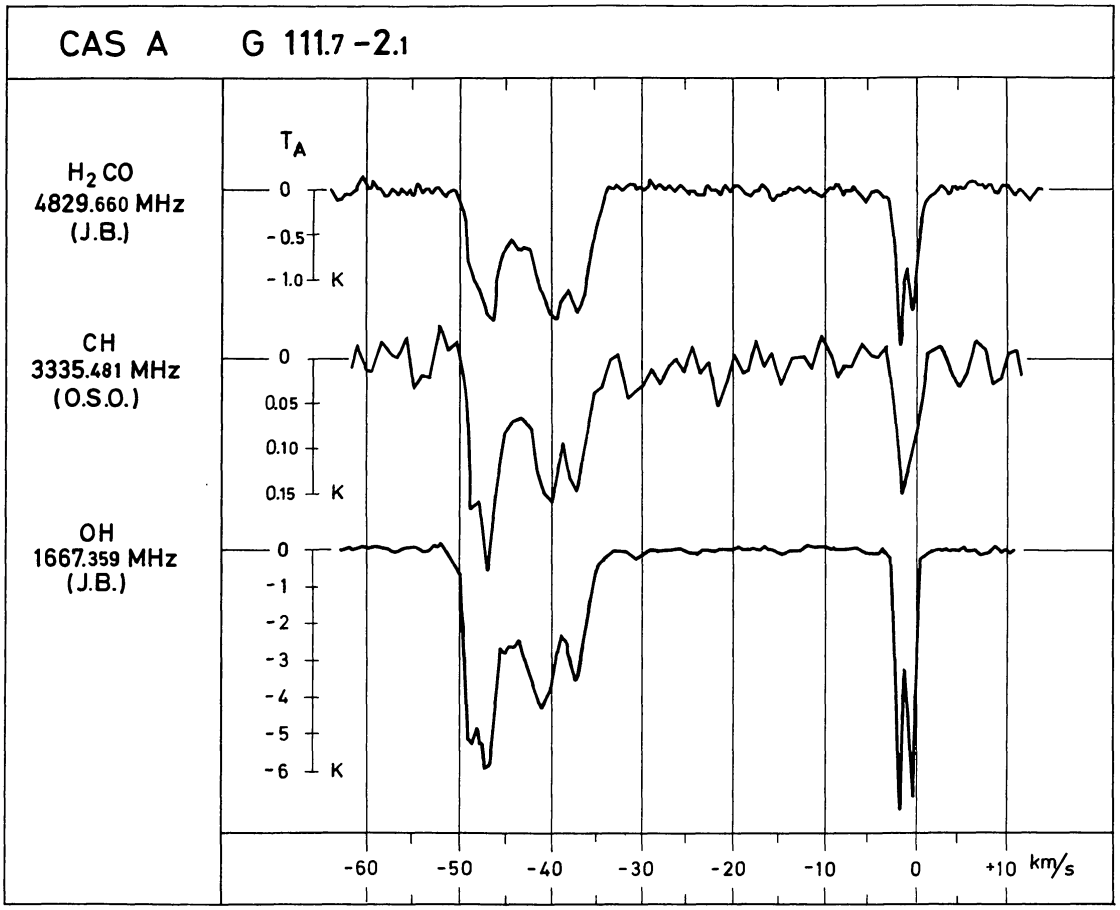

FIG. 3.—Spectra toward Cassiopeia A in the lines of H_2CO (the 1_{11}–1_{10} rotational transition; Jodrell Bank data), CH (the F = 1–1 line of the ground state; Onsala data), and OH (the F = 2–2 line of the ground state; Jodrell Bank data). Velocity scale (LSR) is based on the denoted frequencies. The CH emission profile has been inverted to facilitate comparison with the absorption lines. The Jodrell Bank data were kindly supplied by R. D. Davies.

ratios for the optically thin and LTE case, while the 1612 MHz absorption is too strong and the 1720 MHz absorption too weak (Goss 1968). An anomalous, probably linearly polarized, 1720 MHz OH emission feature from the local arm has also been detected in and possibly around the source direction (Rogers and Barrett 1967; Goss 1968; Turner 1969*a*). Troland and Heiles (1974) mapped the Cas A area in the 6 cm H_2CO line, and found weak absorptions also off the source. The excitation temperature of this line was estimated to lie in the interval 2.4–2.8 K.

The original CH detection was toward Cas A (Rydbeck *et al.* 1973*a*; Turner and Zuckerman 1974), as was the case for OH (Weinreb *et al.* 1963; Barrett, Meeks, and Weinreb 1964). Figure 3 shows 4830 MHz H_2CO and 1667 MHz OH absorption (Davies 1973 and private communication) together with main line CH emission spectra in this direction. The CH spectrum has been inverted to facilitate comparison with the other spectra. The conspicuous agreement in shape for both the Orion and Perseus arms indicates that the molecular species are well mixed in the various clouds in front of the source. Spectra with 10 kHz resolution of the Orion and Perseus arms, and 1 kHz spectra (smoothed to 3 kHz) of the former, are shown for all three CH transitions in Figures 4 and 5, respectively. Velocities and widths of reliable CH features are listed in Table 1, and compared in Table 2 with those of OH, H_2CO, H I, and CO.

We have also detected weak CH emission features at many points around Cas A, from clouds both in the Orion and Perseus arms. The observations indicate inhomogeneities on a scale of 15′, or less. In Figure 6 we have reproduced averages of all spectra (10 kHz resolution) observed in a 24 point grid around Cas A for the three transitions. These weak spectra have been corrected for undesired sidelobe contributions from Cas A. The "clean" line antenna temperature off Cas A was obtained as (for derivations of the relations in this section, see Rydbeck *et al.* 1975)

$$\Delta T_{A,2} = \frac{T_{A,2} - \xi_{21} T_{A,1}}{1 - \xi_{21}}, \tag{1}$$

where $\xi_{21} = T_{CR,2}/T_{CR,1}$. The quantities $T_{CR,1}, T_{A,1}$ and $T_{CR,2}, T_{A,2}$ are the observed continuum temperature above a uniform background and the line antenna temperature, on-source (denoted 1) and off-source (2). $T_{CR,2}$ is assumed to be caused by sidelobe responses only. Figure 6 clearly illustrates the presence of both the Orion and the Perseus arm features in the averaged high-sensitivity spectra. The intensity of the -47 km s^{-1} feature decreases more than the other components off-source, probably indicating that this most distant cloud has a smaller angular extension. A similar behavior is found in the H_2CO mapping around Cas A (Troland and Heiles 1974).

It should be added that small-scale clumping of average size 1′ ($\approx$ 1pc) of the cold neutral hydrogen clouds in the Perseus arm in front of Cas A appears from the interferometer observations by Greisen (1973*a*). Troland and Heiles (1974) suggest a spatial structure on a scale of 4′ or less from their H_2CO observations around Cas A.

The considerable intensity increase of the CH main and satellite line spectra from the Orion and Perseus arm clouds, when observed in the direction of Cas A, clearly demonstrates that CH in all three transitions behaves like a weak maser, amplifying the background radiation. Since the expected line intensity ratio between the satellite lines and the main line is 1:2 for the optically thin case with equal excitation temperatures, the observed spectra (Figs. 4 and 5) indicate unequal excitations of the three transitions. The satellite line enhancement, especially for the lower one, means greater population inversion for these lines.

The on/off Cas A observations offer the most reliable way to estimate the (weak maser) excitation temperatures. This is especially true for the local Orion arm clouds, which most likely are located at a kinematic distance less than about 0.2 kpc (cf. Table 2). The transverse distances between points separated by one beam width (15′) are therefore smaller than 1 pc.

If we assume that the cloud has constant properties over the observed region, we can calculate the excitation temperature from

$$T_x = -\frac{\eta_{21} - \xi_{21}}{1 - \eta_{21}} \frac{T_{CR,1}}{\rho_{10}} + T_B, \tag{2}$$

where $\eta_{21} = T_{A,2}/T_{A,1}$ and $\xi_{21} = T_{CR,2}/T_{CR,1}$ are the ratios between observed antenna temperatures off and on source center, for line and continuum, T_B is the brightness temperature of the diffuse background ($\approx$3 K), and $\rho_{10} = (F_1 R_1 \tau_1)/(R_0 \tau_0)$, where R_0, R_1 and τ_0, τ_1 are mean clumping factors and optical depths over the continuum source (denoted 0) and the cloud within the antenna beam, centered on the source (denoted 1). The quantity $F_1 = \epsilon_M \Omega_{CL}/\Omega_M$ is the beam dilution factor (ϵ_M is the beam efficiency, Ω_{CL} and Ω_M are the cloud and antenna main beam solid angles); cf. Goss (1968). We assume that $\rho_{10} \approx \epsilon_M \approx 0.6$, i.e., the cloud fills the main beam.

For the main line we find from the "on" spectrum in Figure 4, the average "off" spectrum in Figure 6, and the observed Cas A continuum antenna temperature above diffuse background, $T_{CR,1} = 85$ K with $\xi_{21} = 0$, that the excitation temperatures become $T_x = -16$ K, -16 K, and -6 K, for the -1 km s^{-1} Orion arm and the -37 km s^{-1} and -47 km s^{-1} Perseus arm features, respectively. The first value should be the most reliable one, since the

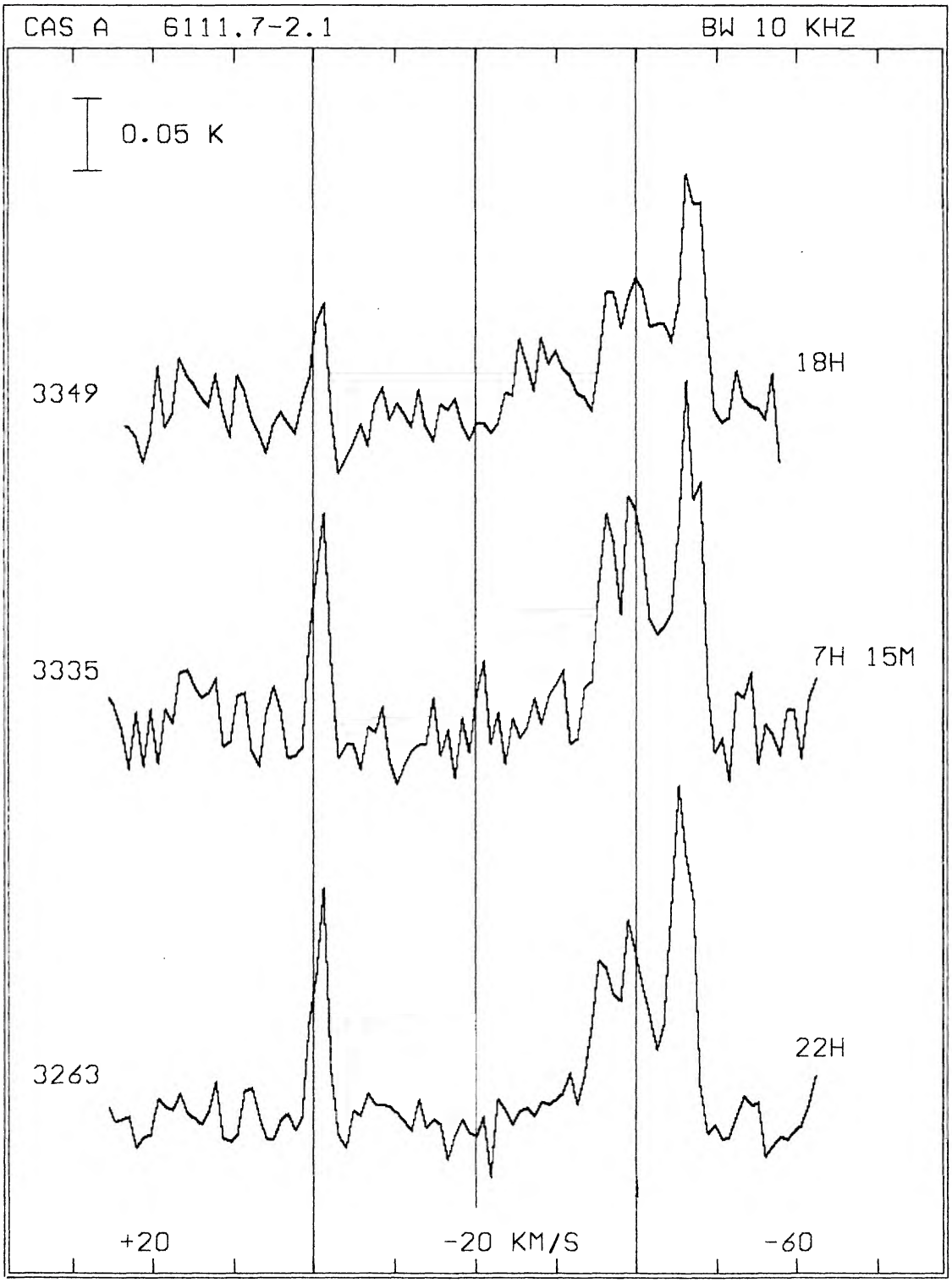

FIG. 4.—CH spectra for the three transitions toward Cas A. The spectra are identified by the transition frequencies in MHz. The source identification, with galactic coordinates, the frequency resolution, the antenna temperature scale, and the integration times are also given in the Figure. This representation will be used for most of our CH spectra.

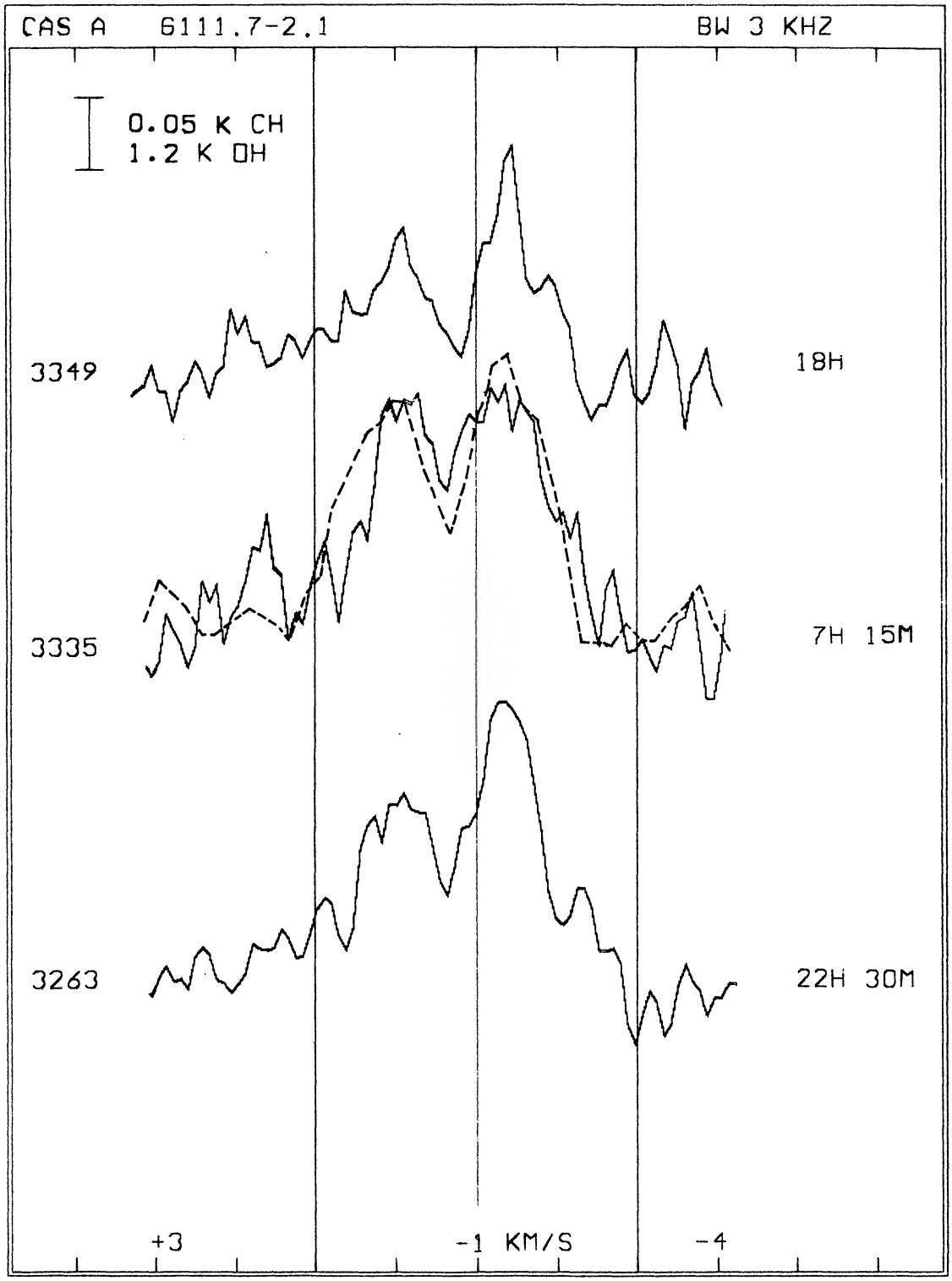

FIG. 5.—CH spectra at 3 kHz of the Orion spiral arm features toward Cas A. Note that at this resolution the CH Orion arm spectra show the same double feature as the OH 1667 MHz line (*dashed line*, entered inverted and scaled for shape comparison. The OH integration time is 10^m).

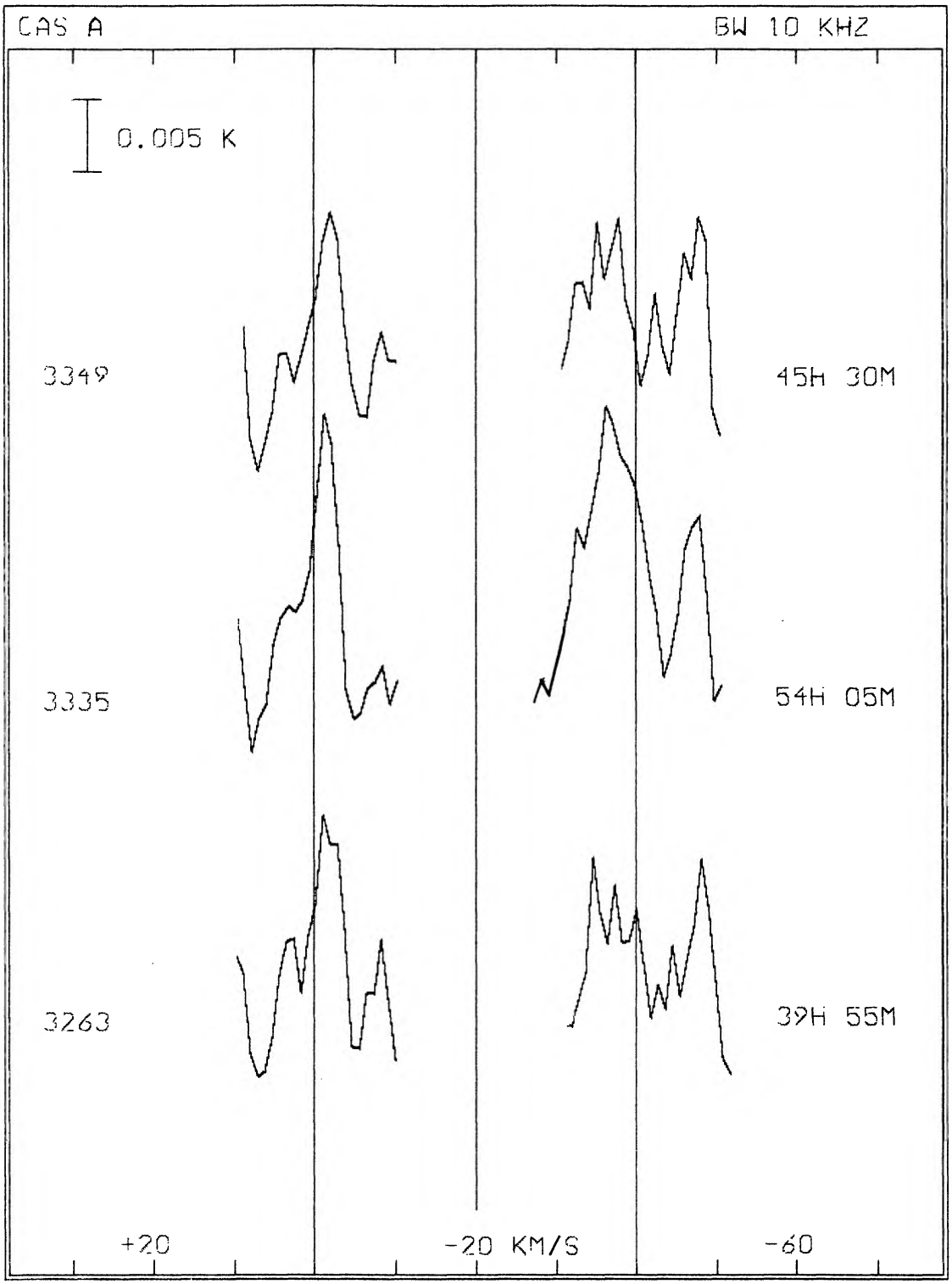

FIG. 6.—Average of 10 kHz CH spectra for the Orion and Perseus arms in the 24 points around Cas A, from a 5 × 5 point grid, with 15′ spacing centered on the Cas A continuum maximum.

assumption of constant cloud properties probably holds better for the local arm clouds. The last value, therefore, may reflect column density variations of the order of 50 percent.

Another estimate of the main line excitation temperatures has been obtained by observations at four half-power continuum positions (about 7'.5 N, S, E, W) around Cas A. We find from equation (2) with $\xi_{21} = 0.5$, and an average of the four main line spectra smoothed to 30 kHz, that $T_x = -29$ K for the -1 km s^{-1} feature, whereas the -37 and -47 km s^{-1} features yield positive excitation temperatures. These estimates are inherently more uncertain, however, since small position errors when the strong source is on the slope of the main beam will cause considerable deviations of $T_{\mathrm{CR},2}$ from the desired value $T_{\mathrm{CR},1}/2$. Furthermore, the signal-to-noise ratio was lower than for the averaged off-source spectra.

We adopt $T_x = -15$ K as a reasonable value for the CH main line excitation temperature, which means a relative population difference ($h\nu/2kT_x$) of about 0.5 percent. For small optical depths the excitation temperatures of the upper and lower satellite transitions can then be estimated from our on source observations (Figs. 4 and 5) by

$$\frac{T_{A,s}}{T_{A,m}} \approx \frac{1}{2}\frac{1 - T_{tb}/T_{x,s}}{1 - T_{tb}/T_{x,m}} \left(\approx \frac{1}{2}\frac{T_{x,m}}{T_{x,s}} \text{ for } T_{tb} \gg |T_{x,m}|, |T_{x,s}|\right), \tag{3}$$

where s and m denote satellite and main line quantities and $T_{tb} = T_B + T_{\mathrm{CR},1}/\rho_{10}$. The average values obtained (assuming $\rho_{10} = 0.6$) for the excitation temperatures of the different velocity components are -10 K and -8 K for the upper and lower satellite transitions, respectively (see Table 1).

The uncertainties in our on/off source determination ($\xi_{21} = 0$) of the main line excitation temperature can be discussed by means of the following relation:

$$T_x = -\frac{\eta_{21}}{\rho_{21} - \eta_{21}}\frac{T_{\mathrm{CR},1}}{\rho_{10}} + T_B, \tag{4}$$

where $\rho_{21} = (F_2R_2\tau_2)/(F_1R_1\tau_1)$ (roughly equal to the ratio between the average off-source and on-source column densities). If we assume that the probability distributions of the measured quantities η_{21} and $T_{\mathrm{CR},1}$ are Gaussian, with estimated standard deviations of 25 and 10 percent, the observational rms uncertainty becomes about ± 5 K. The actual values of ρ_{21} and ρ_{10} are unknown, however. A reasonable guess is that the denominator of equation (4) may deviate less than 50 percent from the assumed value. In view of these considerations we adopt as a conservative estimate

$$T_x = -15(+10, -30\ \mathrm{K}), \tag{5}$$

for the CH main line excitation temperature. A similar value is obtained toward the H II region W12 (see next subsection).

According to relation (3), the uncertainties of the satellite line excitation temperatures for Cas A are essentially determined by the error of the main line excitation temperature. They are therefore uncertain by a factor of about 3. The ratio between the excitation temperatures is rather accurate, however, with an rms uncertainty of about 20 percent.

Table 1 also lists on-source optical depths at line center for the three transitions, calculated by means of the relation

$$\tau_{\max} = \frac{T_{A,\max}}{R_0[\rho_{10}(T_x - T_B) - T_{\mathrm{CR},1}]}, \tag{6}$$

where we assume that $R_0 = 1$ (no clumping) and $\rho_{10} = 0.6$. The calculated opacities are of the order of -10^{-3}. This clearly demonstrates the weak maser action.

The total column densities in the $^2\Pi_{1/2}$, $J = 1/2$ state of the various velocity features are also presented in Table 1. They have been estimated from the main line transition by means of the relation

$$N_{\mathrm{CH}} = 2.9 \times 10^{14}\frac{T_x \int T_A(v)dv}{R_0[\rho_{10}(T_x - T_B) - T_{\mathrm{CR},1}]}\ \mathrm{cm}^{-2}, \tag{7}$$

which contains the $F = 1$–1 Einstein A coefficient of Burdyuzha and Varshalovich (1973). The integrals (km s^{-1} K) have been determined by means of a planimeter. With $R_0 = 1$, $\rho_{10} = 0.6$, and $T_x = -15$ K, we obtain CH column densities of the order of 10^{13} cm^{-2} for the individual velocity components toward Cas A.

We furthermore find by relation (4) that the ratio between off- (2) and on-source (1) column densities is roughly $N_2/N_1 \approx 9\eta_{21}$. Our mapping of the Orion and Perseus arms (Rydbeck *et al.* 1975) then suggests column density variations of a factor of 2 or more.

To estimate the accuracy of the determination of N_{CH}, we note that by equations (4) and (7),

$$N_{CH} = 2.9 \times 10^{14} \frac{-T_x(1 - \eta_{21}/\rho_{21})}{R_0 T_{CR,1}} \int T_A(v)dv\,, \tag{8}$$

where $R_0 \leq 1$.

The uncertainty of the integral is about 10 percent. Therefore the error bounds of N_{CH} are determined mainly by the uncertainty of T_x. Thus the lower limit of $N_{CH}(R_0 = 1)$ is uncertain by a factor of about 3. The uncertainty of the lower limit of the optical depth is much less, however, since, by equations (4) and (6),

$$\tau_{max} = \frac{-T_{A,max}(1 - \eta_{21}/\rho_{21})}{R_0 T_{CR,1}}\,. \tag{9}$$

With a standard deviation of 10 percent in $T_{A,max}$, the observational rms error of τ_{max} becomes about 15 percent.

Even if the clumping factors, $R_0 \leq 1$, are not known, they should be approximately the same for CH, OH, and H_2CO in the Cas A region, where these species seem to be well mixed (see Fig. 3 and Table 2). This means that the accuracy of the abundance ratios of these molecules is determined mainly by that of the excitation temperatures. We find from Table 1 with $T_{x,CH} = -15$ K, $T_{x,OH} = +4$ K (see next paragraph), and $T_{x,H_2CO} = +2$ K (Troland and Heiles 1974), that

$$N_{CH}/N_{OH}/N_{H_2CO} = 1/4/0.1\,, \tag{10}$$

with very small variations between the five velocity features. Since definitely $T_{x,H_2CO} < 3$ K (H_2CO is only observed in absorption around Cas A), we may safely conclude that CH is much more abundant than H_2CO in the Orion and Perseus arm clouds. The OH abundance is of the same order of magnitude as that of CH, perhaps somewhat higher (this depends upon the excitation temperature of OH, which is quite uncertain in this particular case, as appears from the following paragraph).

The 1667 MHz OH *line excitation temperature.*—We have also searched for the 1667 MHz line of OH in a nine-point grid with a 30′ spacing centered on Cas A. In the average of the eight off-source 10 kHz resolution spectra (corrected for sidelobe effects as in the CH measurements), no feature greater than 0.02 K was seen. As the on-source peak OH absorptions are about 3.3 K for both the Orion and Perseus arm features, we obtain by equation (2) with $T_{CR,1} = 185$ K and $\rho_{10} = 0.6$ the following OH 1667 MHz line excitation temperature, $T_x = T_B \pm 2$ K. However, in a point 45′ southwest of the continuum source there is a definite weak emission feature ($T_A \approx 0.05$ K) at a velocity of about -3 km s^{-1}. If we compare this emission peak with the on-source absorption line at about -1 km s^{-1}, we find by equation (2) that $T_x = T_B + 5 \pm 2$ K. However, the fact that this peak is seen in one point only, and at a different velocity, implies that the assumption of constant cloud properties inherent in equation (2) is of doubtful value in this particular case. We therefore believe that $T_x = T_B \pm 4$ K is the better estimate. Its uncertainty is due to possible inhomogeneities as well as to observational errors.

The value of T_B must be taken as the sum of the cosmic background (≈ 3 K) and the nonthermal galactic continuum background brightness temperature. For the Orion arm the latter is estimated to be about 1 K from data by Berkhuijsen (1972), if the spectral index is assumed to be 2.9 (cf. Heiles 1969; Turner 1973). Thus we find from our on/off observations that the excitation temperature of the OH 1667 MHz transition is likely to be about +4 K, in good agreement with the estimates toward W12 (Manchester and Gordon 1971; Goss *et al.* 1975).

ii) *G205.3−14.3 (NGC 2068, M78); G206.6−16.4 (W12, Orion B, NGC 2024); L1630*

This area generally coincides with the very extended diffuse dark nebula L1630 (Lynds 1962). It is bordered in the southwest by the Horsehead Nebula and IC 434, and in the northeast by an emission nebulosity, Barnard's loop. The continuum source W12 (Ori B, NGC 2024) lies in the southwestern part of this elongated region, while the reflection nebulae NGC 2068 and 2071 lie about 2° northeast of W12. The area may be one of intense star formation, containing many T Tauri and late B stars, several small emission knots, and Herbig-Haro objects (see Tucker, Kutner, and Thaddeus 1973; Strom *et al.* 1975). The continuum emission from W12 is confined to a small symmetric region, only a few arc minutes in extension (Schraml and Mezger 1969; Goss and Shaver 1970). Distance estimates vary from 0.4 to 0.7 kpc. W12 is also a source of far-infrared radiation (Harper and Low 1971; Emerson, Jennings, and Moorwood 1973; Harper 1974; Grasdalen 1974).

The OH absorption lines in W12, depicted in Figure 7, have the largest optical depths known outside the galactic center; the strongest feature occurs at about +10 km s^{-1}, with a weaker line at about +13 km s^{-1} (cf. Goss 1968; Manchester, Robinson, and Goss 1970). The 6 cm formaldehyde transition in Figure 7 shows a similar double feature with velocities of about +9 and +13 km s^{-1} (cf. Zuckerman *et al.* 1970). H I absorption is seen at about +10 km s^{-1} (Radhakrishnan *et al.* 1972*b*). The hydrogen recombination line velocities fall around +5 km s^{-1}, whereas the carbon recombination and molecular line velocities equal +10 km s^{-1} (cf. Table 2). Emission has been found from H_2O (weak, see Fig. 7), SO, CS, C_2H, HCN, U89.2, and U90.7 toward W12, and also from CO and OH over the entire L1630 region (Tucker, Kutner, and Thaddeus 1973; Johansson *et al.* 1974 and private communication).

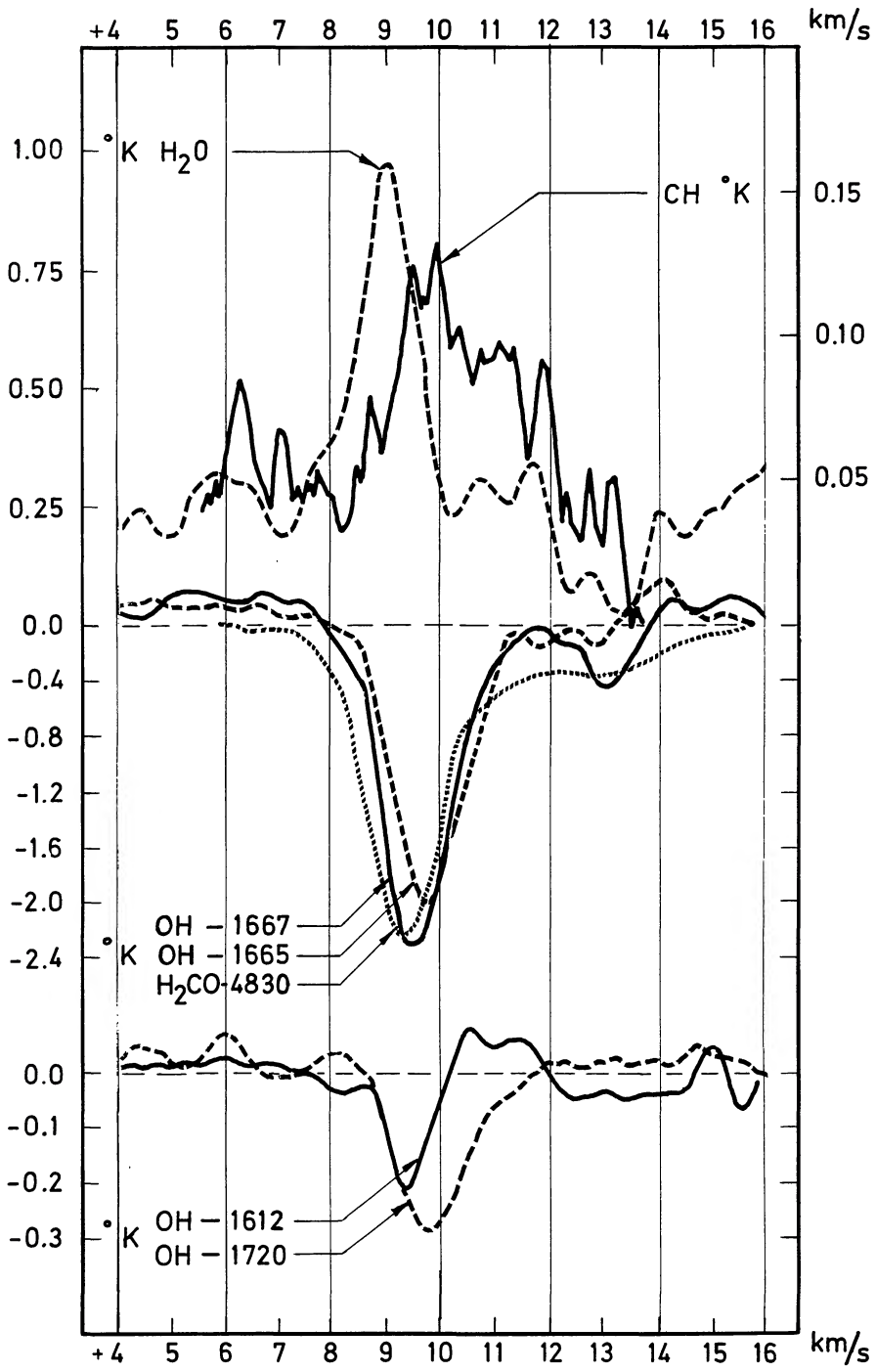

FIG. 7.—OH, H_2CO, and H_2O (weak) spectra (from Yngvesson *et al.* 1973, 1975) and a CH main line, 3 kHz resolution spectrum toward W12 (G206.6–16.4).

We find fairly broad CH emission in the velocity range +3 to +13 km s^{-1} toward selected regions of the L1630 cloud (Figs. 8 and 9), occasionally appearing as two separate peaks.

In the direction of W12 there appears a narrow, strong feature at about +10 km s^{-1} (Fig. 9). All three CH lines show a maximum intensity here, with the lower satellite anomalously strong (Figs. 8 and 9). At higher resolution (3 kHz), the main line appears to consist of several components (see Fig. 7). These results suggest that we see CH in an extended region along the line of sight, apparently divided into a number of more or less distinct

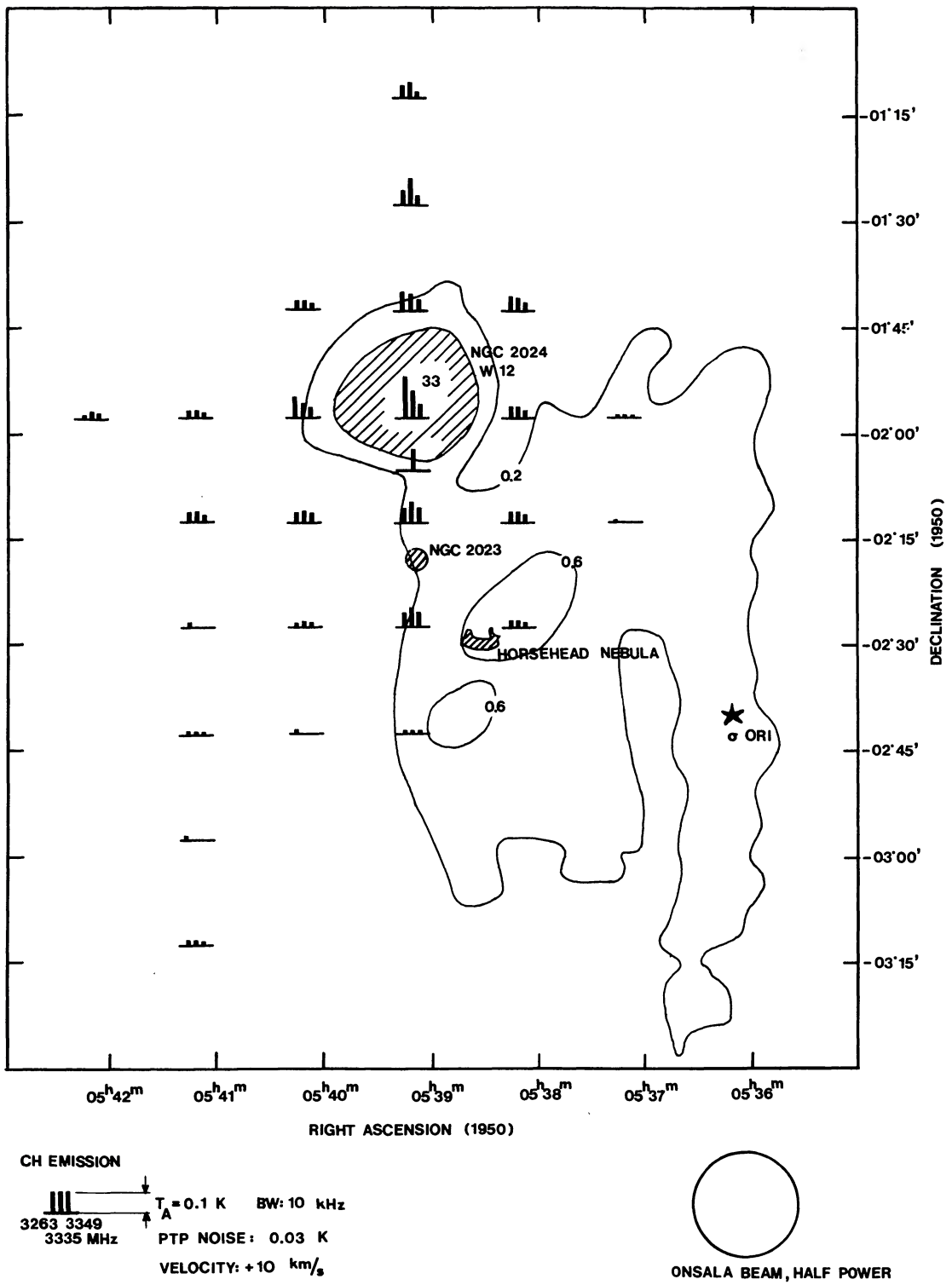

FIG. 8.—CH peak antenna temperatures, represented by bars, in the W12 region at about +10 km s^{-1}. The three CH lines are identified with the bars as shown at bottom left. Observations of all three lines were made only at points where three bars are indicated. The contours represent continuum brightness temperatures (K) at 2.7 GHz (from Caswell and Goss 1974). The positions of the reflection nebula NGC 2023, the Horsehead nebula, and the exciting star, σ Ori, of IC 434 are also shown.

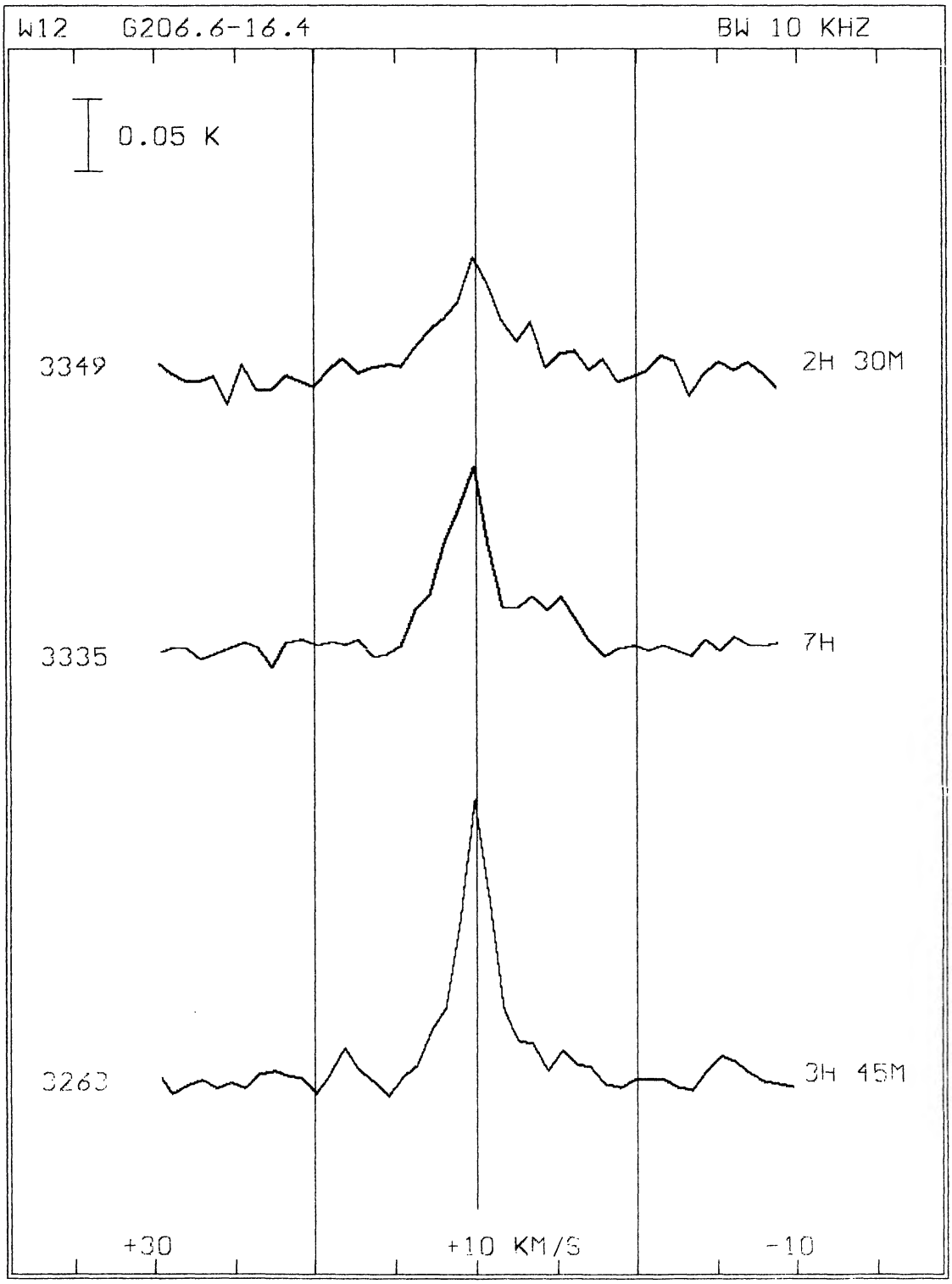

FIG. 9.—CH spectra toward W12

clouds. The $+10$ km s^{-1} CH cloud appears to lie in front of the radio continuum source, amplifying the background radiation. This should also be the case for the weak component at about $+13$ km s^{-1}. Both velocities have counterparts in OH and H_2CO absorptions (see Fig. 7), as well as H I absorption (Greisen 1973*b*).

The narrow, $+10$ km s^{-1} feature is visible at several points around W12 and also toward NGC 2068 and at five points (observed in the main line only) at and around the position of maximum OH emission in the L1630 dust

cloud, about 45′ northeast of NGC 2068 (Johansson, private communication). Toward NGC 2068 the velocity equals about +11 km s^{-1}, in agreement with the OH velocity and the H_2CO velocity observed by Dieter (1973) in the opaque dark dust cloud L1627 close to this source. The narrow CH features in the direction of NGC 2068 are approximately in the LTE ratio, and may arise from L1627. A dense cloud has also been found centered about 15′ southwest of NGC 2068, at a velocity of +10 km s^{-1}, and mapped in the 2 mm H_2CO line (Lada *et al.* 1974*b*). HCN was also detected in this region.

Our observations also show that CH and CO (Tucker, Kutner, and Thaddeus 1973; Milman 1974) coexist in approximately the same velocity range in Lynds's cloud L1630. The intercomparison of spectra is difficult due to the very different antenna beams used. However, the appearance of a strong and sharp CO peak in the direction of NGC 2068 and at the velocity of the narrow CH feature should be mentioned. The location of the maximum CO emission coincides with the position of the reflection nebula NGC 2023, where Morris *et al.* (1974*a*) found HCN at +10 km s^{-1}. Our CH spectra 15′ south of W12 (cf. Fig. 8) do not appear to be influenced by NGC 2023, although it lies within the beam.

Because of its relative simplicity and small distance ($\approx$0.5 kpc; 15′ corresponds to about 2 pc in the transverse direction), W12 offers a possibility to estimate the excitation temperature of CH in front of the continuum source by a comparison of the measurements on and around the source (as was done for Cas A). For this purpose we must assume that the cloud has the same properties in front of and near the source.

By relation (2) we find from the on-source spectrum ($T_{CR,1}$ = 5 K), from the four spectra 15′ N, E, S, W (cf. Fig. 8) of W12 ($T_{CR,2}$ = 0.5, 0.1, 0.6, and 0.5 K, respectively), with T_B = 3 K and ρ_{10} = 0.6, the T_x values −10, −4, −25, and −1 K for the main line, with a mean of −10 K. This scatter in T_x reflects inhomogeneities of the gas in the region. If we express the inhomogeneities in terms of column density variations, we find from relation (4) that the ratio between off- and on-source column densities is $N_2/N_1 \approx 1.5\eta_{21}$. Such inhomogeneities are clearly demonstrated by Figure 8. At a point 30′ N of the continuum maximum, for example, the main line is as strong as on-source. Moreover, 7.5 and 15′ south of W12 the main line has an intensity which is about 80 percent of the on-source value. This and similar results of Robinson *et al.* (1974) indicate a CH column density increase south of the continuum maximum (cf. also the NGC 2024 model by Grasdalen 1974).

In view of the additional uncertainties of the excitation temperature determination due to the inhomogeneities, the T_x value derived here may be regarded as being in agreement with the value −15 K obtained from the Cas A observations. We will therefore adopt this value for the CH main line in all H I and H II regions studied in this paper. The satellite line excitation temperatures can then be estimated from relation (3), by means of the on-source spectra only. Toward W12 we find T_x = −10 K and −3 K for the upper and lower satellite transitions (cf. Table 1). In this case the latter is 5 times more inverted than the main line (cf. Cas A and § III*b*).

The CH column density toward W12 equals about 1.5 × 10^{14} cm^{-2} (cf. Table 1). CH column densities for most of our sources are compared in this Table with those of OH, H_2CO, CO, and in some cases H I, and are discussed in § III*b*.

We draw attention to the fact that the lower satellite line generally is strongly enhanced when seen toward a region of intense far-infrared radiation. This is apparent from Figure 8. A mechanism of population transfer between the Λ doublet levels which leads to such an enhancement is discussed in § VII. Such enhancements are common in many of the H II regions surveyed by us.

iii) *G15.0−0.7 (M17, W38, NGC 6618, Omega Nebula)*

This bright H II region is located in a complex area of radio and optical emission as well as optical obscuration (Dickel 1968). Radio continuum measurements at 15 GHz reveal two strong main components separated by about 4′ (Schraml and Mezger 1969). Hydrogen recombination lines are found around +18 km s^{-1} with a width of about 40 km s^{-1} (McGee and Gardner 1968; Wilson *et al.* 1970*b*; Reifenstein *et al.* 1970), possibly consisting of two components (Gull and Balick 1974). Carbon recombination lines occur at about +24 km s^{-1}. The distance is estimated to 2.5 kpc. M17 is also a strong, two-component far-infrared source (Harper and Low 1971; Hoffman, Frederick, and Emery 1971; Lemke and Low 1972; Rieke *et al.* 1973; Harper 1974).

Our observations were performed toward M17 SW, located approximately 1′ from the southern continuum maximum, at the position of a molecular cloud with CO, SO, NH_3, CS, C_2H, HCN, and H_2CO millimeter wave emission. The 6 cm H_2CO transition as well as the OH ground state are seen in absorption in this direction. Furthermore, an H_2O maser and a strong infrared point source have been detected in this area (cf. Table 2; Lada, Dickinson, and Penfield 1974*a* and references therein; Lada and Chaisson 1975). According to Lada and Chaisson there is evidence of extensive mass motions near M17 SW, which may be a region where star formation is in progress.

Our CH profiles (Fig. 10) toward M17 SW are among the most complex that we have observed for any source. A narrow emission feature for all three lines appears at about +24 km s^{-1}. There is also a broad absorption in the main line and the upper satellite, centered at about +15 km s^{-1}, and strong, anomalously enhanced lower satellite emission with maximum amplitude at about +20 km s^{-1}.

When observed with 1 kHz resolution (see Fig. 11, which depicts 1 kHz spectra smoothed to 3 kHz), the narrow emission feature at +24 km s^{-1} exhibits velocity patterns that are different for the three hyperfine components.

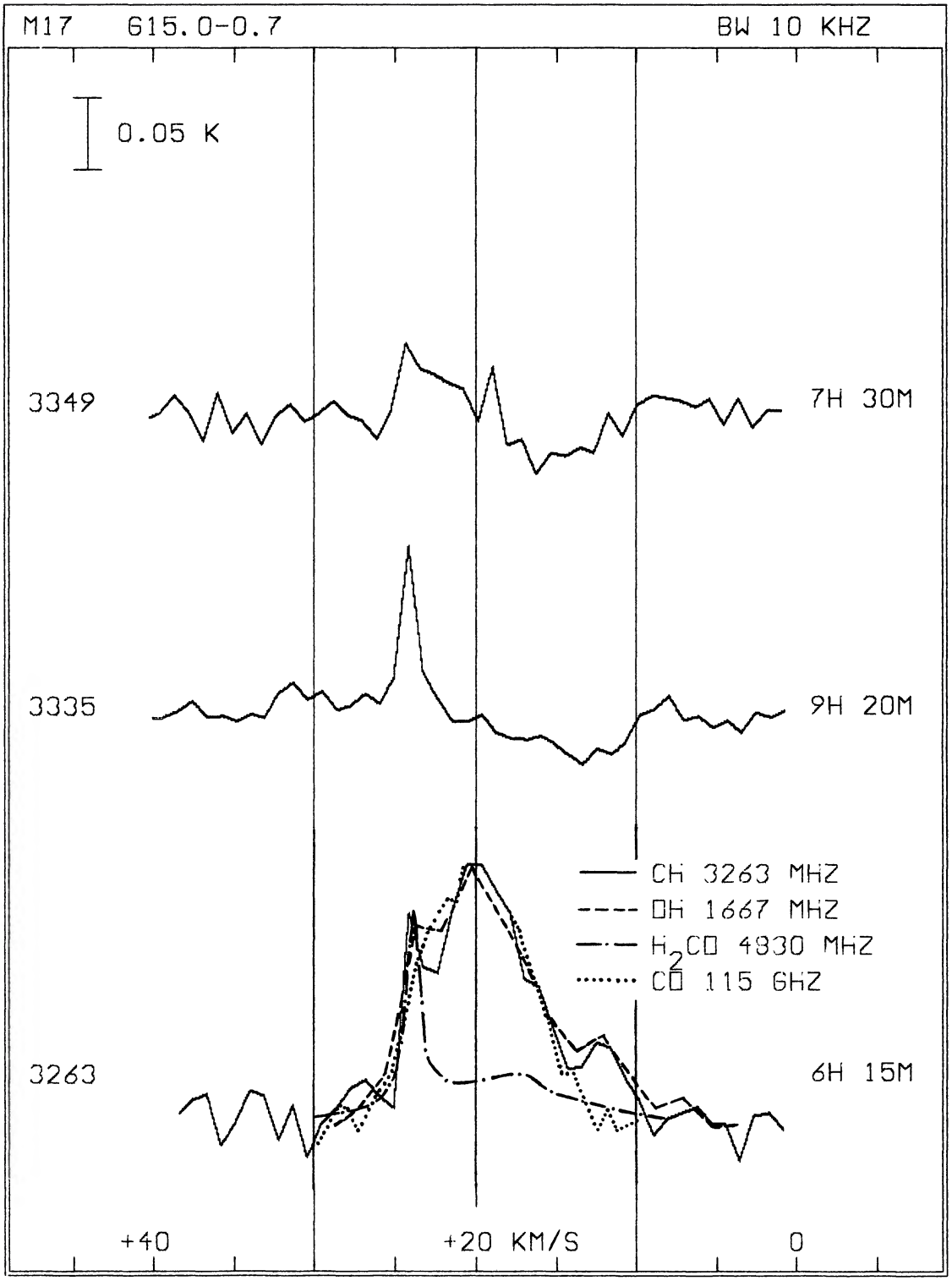

FIG. 10.—CH spectra toward M17 with normalized spectra of the OH 1667 MHz main line absorption (Gardner and McGee 1971), the H_2CO 4830 MHz line absorption (smoothed spectrum from Lada and Chaisson 1975), and the CO 115 GHz line emission (Lada *et al.* 1974*a*) superposed on the CH 3263 MHz lower satellite line. The OH and H_2CO profiles have been inverted to facilitate comparison with the emission spectra.

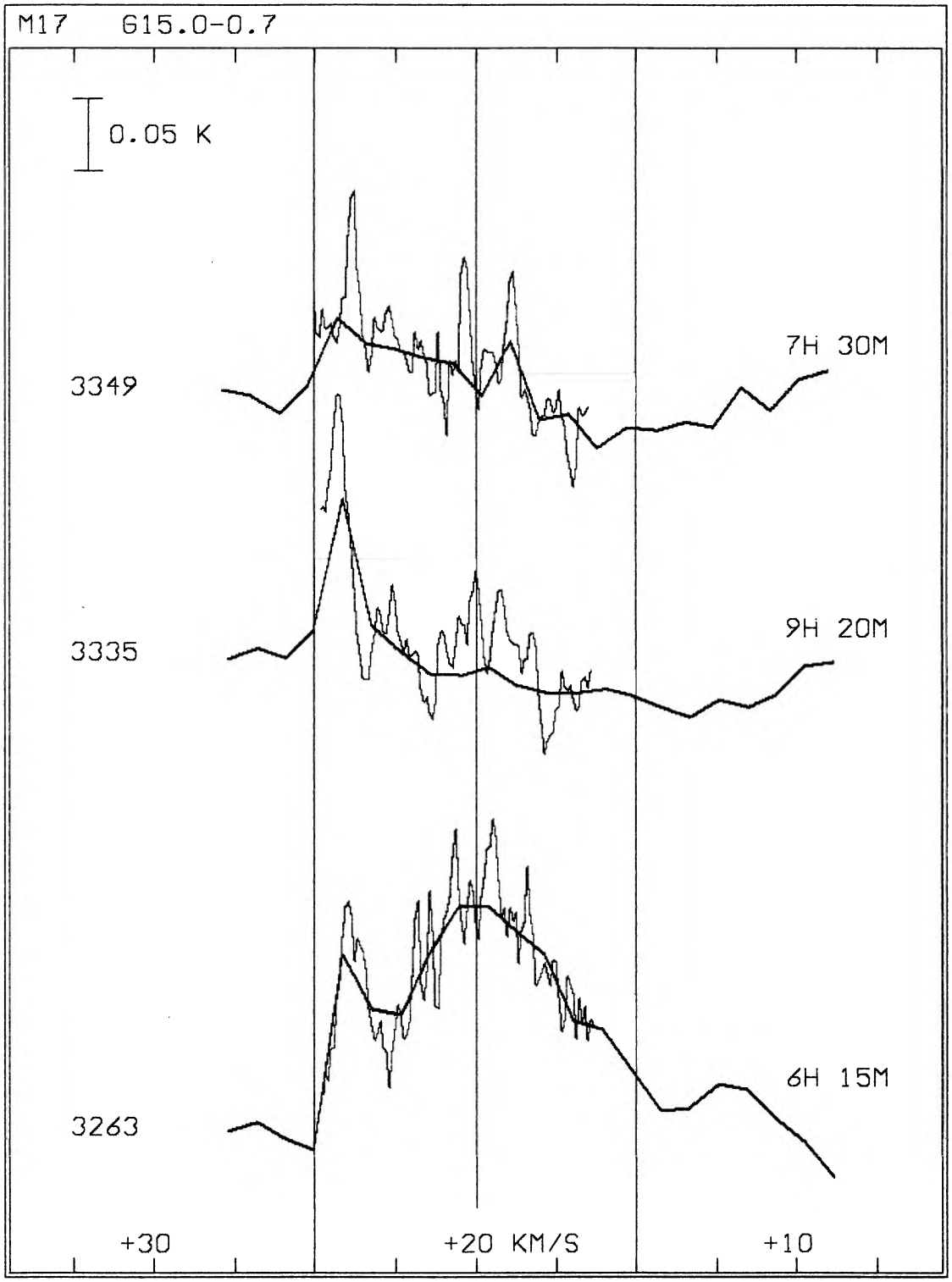

FIG. 11.—Spectra at 3 kHz (*light lines*) superposed on 10 kHz spectra (*heavy lines*) toward M17

This suggests the presence of even finer velocity structures (possibly indicating clumping on a scale small compared with our beamwidth). The 3349 MHz line in particular is by far the narrowest feature (width $\lesssim 0.3$ km s^{-1} as measured with 1 kHz resolution, corresponding to a temperature less than 30 K) that we have observed for any source, including the dark dust clouds. The 3263 MHz feature is definitely much broader (width ≈ 1 km s^{-1}) than the 3349 MHz and 3335 MHz spectra, probably because of anomalous lower satellite line emission. There is a

narrow (width ≈ 0.9 km s^{-1}), intense 6 cm H_2CO absorption at about $+24$ km s^{-1} (Zuckerman *et al.* 1970; Lada and Chaisson 1975), which is indicative of a pronounced daser effect in a foreground dust cloud. Figure 10 depicts the 6 cm H_2CO profile (inverted) obtained by Lada and Chaisson superposed on the CH lower satellite spectrum. Assuming that the narrow peak at about $+24$ km s^{-1} in the three CH lines emanates from the same cloud, a comparison with the corresponding H_2CO feature yields CH rest frequencies just within the error bounds given by Rydbeck *et al.* (1974*c*).

In Figure 10 we also illustrate the close agreement between the shapes of the strong CH lower satellite emission spectrum in the velocity range $+10$ to $+25$ km s^{-1} and the (inverted) strong 1667 MHz OH absorption profile (Gardner and McGee 1971). It thus appears that CH and OH are well mixed in the clouds in front of the H II region. The broad component in the spectral region $+15$ to $+25$ km s^{-1} probably originates in the "molecular cloud," since the line profile is quite similar to that of CO (also depicted in Fig. 10), SO, H_2CO (140 GHz), and HCN (Lada, Dickinson, and Penfield 1974*a*). The 6 cm H_2CO absorption spectra obtained by Lada and Chaisson (1975) have a corresponding broad but weak feature (see Fig. 10), which, they propose, may originate from infalling gas in the outer layers of the molecular cloud. Our high-resolution spectra (Fig. 11) indicate the presence of several discrete emission features centered around $+20$ km s^{-1} in all three CH transitions, which for instance form the "shoulder" to the $+24$ km s^{-1} peak of the upper satellite line in Fig. 10.

The feature at about $+12$ km s^{-1} (shown in Fig. 10) in the OH and the lower satellite CH profiles is also found in 6 cm H_2CO absorption (Whiteoak and Gardner 1970), but is not seen in the millimeter molecular emission line spectra.

A particularly unusual aspect of our profiles for M17 is the broad (width ≈ 7 km s^{-1}) absorption present in both the main and upper satellite lines and centered at about $+15$ km s^{-1}. These weak absorptions have been established by careful, long integrations, including different frequency-switching schemes and with different centering of the profiles in the filter bank. This is the only CH absorption feature which we have found; it is similar to the CH absorption reported for RCW 38 by Robinson *et al.* (1974). These authors found main line absorption at a velocity slightly lower than that at which strong, anomalous lower satellite emission and weaker upper satellite emission occur; upper satellite absorption was not, however, apparent for RCW 38. For both M17 and RCW 38 the OH spectra are similar, in that the 1612 MHz line shows weak absorption and emission features, while the other three OH lines appear in absorption in the same velocity range, the 1720 MHz line being anomalously strong.

It is possible that the emission features indicated by our high-resolution spectra in the velocity range $+18$ to $+23$ km s^{-1} mask absorption in this range and hence shift the absorption maxima toward lower velocities. It would indeed be expected that the maximum absorption should occur at the same velocity as the enhanced lower satellite, since we believe that one and the same pumping process causes the lower satellite enhancement and the absorption in the other two lines (cf. RCW 38 in Robinson *et al.* 1974). Absorption at about $+15$ km s^{-1} might also be present for the 3263 MHz line, producing the local emission minimum at that velocity. Note that both OH and H I have a minimum optical depth at this velocity (Gardner and McGee 1971; cf. Fig. 10).

Another, perhaps more likely, interpretation could be that the weak CH absorptions around $+15$ km s^{-1} are associated with the lower satellite feature at $+12$ km s^{-1}, and are generated in a region separate from the molecular cloud (the $+20$ km s^{-1} feature). In this context it should be remembered that there are two compact radio and infrared components within the antenna beam in the direction of observation.

iv) *G30.7−0.0 (W43 region)*

The radio source complex W43 lies in a heavily obscured region of the galactic plane which makes optical observations impossible. It apparently lies near the tangential point of the Scutum spiral arm (Radhakrishnan *et al.* 1972*b*) at a distance of about 7 kpc. A strong central H II region (G30.7−0.0) and a number of weaker ones are superposed on a large extended area of emission (Goss and Shaver 1970; see Fig. 12). The central source has recently been resolved into a number of compact components at 2.7 GHz (Turner *et al.* 1974*a*). A far-infrared source (100 μ) has been associated with G30.7−0.0 (Hoffman *et al.* 1971). At 12.6 μ this source was found to be multiple in nature (Pipher, Grasdalen, and Soifer 1974), in rough agreement with the radio map by Turner *et al.* A number of molecular lines have been observed toward this source, from OH, H_2O, NH_3, and CO in emission, and OH and H_2CO in absorption (see Table 2).

We find low-velocity ($+5$ to $+17$ km s^{-1}) CH emission in all observed directions (for observation points see Fig. 12). The peak emission occurs at slightly higher velocities ($\sim +12$ km s^{-1}) in the northern part of the area than in the southern ($\sim +7$ km s^{-1}). Main line OH absorption is also found at velocities of about $+7$ and $+12$ km s^{-1}, with the former feature strongest toward G29.9−0.0 (Goss 1968; Robinson, Goss, and Manchester 1970; Goss *et al.* 1973; Onsala unpublished data). Six cm H_2CO absorption has been found at $+7$ km s^{-1} for G29.9−0.0 (Wilson 1972), and at $\sim +14$ km s^{-1} for G30.7−0.1 (Zuckerman *et al.* 1970). Similar features occur in the H I spectra (Radhakrishnan *et al.* 1972*b*). This gas is apparently local, at a distance of less than 1 kpc.

Weak OH, H_2CO, and H I features also occur in the velocity interval $+20$ to $+70$ km s^{-1}, where CH emission is faint or absent.

Our observations at higher velocities include the five points indicated in Figure 12. The lower satellite is enhanced in all observed directions, but the anomaly is particularly strong toward G30.6−0.0 and G30.7−0.0 (Fig. 13) for

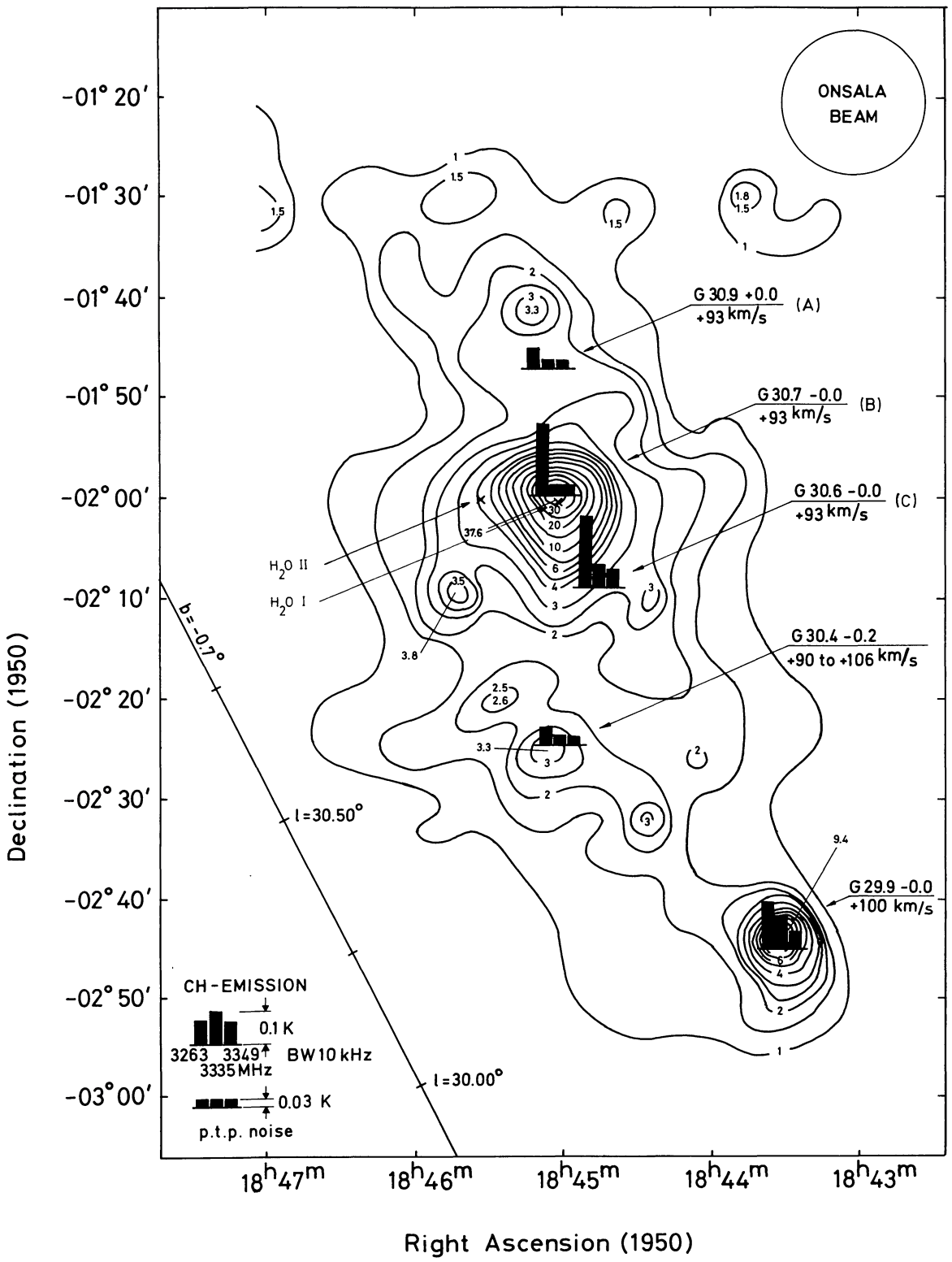

FIG. 12.—A 5 GHz continuum map (from Goss and Shaver 1970) of the W43 region, with bars representing CH peak antenna temperatures. The contour unit is 1 K brightness temperature. The three CH lines are identified with the bars as shown at bottom left. The velocities of the observed CH peaks have been entered under the galactic coordinates. The source notations A, B, and C are adopted from Robinson *et al.* (1970). The positions of the recently resolved H_2O sources (Cato *et al.* 1975) have also been marked on the map.

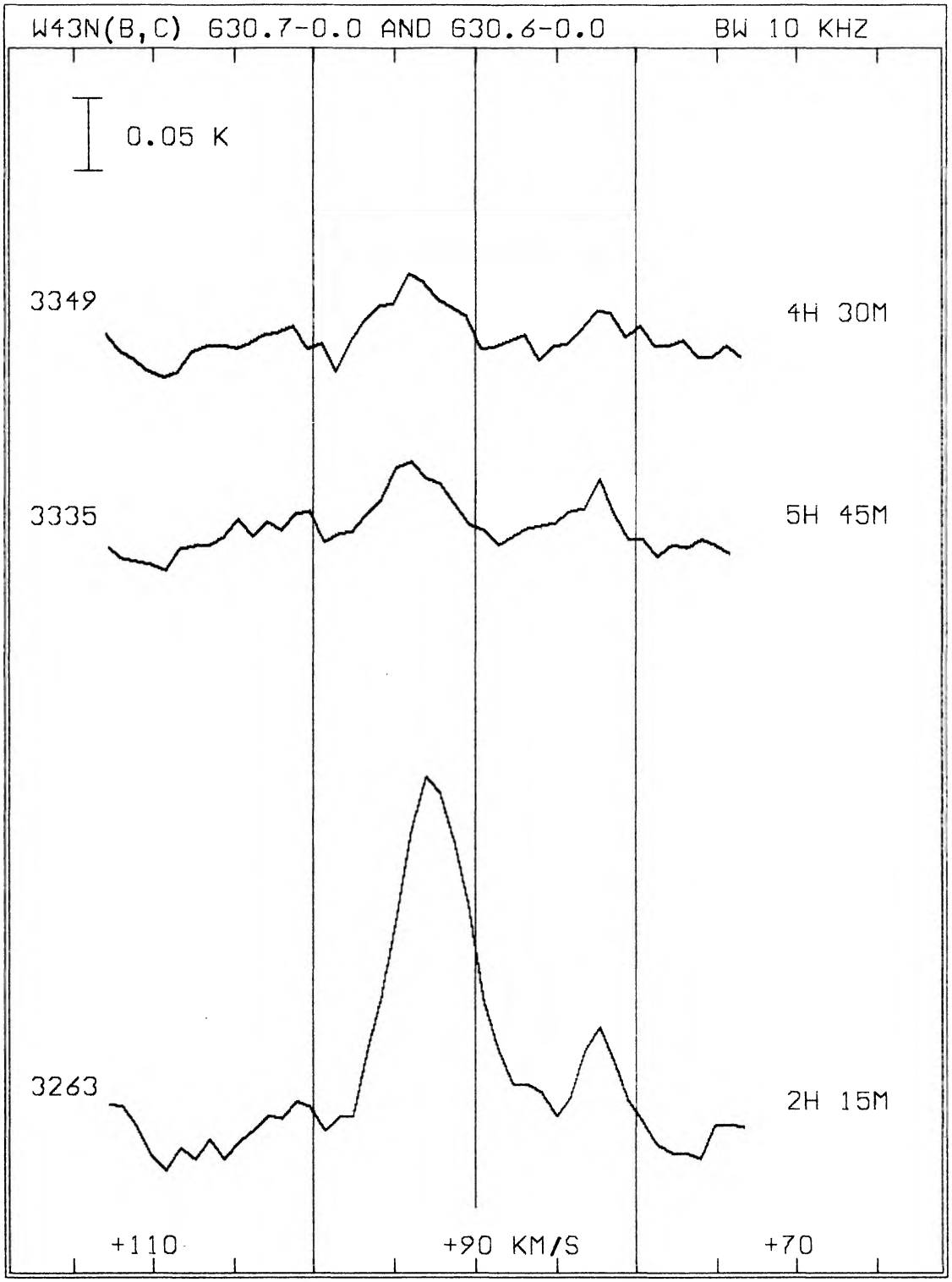

FIG. 13.—Averages of CH spectra of high velocity components toward G30.6−0.0 and G30.7−0.0. No difference was found between these two positions.

the +93 km s^{-1} feature. In the direction of G30.4−0.2 broad, weak emission in all three lines appears in the velocity interval +90 to +106 km s^{-1}. The peak emission moves from +93 km s^{-1} in the northern part of the region to +100 km s^{-1} toward G29.9−0.0. A similar velocity shift occurs for H_2CO (Zuckerman *et al.* 1970; Wilson 1972) and for OH (unpublished Onsala data). Wilson *et al.* (1974) have observed CO emission at our CH

positions. The agreement with the CH velocities is very good, if one considers the limited velocity resolution of the CO observations.

The double structure apparent in Fig. 13 is also seen in the absorption spectra of OH, H_2CO, and H I (already referred to; see also Table 2). We may conclude that these species exist in the same clouds and hence that the CH features emanate from gas in front of the continuum source complex. The same conclusion can be drawn for the $+100$ km s^{-1} CH features in the direction of G29.9−0.0. Toward G30.7−0.0 a single broad NH_3 feature has been observed (Morris *et al.* 1973*b*), centered at about the higher CH velocity component. Hydrogen recombination line velocities have been reported for G29.9−0.0, G30.7−0.0, and G31.1+0.0 at about +96, +92, and +99 km s^{-1}, respectively (Reifenstein *et al.* 1970).

The strong, and characteristic, enhancement of both lower satellite CH features toward G30.7−0.0 and G30.6−0.0 (cf. Fig. 13) most likely results from far-infrared pumping of two separate CH clouds. The multiple radio and infrared source structure should be remembered in this context.

v) *G34.3+0.1 (W44, H II region)*

This H II region, at a probable distance of about 4 kpc, lies close to the supernova remnant in W44 (G34.7−0.6). The W44 H II continuum source, observed at 2.7 GHz by Willis (1973), has recently been resolved into at least two components (Turner *et al.* 1974*a*). A far-infrared source has also been detected in this direction (Olthof 1974). The H109α recombination line velocity is +54 km s^{-1} (Reifenstein *et al.* 1970). OH absorption features appear in the velocity range +50 to +65 km s^{-1}, partly masked by sharp emissions (Onsala unpublished data; see also Yngvesson *et al.* 1973, 1975). Wilson (1972) reports H_2CO absorption at +60 km s^{-1}. CO emission features, observed at a slightly different position, occur at +55 km s^{-1} (strongest) and +64 km s^{-1} (Wilson *et al.* 1974). OH and H_2O maser sources have also been detected toward this H II region (Yngvesson *et al.* 1973, 1975).

Our CH spectra (shown in Fig. 14) exhibit the anomalously strong lower satellite emission typical for so many H II regions which have associated far-infrared radiation. The double structure of the main CH emission between +55 and +65 km s^{-1} also resembles the CO and H_2CO features. This emission presumably emanates from gas in front of the continuum source complex, as do the OH and H_2CO absorptions. Our +53 km s^{-1} CH emission component could be associated with the H I self-absorption features at about the same velocity, observed over an extended area surrounding our CH position and thought to originate from dense dust clouds (Knapp 1974).

vi) *G43.2−0.0 (W49 A)*

The radio source W49 consists of a thermal complex, A, containing several compact components, and a non-thermal region, B, separated by about 12′ (Schraml and Mezger 1969; Goss and Shaver 1970; Wynn-Williams 1971). On the basis of neutral hydrogen absorption spectra (Radhakrishnan *et al.* 1972*b*) the H II region W49A has been placed at the far kinematic distance of 14 kpc. The H109α recombination line velocity is +9 km s^{-1} (Reifenstein *et al.* 1970).

W49A is one of the most luminous H II regions in the Galaxy, both in the radio region and in the far-infrared, where it also exhibits complex structure (Harper and Low 1971; Hoffman, Frederick, and Emery 1971; Rieke *et al.* 1973; Becklin, Neugebauer, and Wynn-Williams 1973). At optical wavelengths the W49 area is completely obscured.

OH and H_2CO absorption features, as well as emission lines from OH, H_2O, CO, CS, HCN, and U93.2 have been observed in the direction of W49A (cf. Table 2). Our CH spectra (Fig. 15) have features centered at about +15, +41, and +62 km s^{-1}, in good agreement with reported H I (Radhakrishnan *et al.* 1972*b*) and H_2CO absorptions (Zuckerman *et al.* 1970; Wilson 1970, 1972; Scoville and Solomon 1973). The 1667 MHz OH spectra observed in the direction of W49A by Pastchenko and Slysh (1973) also show absorption at the two higher velocities, but strong maser emission in the low-velocity range. One may conclude that the +41 and +62 km s^{-1} features originate from clouds in spiral arms in the line of sight to the nebula (cf. also Fig. 2). A possible carbon recombination line feature at +64 km s^{-1}, believed to be associated with such clouds, has been reported by Pankonin, Parrish, and Terzian (1973). The +41 km s^{-1} CH spectra appear to exhibit approximate LTE line ratios, while the +62 km s^{-1} feature may be composed of two components, one of which displays a slightly enhanced lower satellite (for comparison see also the paragraph on Cas A).

The +15 km s^{-1} feature exhibits a strongly enhanced lower satellite line, extending from 0 to +20 km s^{-1}. This is, on an absolute scale, the strongest CH emission seen by us to date. Broad lines of CO, CS, and HCN are reported in this velocity range (Scoville and Solomon 1973; Turner *et al.* 1973; Snyder and Buhl 1971), as well as a carbon recombination line (Chaisson and Ball 1971). The complex structure of the CH lower satellite line is also similar to the CO emission, which has components at about +5, +12, and +16 km s^{-1} (Scoville and Solomon 1973). The striking resemblance between the lower satellite emission and the 6 cm H_2CO absorption (Zuckerman *et al.* 1970) suggests that the two species are well mixed in a cloud in front of the H II region. The component at about +5 km s^{-1}, in the lower satellite CH spectrum, is probably associated with the H II region and not due to local gas, since it is barely seen in the main and upper satellite line spectra. On account of the distance ambiguity (see Fig. 2), we cannot conclude whether the main line component at about +16 km s^{-1} originates from relatively nearby gas, or from the spiral arm in which the nebula is embedded. CH observations around W49A and B might solve some of the problems outlined here.

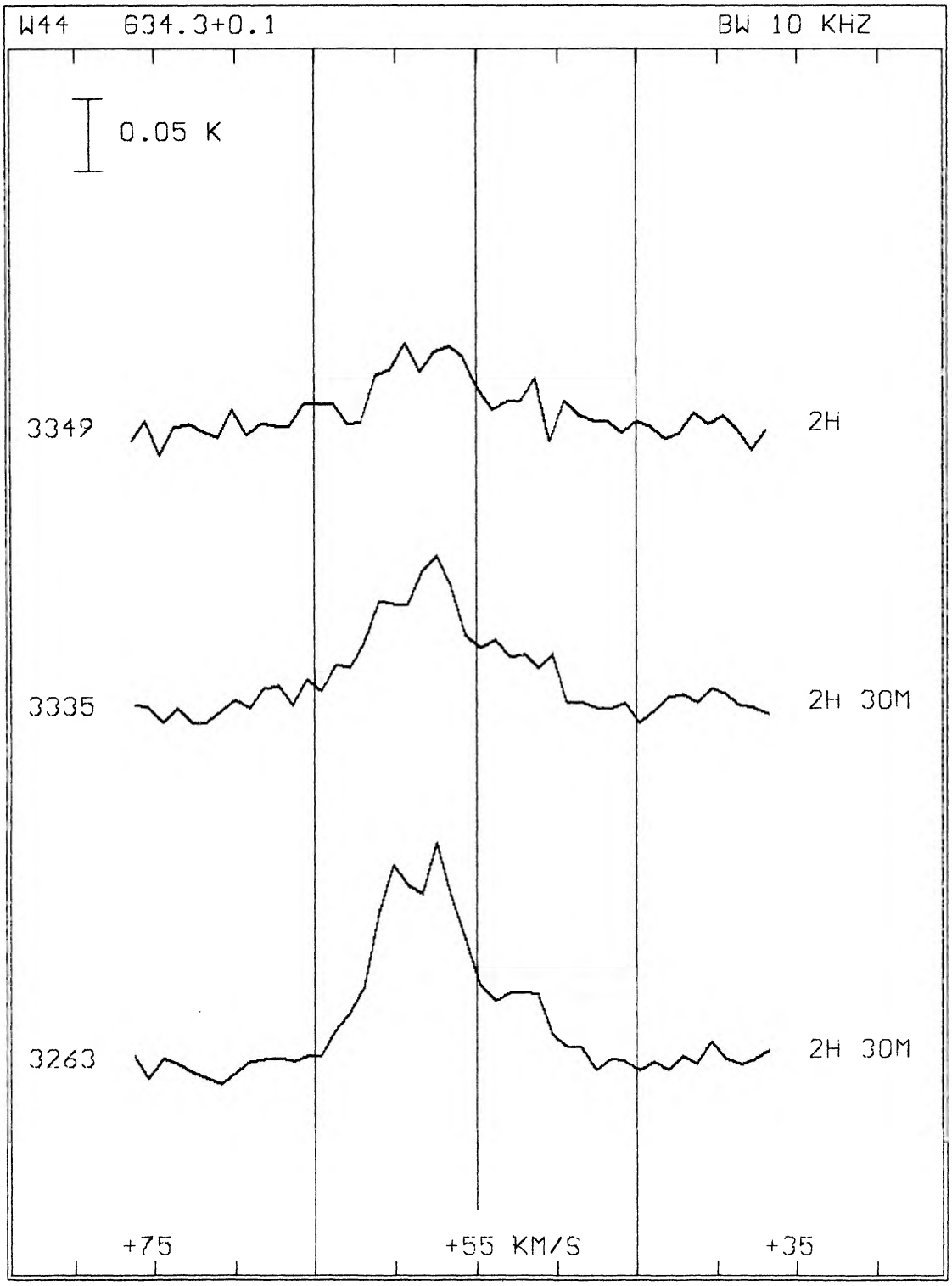

FIG. 14.—CH spectra toward W44, H II region

The enhancement of the +15 km s^{-1} feature in the lower satellite line is probably caused by far-infrared radiation from W49A (see § VII). The double structure of this feature may reflect the fact that this region contains several compact components, detected both at radio and infrared wavelengths.

It is interesting to notice that our W49 results indicate that it should be possible (with sufficient integration time) to map at least fractions of the CH Galactic spiral arm structure.

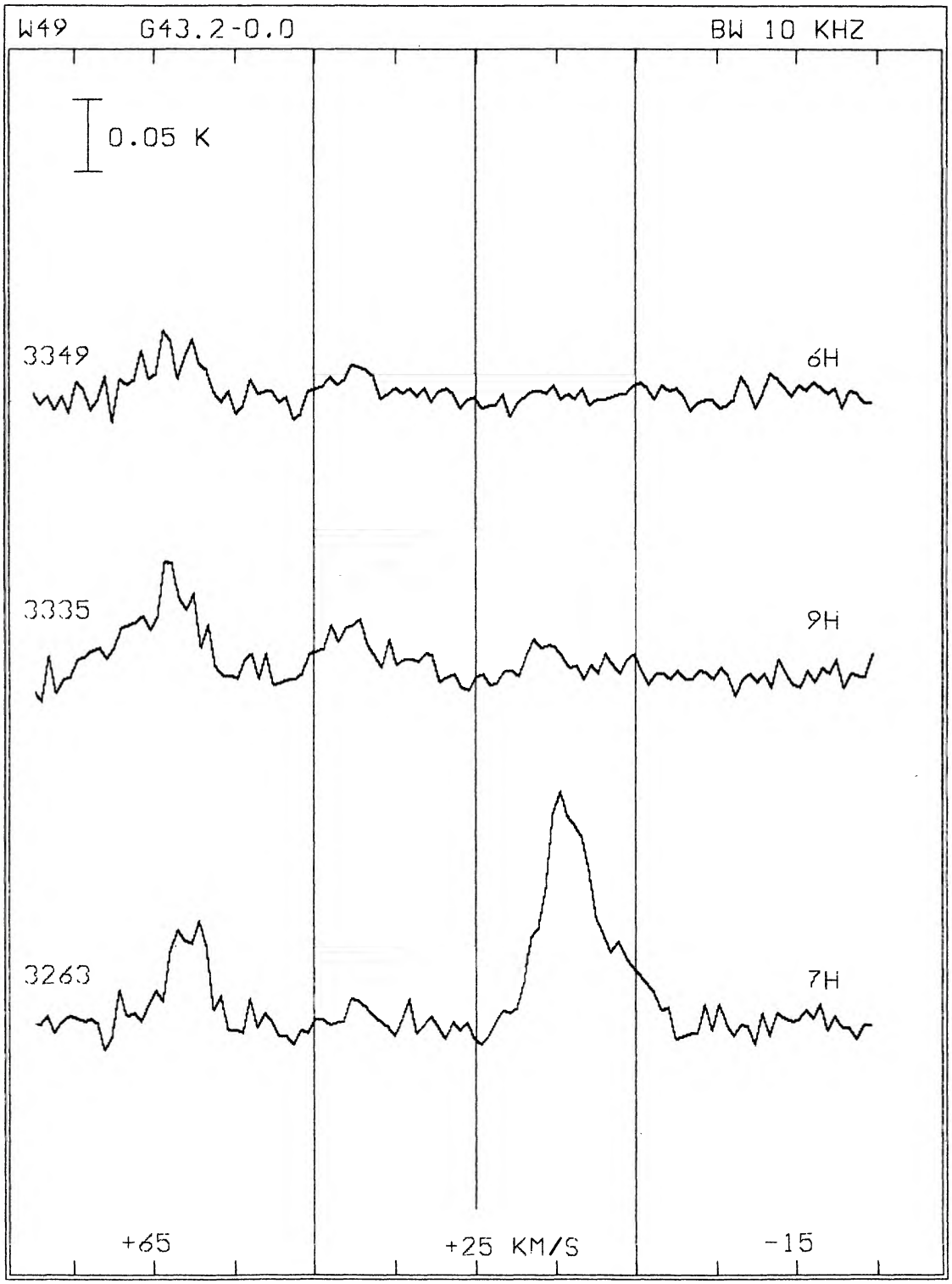

FIG. 15.—CH spectra toward W49A, which demonstrate spiral arm features at about +62 and +41 km s^{-1}. The +15 km s^{-1} feature is associated with the H II, far-infrared source.

vii) *G49.5−0.4 (W51 region)*

The W51 area is known to be composed of a number of discrete radio sources in the Sagittarius arm (MacLeod and Doherty 1968; Schraml and Mezger 1969; Goss and Shaver 1970) which form two main groups, a northern and a southern (cf. Fig. 16). The northern group consists of two main thermal components, G49.5−0.4 and G49.4−0.3, at a distance of about 8 kpc, while the southern group has four thermal components at a distance of about 6.5 kpc (Wilson *et al.* 1970*a*; Radhakrishnan *et al.* 1972*b*; Sato 1973). In addition to the thermal components there are indications of an extended, nonthermal region east of the southern complex, probably a supernova remnant (Shaver 1969; Wilson *et al.* 1970*a*) at a distance of about 5 kpc (Wilson 1973; Sato 1973).

G49.5−0.4 and G49.4−0.3 have been identified with far-infrared emission in the band 45–750 μ (Harper and Low 1971). The northern and southern complexes of W51 are each associated with a 100 μ source (Hoffman, Frederick, and Emery 1971). Emission at 350 μ is observed throughout the general region occupied by the eight compact H II condensations which form the component G49.5−0.4 (Martin 1972; Rieke *et al.* 1973). Two of these condensations have also been associated with infrared emission in the range 1.65 to 20 μ (Wynn-Williams, Becklin, and Neugebauer 1974*a*). The W51 region is heavily obscured optically.

The strongest radio component, G49.5−0.4, is known to be associated with emission or absorption by a number of molecular species (OH, H_2O, H_2CO, CO, SO, H_2S, NH_3, CN, CS, C_2H, HCN, HCCCN, U89.2, U90.7, U93.2, and possibly H_2CS and HNCO; cf. Table 2).

We have mapped the W51 region in 16 points for the three CH lines. CH emission has been found at about $+5$ km s^{-1} and between $+50$ and $+70$ km s^{-1}. The peak emission for these two velocity features is shown in Figures 16 and 17.

The $+5$ km s^{-1} features are seen in most points and seem to be essentially independent of the background continuum brightness. They have a full width at half-intensity of 2 to 3 km s^{-1}. Ground state OH features at the same velocity with approximately the same width have also been seen over an extended region, centered near the continuum source G49.1−0.4 (the 1720 MHz line in emission and the three other lines in absorption, with the 1612 MHz line anomalously strong; Goss 1968; Goss *et al.* 1973). Unpublished Onsala data show that this kind of OH emission and absorption at about the same velocity is also present, although weaker, toward the strongest continuum source G49.5−0.4. The CH emission is similarly stronger near G49.1−0.4 than toward G49.5−0.4. Possible features are also present in the OH satellite line spectra of Robinson, Goss, and Manchester (1970). Wilson (1973) has detected 1667 MHz absorption and 1720 MHz emission near $+7$ km s^{-1} in three directions toward the supernova remnant.

21 cm H I absorption spectra show features at about $+6$ km s^{-1} toward G49.5−0.4 and G49.1−0.4 (Radhakrishnan *et al.* 1972*b*). The presence of H I gas at $+6$ km s^{-1}, in front of the entire W51 continuum complex, has been demonstrated by Sato (1973) and Sato and Akabane (1974), who used the Maryland-Greenbank Galactic 21 cm Line Survey (Westerhout 1969).

To our knowledge no 6 cm H_2CO absorption features have been detected at this low velocity from the W51 area. However, such features have been seen toward the dark dust cloud L704 in the Aquila complex, situated about 1° southeast of this area (Minn and Greenberg 1973*a*; Dieter 1973).

All this taken together indicates that the CH, OH, and H I responsible for the low-velocity features coexist in an extended, inhomogeneous local cloud at a kinematic distance of about 0.5 kpc.

Although the signal-to-noise ratio is not high enough for a detailed discussion of the line ratios, it appears that the lower satellite CH line is enhanced to about the strength of the main line in most points (see Fig. 16). This is similar to the CH emission from the H I clouds observed toward Cas A. Due to the observed inhomogeneity of the low-velocity gas (CH and OH), it is not possible at this stage to decide whether CH is masing or not. However, we believe it to be a weak maser from the analogy with the Cas A clouds and from an assumption that conditions generally are similar in interstellar H I clouds.

In contrast to the low-velocity CH component, the intensity of the features in the velocity interval $+50$ to $+70$ km s^{-1} (depicted in Fig. 17) shows strong correlation with the continuum sources. The lower satellite is strongly enhanced in spectra observed close to the components G49.2−0.3 and G49.4−0.3 (for a detailed discussion of these, see Rydbeck *et al.* 1975), and particularly so in the direction of the strongest continuum source G49.5−0.4, which is also the strongest far-infrared source. The CH spectra observed in the latter direction are shown in Figure 18. In this velocity interval H I, OH, and H_2CO absorption features are seen more or less over the entire region (Sato 1973; Slysh 1975; Scoville and Solomon 1973; Sato and Akabane 1974). CO emission has been detected toward several of the H II regions (Scoville and Solomon 1973; Wilson *et al.* 1974; see also Table 2).

Our CH spectra toward G49.5−0.4 (see Fig. 18) exhibit emission in the interval $+50$ to $+72$ km s^{-1}. At least three components can be found (at about $+57$, $+66$, and $+69$ km s^{-1}) in the lower satellite spectrum. The shape of this spectrum agrees very well with the absorption spectrum of OH (Chaisson 1974).

The three velocity components can also be seen in the 6 cm H_2CO absorption (Onsala data, see Fig. 18; cf. also Zuckerman *et al.* 1970), although the maximum appears at $+67$ km s^{-1}, reflecting nonuniform conditions in this complex region.

The $+57$ km s^{-1} lower CH satellite component has no visible counterparts in the main and upper satellite lines.

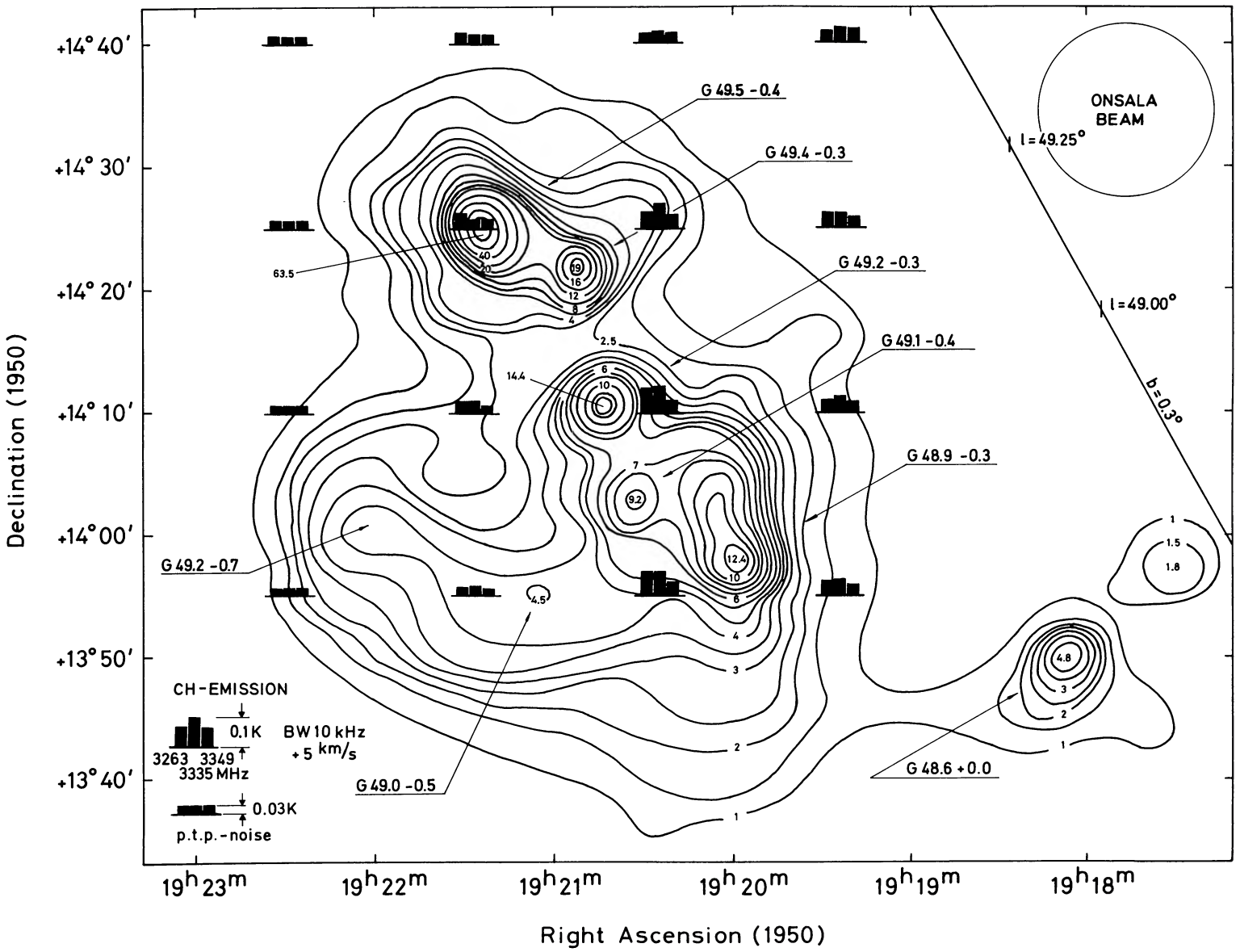

FIG. 16.—A 5 GHz continuum map (from Goss and Shaver 1970) of the W51 region, with bars representing the CH peak antenna temperatures at about +5 km s^{-1}. The contour unit is 1 K brightness temperature. The three CH lines are identified with the bars as shown at bottom left. The main continuum sources are indicated with arrows and galactic coordinates.

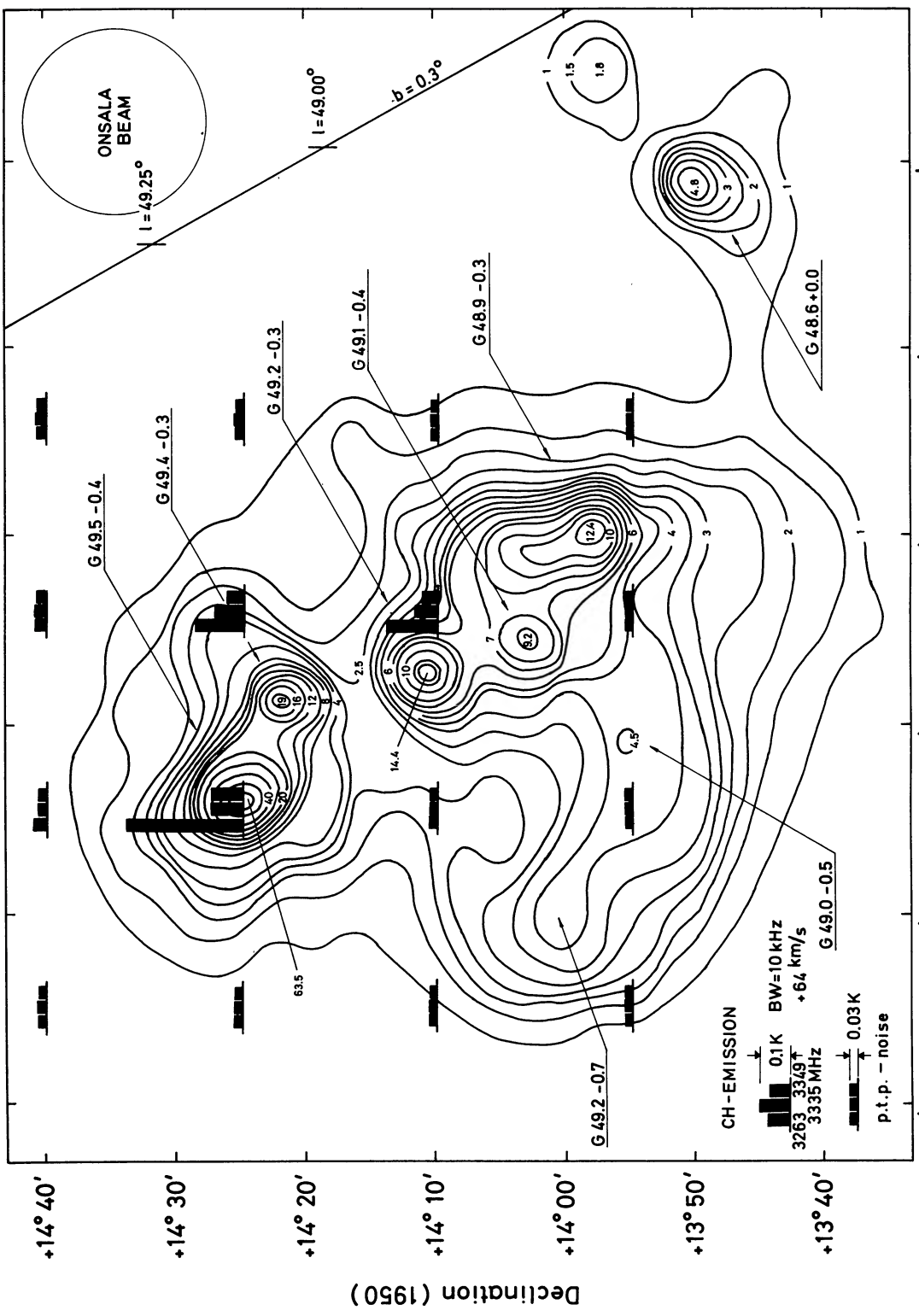

FIG. 17.—Same as Fig. 16 but for the +64 km s^{-1} component. The strong enhancement of the CH lower satellite transition toward the dominant H II–infrared components is clearly visible.

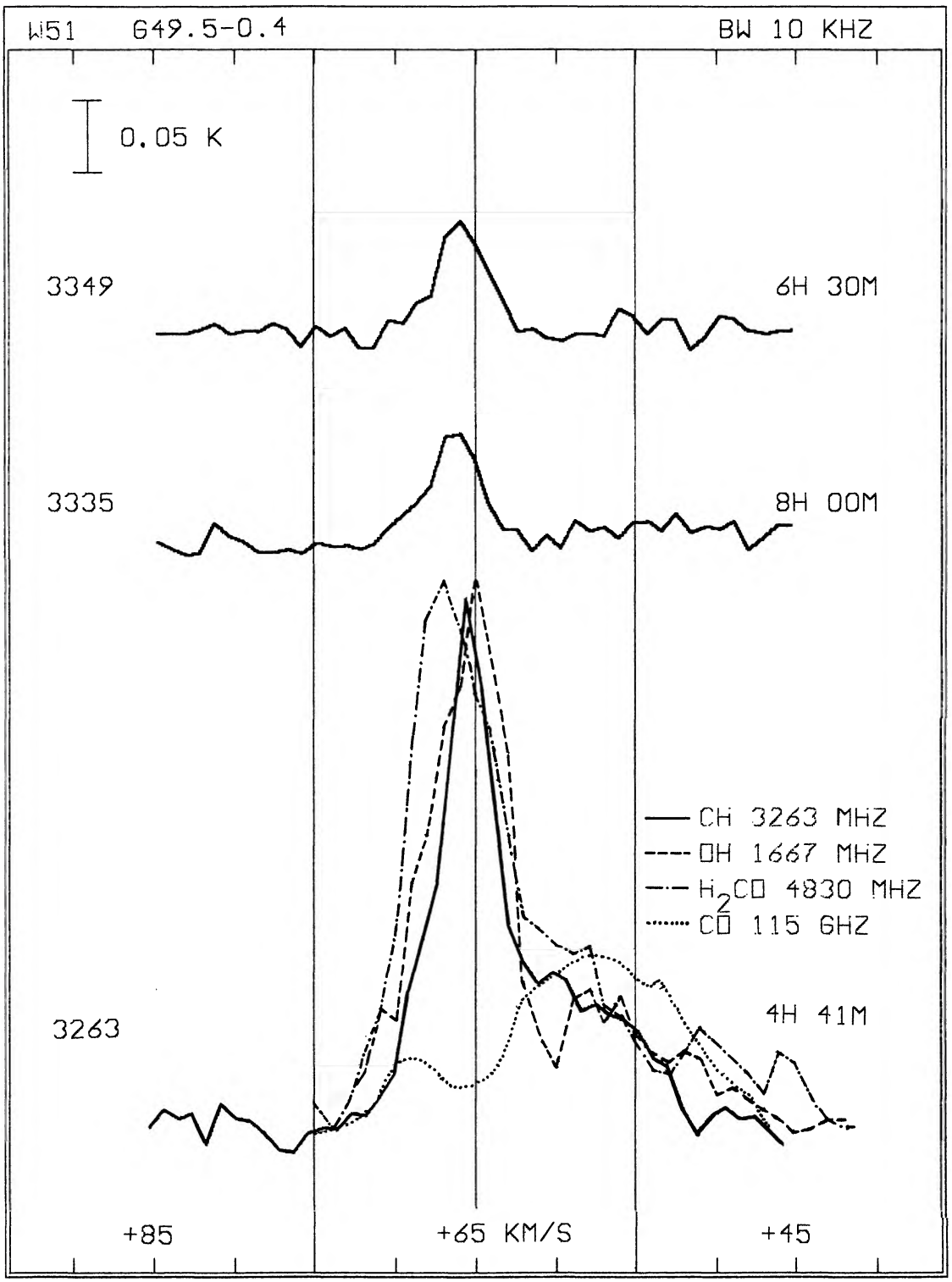

FIG. 18.—CH spectra of the high velocity components toward G49.5−0.4, with normalized profiles of the OH 1667 MHz main line absorption (Chaisson 1974), the H_2CO 4830 MHz line absorption (Onsala data), and the CO 115 GHz line emission (Scoville and Solomon 1973) superposed on the CH 3263 MHz lower satellite line. The OH and H_2CO profiles have been inverted to facilitate comparison with the emission spectra.

This component appears as the most intense feature in the millimeter emission spectra of CO, CS, and many other molecules (see Table 2 and Fig. 18), and is probably caused by gas in the compact molecular cloud associated with the G49.5−0.4 complex of H II regions (Scoville and Solomon 1973; Slysh 1975). A C92α recombination line has also been found close to this velocity (Chaisson 1974). This line is probably also associated with the molecular cloud. The H109α and H92α line velocities from G49.5−0.4 are slightly higher (Wilson *et al.* 1970*a*; Chaisson 1974). The strongest CH feature at $+66$ km s^{-1} has counterparts in OH and H_2CO absorptions (Zuckerman *et al.* 1970; Evans, Cheung, and Sloanaker 1970; Chaisson 1974). In CO, however, it corresponds to an emission minimum, which has been interpreted as caused by cold CO gas in a large cloud in front of the $+57$ km s^{-1} emission region (Scoville and Solomon 1973). OH, H_2CO, and H I observations indicate the presence of an extended cloud at about $+65$ km s^{-1} (Slysh 1975; Scoville and Solomon 1973; Sato 1973; Sato and Akabane 1974). H I interferometer observations toward G49.5−0.4 by Radhakrishnan *et al.* (1972*b*) also show a strong $+65$ km s^{-1} component, but no obvious one at $+57$ km s^{-1}. H_2CO interferometric measurements (Fomalont absorption at about $+58$ and Weliachew 1973) demonstrate that the km s^{-1} is weaker than that at $+65$ km s^{-1}.

The $+69$ km s^{-1} feature is clearly seen in all three CH transitions and also in the OH, CO, and CS lines (Slysh 1975; Scoville and Solomon 1973). Slysh (1975) finds reasons to associate the OH at this velocity with one of the compact H II components of G49.5−0.4 found by Martin (1972).

In the southeastern, nonthermal region of W51, around G49.2−0.7 and G49.0−0.5, OH absorption was observed in the velocity range $+45$ to $+60$ km s^{-1} by Wilson (1973). This absorption is much weaker than the previously discussed local, $+7$ km s^{-1} component. This might explain why there are no corresponding features in our CH spectra.

The presence of at least two strongly enhanced CH lower satellite features associated with the H II-infrared complex G49.5−0.4 probably reflects the multiple radio and infrared source structure.

viii) *G69.5−1.0 (ON 1)*

ON 1 was originally detected as a Class I OH emission source (Elldér, Rönnäng, and Winnberg 1969; Winnberg 1970). A compact H II region has been found coinciding with the OH source (Hardebeck 1972; Winnberg, Habing, and Goss 1973; Harris 1974) as well as with an H_2O maser source (Sullivan 1973; Yngvesson *et al.* 1973, 1975; Cato *et al.* 1975). The $+14$ km s^{-1} average velocity of the OH lines yields a kinematic distance of about 1 or 5 kpc. The region is heavily obscured optically.

Our CH spectra show emission at about $+11$ km s^{-1}, approximately at the LTE ratio. This is expected since the small continuum source is very weak (cf. relation 3). Morris *et al.* (1974*a*) have detected CS at $+11$ km s^{-1} with a linewidth (4 km s^{-1}) close to our value. Schwartz, Wilson, and Epstein (1973) report CO emission at $+14$ km s^{-1} in a direction (G69.4−1.5) about 30′ from our position. CO emission toward ON 1 has also been detected by Dickel *et al.* (1974). The unidentified line, U93.2, has recently been detected toward this source, at the velocity of CH and CS (Turner 1974); cf. Table 2.

ix) *G70.3+1.6 (ON 3, K3–50, NGC 6857, W58)*

ON 3 is an OH emission region (Elldér, Rönnäng, and Winnberg 1969; Rubin and Turner 1969; Winnberg 1970; Downes 1970) associated with the compact components of the W58 complex of H II regions (Wynn-Williams 1969; Higgs 1970; Rubin and Turner 1971; Hardebeck 1971; Wynn-Williams, Becklin, and Neugebauer 1974*b*; Harris 1975). An H_2O maser has recently been detected close to the very compact H II region K3–50 (Yngvesson *et al.* 1973, 1975), while Johnston, Sloanaker, and Bologna (1973) found no H_2O emission from the 1720 MHz OH line position, about 2′ away from K3–50. The hydrogen recombination line velocity of this region is about -24 km s^{-1} (Rubin and Turner 1969; Reifenstein *et al.* 1970; Rubin and Turner 1971). This velocity yields a kinematic distance of about 9 kpc. W58 (K3–50) is a very luminous far-infrared source (Neugebauer and Garmire 1970; Harper and Low 1971; Hoffman, Frederick, and Emery 1971). Persson and Frogel (1974), who observed that the interstellar extinction toward K3–50 is very high, have discussed the W58 area in some detail.

We find lower satellite CH emission in the velocity interval -19 to -25 km s^{-1}, but no visible main and upper satellite lines (cf. Table 1), a situation which sometimes arises toward strong far-infrared sources. Zuckerman *et al.* (1970) found a 6 cm H_2CO absorption profile toward K3–50 which has a shape and velocity similar to our lower satellite CH feature. Buhl and Snyder (1973) report U89.2 and HCN emission at these velocities, for which CO emission has also been observed in three positions (Wilson *et al.* 1974). H I absorption at 21 cm (Thompson *et al.* 1969; Bridle and Kesteven 1970), as well as carbon C94α recombination lines probably originating in the molecular cloud (Chaisson and Goad 1972), have been observed at the CH velocities toward K3–50.

To our knowledge no OH absorption features have been observed toward K3–50. The main line OH emission and the H_2O maser lines appear in the interval -19 to -27 km s^{-1}, while the 1720 MHz OH emission is centered around -13 km s^{-1}. It has been suggested that the main line OH and H_2O masers are separated from the 1720 MHz OH source (Yngvesson *et al.* 1973, 1975). The former are probably associated with K3–50. Since the CH upper satellite and main lines are virtually absent, the lower satellite CH emission is most likely connected with the K3–50 far-infrared source. This demonstrates that the anomalous emission of the lower CH satellite transition is probably an important far-infrared radiation indicator.

x) *G75.8+0.3 (ON 2)*

ON 2 is a class I OH maser source (Elldér, Rönnäng, and Winnberg 1969; Winnberg 1970). Its position (Hardebeck and Wilson 1971) approximately coincides with an H_2O maser complex (Johnston, Sloanaker, and Bologna 1973; Yngvesson *et al.* 1973, 1975; Cato *et al.* 1975). Matthews *et al.* (1973) found at least three compact H II regions within a radius of about 3′ in this direction. Reifenstein *et al.* (1970) report a H109α recombination line at -5 km s^{-1}, which yields a kinematic distance of about 5.5 kpc.

Our CH spectra show emission in approximately the LTE ratio in the velocity interval -5 to $+7$ km s^{-1}, i.e., in the range of the OH and H_2O emission velocities (cf. Table 2). To our knowledge no other molecules have been detected toward ON 2 so far.

xi) *G80.6+0.0 (Cygnus X region, 78° < l < 85°; −2° < b < 2°)*

This complex area of the sky is viewed in the direction tangential to the Orion arm (cf. Fig. 2). It contains numerous discrete radio components, the strongest of which are the well known DR sources, and has been extensively studied (e.g., Pike and Drake 1964; Downes and Rinehart 1966; Dickel, Wendker, and Bieritz 1969, 1970; Wendker 1970; Kap-herr and Wendker 1972; Terzian and Parrish 1973). A neutral hydrogen survey of the Cygnus X region has been performed by McCutcheon and Shuter (1970). Most of the area that we observed (cf. Fig. 19, adopted from Wendker 1970) is heavily obscured by the large foreground dark clouds which form the Great Cygnus Rift (Miller 1937; Lynds 1962, 1968; Neckel 1966; Ackermann 1970). Several far-infrared sources have been detected close to the stronger H II regions (Harper and Low 1971; Hoffman, Frederick, and Emery 1971; Rieke *et al.* 1973; Emerson, Jennings, and Moorwood 1973; Jennings 1973).

We find CH emission over almost the entire region (Fig. 20). Although the signal-to-noise ratio does not allow a detailed discussion of many of the spectra, the velocity field is informative. A positive velocity component at around $+5$ km s^{-1} is present in most spectra, indicating an extended foreground cloud (Fig. 19), in agreement with OH absorption observations toward the DR sources by Pashchenko (1974). He also finds a dense cloud moving with velocities of -2 to -6 km s^{-1}, at a kinematic distance of about 3 kpc, in front of DR 20–23. The corresponding velocity features can be traced in our CH spectra (Fig. 20). However, DR 17, which is close to our point H11 in Figures 19 and 20, shows neither CH nor OH features at these velocities and is probably closer to us. That conclusion is supported by its H109α recombination line velocity of $+11$ km s^{-1}, which yields a distance of 1.5 kpc (Reifenstein *et al.* 1970). Furthermore, a CO feature, at about $+9$ km s^{-1}, has been found by Wilson *et al.* (1974). The H I absorption results by Sato (1968) are in agreement with these findings.

Our observations (Fig. 20) also confirm the existence of a third, more distant (4–5 kpc) cloud, also discovered in OH by Pashchenko (1974), in front of the sources DR4–7, 9, 13, and 15, bounded by the coordinates $78° < l < 79°$, $-0.°5 < b < 2°$. Separate CH spectra for all three lines toward DR5 and DR15 are presented in Rydbeck *et al.* (1975). The spectra toward DR15 show a main component near zero velocity, and also a weak component at about $+9$ km s^{-1} (cf. Table 1). The latter component can also be traced in the spectra of adjacent points in the southwest corner of Figure 20, and is attributed to the extended foreground cloud. The DR5 spectra, however, display only the zero velocity component. Millimeter wave emission from CO, CS, and HCN shows a component at about -5 km s^{-1} towards the AFCRL (UOA)-19 infrared source (Dickel *et al.* 1974; Morris *et al.* 1974*a*), situated approximately halfway between DR 5 and DR 15. The CO emission displays a multiple structure as do our CH spectra in adjacent points. Turner (1972*b*) observed OH absorption toward and around Cyg X-3 (cf. Fig. 19) at $+2$ to $+5$ km s^{-1}. He also found OH and H_2CO at about $+12$ km s^{-1}, but only toward Cyg X-3 itself, probably from a very small cloud. Lauqué, Lequeux, and Nguyen-Quang-Rieu (1973) found H I absorption at small positive velocities in the Cyg X-3 direction, apparently from the earlier mentioned extended foreground cloud.

We have also searched for 6 cm H_2CO absorptions at five of our CH positions, *viz.*, D4, D8, F6, H4, and H8 in Figures 19 and 20. At D4 and D8 we found absorption features at about $+6$ km s^{-1}, and in D8 also at about -4 km s^{-1}, in good agreement with the CH spectra. Negative H_2CO results were obtained at the other three points, in agreement with Turner's (1972*b*) negative results toward DR 18. Wilson (1972) detected an H_2CO positive velocity component toward DR 23, about 20′ northeast of our point D8. He likewise found only one component at $+7$ km s^{-1} toward DR 22. CO emission features at -6 and $+6$ km s^{-1} have been observed toward DR 23 (Wilson *et al.* 1974); our CH spectra in adjacent points C9 and D8 (Fig. 20) exhibit a similar pattern.

Separate CH spectra toward DR 22 (Rydbeck *et al.* 1975) show, besides the strong $+6$ km s^{-1} component emanating from the foreground extended cloud, a weak component at about -3 km s^{-1} with an enhanced lower satellite line. Both features can also be traced in most adjacent points. DR 22 is also a relatively strong far-infrared source (Hoffman, Frederick, and Emery 1971; Jennings 1973). Wilson *et al.* (1974) observe weak CO emission at -1 and -11 km s^{-1}.

Two dark dust clouds, surveyed in the 6 cm H_2CO line, fall within the map depicted in Figure 19. Dieter (1973) found absorption in the range -3 to 0 km s^{-1} toward five points (indicated in the figure) centered on the small cloud L896. Minn and Greenberg (1973*a*) found components at -4, -2, and $+2$ km s^{-1} in their cloud 36 (G82.89+0.23), which is a dark patch in the western side of the North America Nebula (NGC 7000).

Typical column densities, based on a CH main line excitation temperature T_x of -15 K, are as follows. Toward DR 21 and DR 22, for the foreground cloud, about 10^{14} and 2×10^{14} cm^{-2}. If we assume that $T_x = 5$ K for the

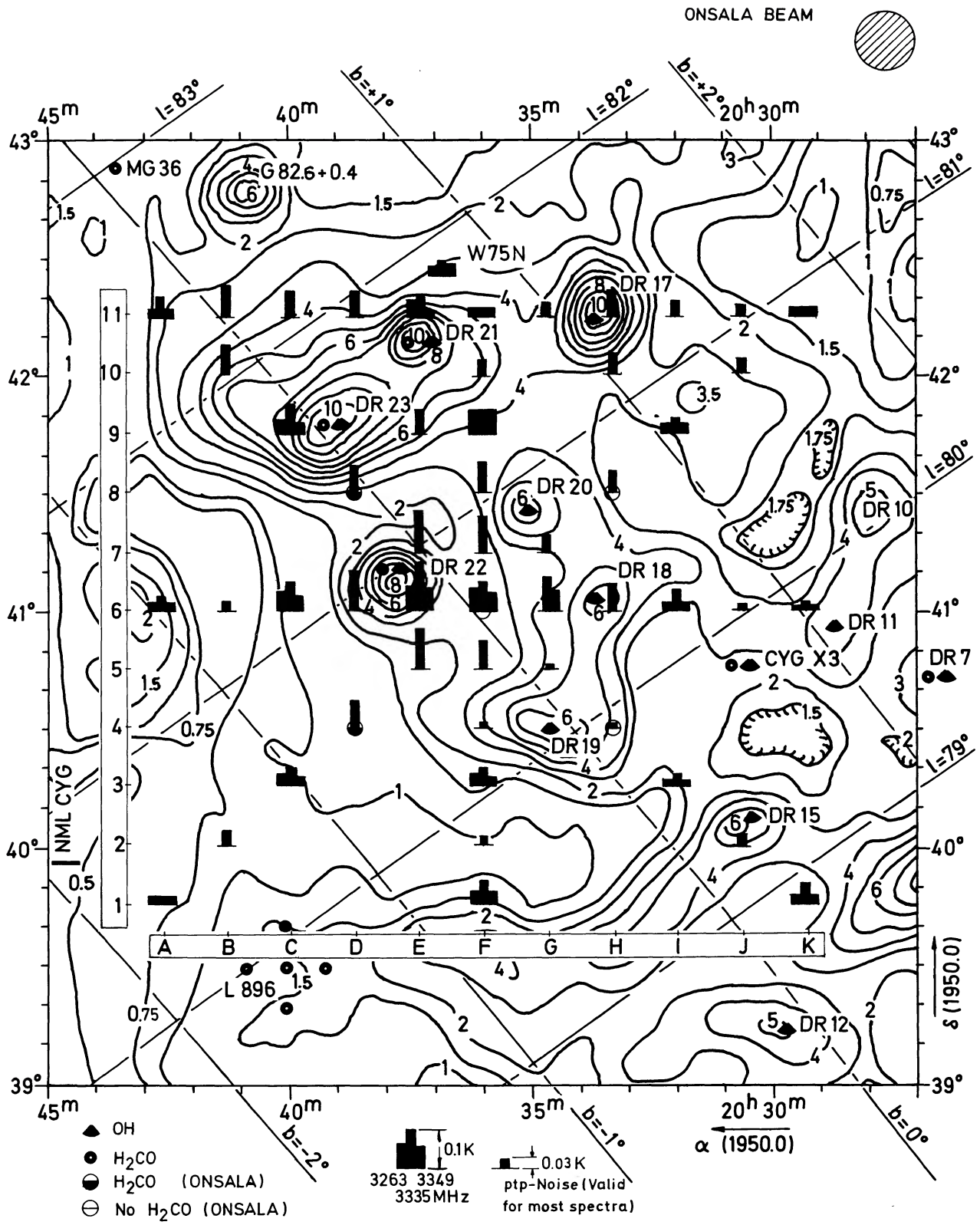

FIG. 19.—A 2.7 GHz continuum map (from Wendker 1970; kindly supplied in a large format by H. J. Wendker) of the Cyg X region, with bars representing the CH peak antenna temperatures at about $+5$ km s^{-1}. The contour unit is 1 K brightness temperature. Points with only a single bar were observed only in the main CH line.

The main continuum radio sources have been entered on the map, together with the OH/IR star NML Cyg, the OH/H_2O source W75N, the X-ray source Cyg X3, Lynds's cloud L896, and cloud No. 36 in Minn and Greenberg's (1973*a*) 6 cm H_2CO survey. Special symbols have been used to indicate positions searched for OH and H_2CO. The vertical and horizontal labels (1–11; A–K) have been introduced for quick text reference to the various CH positions.

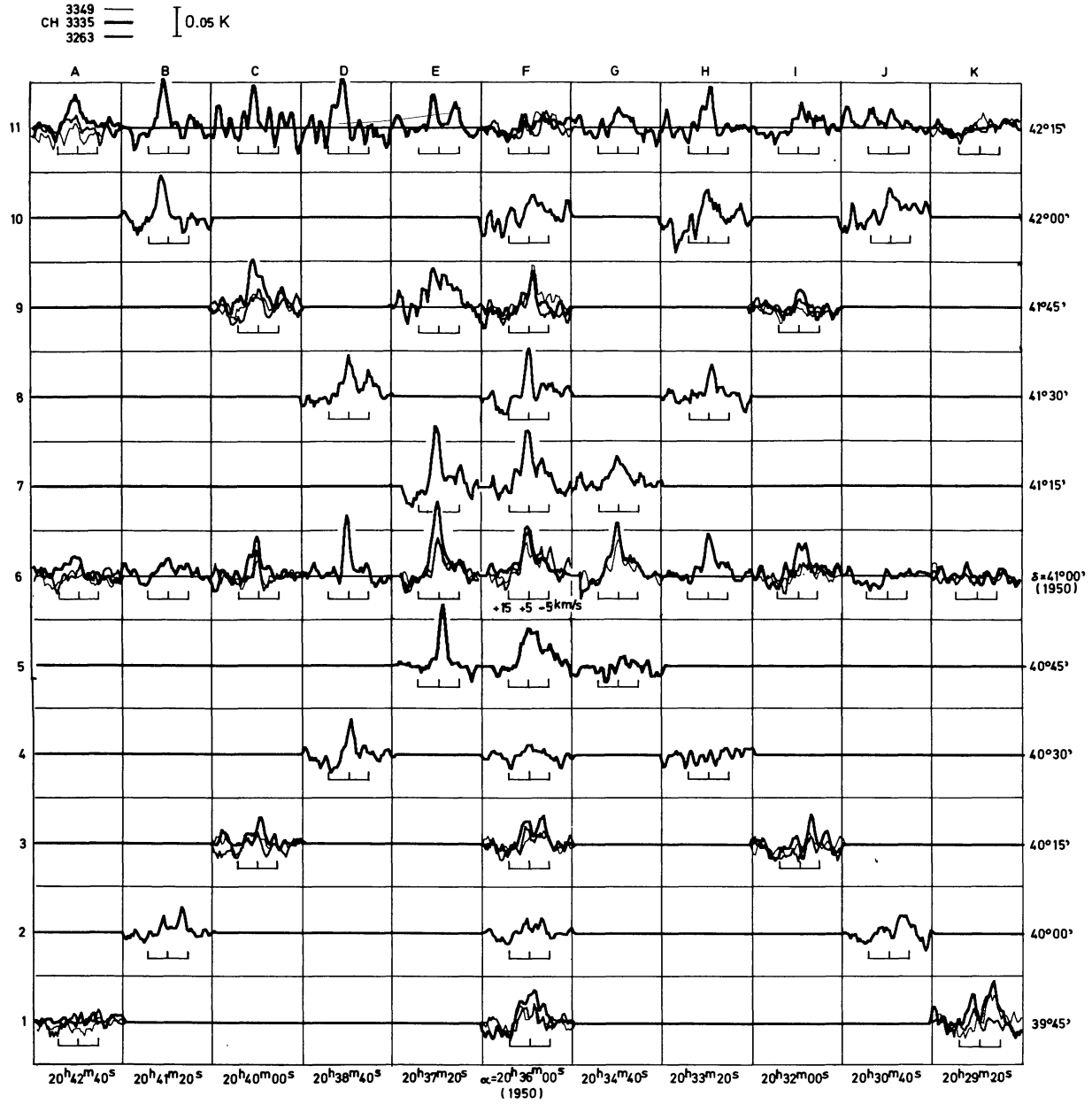

FIG. 20.—CH spectra obtained toward the CH positions of Fig. 19. The frequency resolution is 30 kHz.

OH main line, the corresponding OH column densities are approximately 3×10^{14} for the two objects. Finally, as a further example, we obtain about 10^{13} and 2×10^{13} cm^{-2} for the 6 cm H_2CO transition, if its T_x is assumed to be 2 K. These values should be compared with the similar results obtained in the direction of Cas A. Details of column densities for other objects in the Cyg X region are found in Table 1. Figures 19 and 20 demonstrate the existence of considerable column density variations in the Cyg X foreground clouds.

NML Cyg, located in the southeastern part of Figure 19, was not detected in any of the three CH lines, despite the considerable integration times used. This, and other negative results, will be discussed in § V.

xii) *G81.7+0.5 (DR 21, W75 area)*

DR 21, probably associated with the Horseshoe Nebula, is part of the diffuse H II region W75. It is a very compact and intense H II region, composed of several components (Downes and Rinehart 1966; Webster and Altenhoff 1970; Wynn-Williams 1971; Balick 1972; Harris 1973, 1974). Two OH emission sources, W75S and W75N, have been detected north of DR 21 (Rydbeck, Elldér, and Kollberg 1969; Zuckerman *et al.* 1969). Two weak continuum

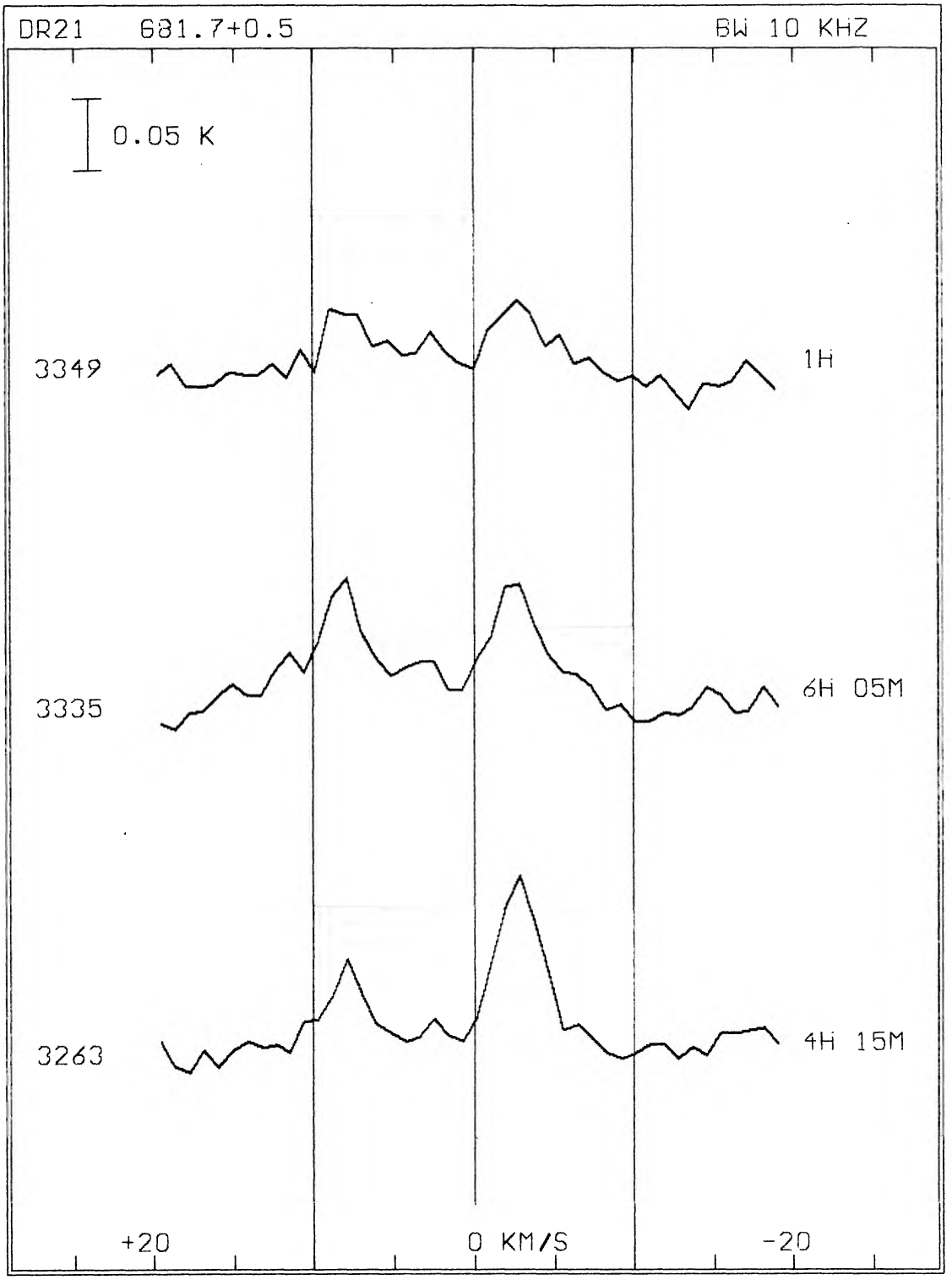

FIG. 21.—CH spectra toward DR 21

sources have been found in the W75N region; one coincides with the OH source (Wynn-Williams 1971; Habing *et al.* 1974). H_2O maser emission has been observed from several points both in W75S and W75N (Knowles *et al.* 1969; Yngvesson *et al.* 1973, 1975; Johnston, Sloanaker, and Bologna 1973; Cato *et al.* 1975).

The observed recombination lines toward DR 21 lie around zero velocity (Reifenstein *et al.* 1970; Terzian and Balick 1972; Terzian and Parrish 1973). OH and H_2CO absorption data, together with the recombination line velocities, yield a distance of about 3 kpc (Rydbeck, Elldér, and Kollberg 1969; Pashchenko 1974). DR 21 is also

a far-infrared source (Harper and Low 1971; Hoffman, Frederick, and Emery 1971; Jennings 1973). Rieke *et al.* (1973) have resolved the source at 350 μ into two components of about equal strength, identified with DR 21 and W75S. Near-infrared emission sources have been found in the directions of DR 21, W75S, and also W75N (Wynn-Williams *et al.* 1974*a*).

Our CH spectra toward DR 21, shown in Figure 21, display two well-defined features at about -3 and $+8$ km s^{-1}, in excellent agreement with velocities and widths from OH and H_2CO absorption data (Rydbeck, Elldér, and Kollberg 1969; Zuckerman *et al.* 1970; Wilson 1972; Pashchenko 1974). The $+8$ km s^{-1} component is caused by the Cyg X foreground cloud. The -3 km s^{-1} component, with the enhanced lower satellite line, probably is associated with the molecular cloud whose existence has been established by measurements of millimeter wave emission from SO, H_2S, NH_3, CS, C_2H, HCN, H_2CO, CH_3OH, U90.7, and 93.2 (see Table 2).

We also detected CH toward the W75N position, about 18′ north of DR 21. The intensities of both velocity components decreased to about half of the values found toward DR 21. Morris *et al.* (1974*a*) found HCN emission over a large part of the W75 region, probably extending from DR 21 to W75N. A -3 km s^{-1} component dominates in the vicinity of DR 21. In the W75N region, on the other hand, the strongest HCN features are found between radial velocities of $+5$ and $+12$ km s^{-1}. Wilson *et al.* (1974) and Dickel *et al.* (1974) observed a similar behavior for CO.

xiii) *G84.7−1.0 and G84.9−1.0 (NGC 7000, IC 5070, W80, DR 27, North America and Pelican Nebulae)*

These extended nebulae, located at a distance of about 1 kpc (Hippelein 1973), appear as a complex mixture of emission nebulosities and dark dust clouds. Recombination line velocities between -4 and $+1$ km s^{-1} have been found across this region (Pedlar and Matthews 1973). An extended far-infrared emitter (size $\approx 0.^\circ 6$) has also been detected in this direction (Hoffman, Frederick, and Emery 1971).

We have detected CH in two positions in NGC 7000, *viz.*, toward the "Gulf of Mexico" dust cloud G84.7−1.0 and toward G84.9−1.0 (see Table 1). The former spectra show emission of all three transitions, in the velocity range -3 to $+7$ km s^{-1}. Cudaback and Heiles (1969) detected OH 1667 MHz absorption in this direction at $+3$ km s^{-1}. Turner (1973) observed all four 18 cm OH lines toward this dust cloud and found satellite line anomalies, of Type II(a) and II(b), at about 0 and $+4$ km s^{-1}. He believes that these anomalies are caused by infrared pumping. CO has been detected in the range -2 to $+6$ km s^{-1}, probably with a multiple structure (Penzias, Wilson, and Jefferts 1972). This emission, which is centered at about $+2$ km s^{-1}, extends over an area greater than $2^\circ \times 2^\circ$. An NH_3 feature, probably narrow, was found at about $+1$ km s^{-1} (Cheung *et al.* 1973). Since the CH emission has its maximum at about $+2$ km s^{-1}, it may be associated with this molecular cloud.

Our spectra toward G84.9−1.0 (separated by about 12′ from the previous position), are very similar to the first ones. In this direction Minn and Greenberg (1973*a*) found 6 cm H_2CO absorption, at about $+1$ and $+5$ km s^{-1}. The slight enhancement of the CH satellite lines may be caused by the extended infrared source.

xiv) *G111.5+0.8 (NGC 7538, S158)*

This H II region, approximately 8′ across, is located in the Perseus arm at a distance of about 4 kpc. It contains several compact radio components, as well as OH and H_2O emission sources (Schraml and Mezger 1969; Habing, Israel, and de Jong 1972; Israel, Habing, and de Jong 1973; Martin 1973; Terzian, Dennison, and Balick 1973; Johnston, Sloanaker, and Bologna 1973; Wynn-Williams, Becklin, and Neugebauer 1974*b*; Yngvesson *et al.* 1973, 1975; Cato *et al.* 1975). H109α emission appears around -61 km s^{-1} (Reifenstein *et al.* 1970). Infrared emission in the wavelength range 1.65 to 20 μ has been found from the compact H II condensations (Wynn-Williams, Becklin, and Neugebauer 1974*a*), indicating the presence of heated dust.

Our CH observations were performed toward the northern OH maser source (Wynn-Williams, Becklin, and Neugebauer 1974*b*) with the entire NGC 7538 nebula covered by the beam. We find weak emission in the velocity interval -62 to -48 km s^{-1}. The spectra seem to be composed of several components, of which a -52 km s^{-1} component is the strongest one in the main line. Another weaker component, at -57 km s^{-1}, might have enhanced lower satellite emission. Centered around this velocity, millimeter wave emission from H_2S, CO, CS, C_2H, HCN, U89.2, and U90.7 has been found (cf. Table 2). The narrow CS and HCN features are strongest at the OH/IRS 1 position, and have small angular extensions (Turner *et al.* 1973; Wynn-Williams, Becklin, and Neugebauer 1974*a*). At this position 6 cm H_2CO emission features, at -60 and -58 km s^{-1}, were recently detected with the Effelsberg 100 m telescope (Downes and Wilson 1974*a*). They also found absorption at -56 and -50 km s^{-1}.

CO emission has been observed over an extended ($\sim 0.^\circ 5$) area, also with maximum intensity toward IRS 1 (Wilson *et al.* 1974). Six-centimeter H_2CO absorption from three giant dust clouds in the general direction of NGC 7538 has been found by Minn and Greenberg (1975), at the velocities -56, -53, and -49 km s^{-1} for complexes denoted 1, 2, and 3. The space-velocity pattern is similar to that of CO. Minn and Greenberg believe that these complexes are located behind the bright nebula.

Our CH data agree with the general picture quite well. On account of our beam size Minn and Greenberg complexes 1 and 2, as well as the molecular cloud, all contribute to the CH velocity pattern. We have also observed the CH main and upper satellite transitions toward the center (G111.8+0.6) of complex 2. A narrower feature, still quite weak, was found to be centered around -52 km s^{-1}, in good agreement with the H_2CO data. The upper satellite line intensity had approximate LTE strength.

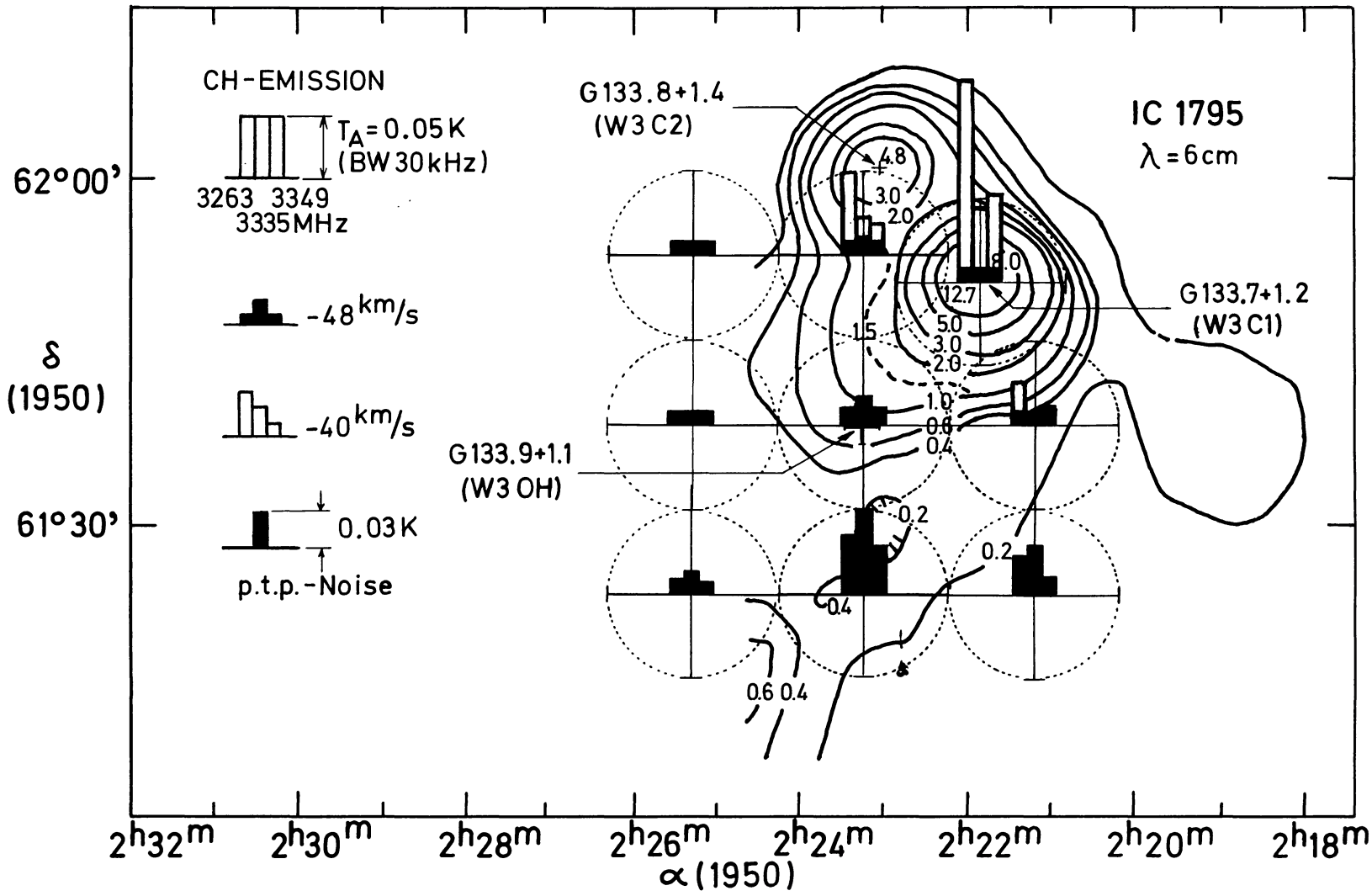

FIG. 22.—A 5 GHz continuum map (from Mezger *et al.* 1967) of the W3 region, with bars representing the CH peak antenna temperatures. The contour unit is 1 K antenna temperature. Open bars correspond to the -40 km s^{-1} features, solid bars to -48 km s^{-1}. The three CH lines are identified with the bars as shown at left. The half-power Onsala beam size is indicated by dotted circles.

xv) *G118.1+5.0 (W1, NGC 7822)*

This region contains emission nebulosities, irregularly distributed obscuring matter including several Lynds's clouds, and the Cep IV OB association. In the optical spectra of three bright stars, Münch (1964) observed CH and CN absorption lines with CH velocities between -12 and -8 km s^{-1}. Main line OH absorptions at about -14 and -7 km s^{-1}, approximately in LTE ratio, have been found by Winnberg and Lundahl (1970) in the position of the radio continuum source W1. Recombination line velocities of about -19 and -8 km s^{-1} have been found (Dickel and Milne 1972; Downes and Wilson 1974*b*). More recently CO has been observed at about -12 km s^{-1} (Wilson *et al.* 1974), while H_2CO has been sought for and not found. The distances of both the OB association and the H II region are probably somewhat less than 1 kpc (Winnberg and Lundahl 1970).

Our CH emission spectra show two components, which agree well in velocity and line shape with the OH absorption profiles. We have also detected the two CH features toward all positions in a 3 × 3 point grid, with 15′ spacing, centered on the W1 continuum maximum. We probably observe CH in two extended dust clouds.

xvi) *G133.7+1.2 (W3C1), G133.8+1.4 (W3C2), and G133.9+1.1 (W3OH)*

The W3 region is a strong radio source complex associated with the optical H II region IC 1795. Several Lynds's clouds are found in the direction of this area. Its properties have recently been summarized by Minn and Greenberg (1973*b*). The distance is estimated to be about 3 kpc.

The continuum radio emission is attributed to three separate regions, W3C1, W3C2, and W3OH, depicted on the 5 GHz continuum map, Figure 22. W3C1 has been shown to consist of several compact radio continuum components (Wynn-Williams 1971; Sullivan and Downes 1973). It is the strongest continuum source in the entire W3 region. W3C1 and W3C2 are located (about 12′ apart) northwest and north of the area of optical emission, in a region where such emission is heavily obscured by dust. Far-infrared radiation between 30 and 500 μ has been detected from the directions of W3C1 and W3OH (Emerson, Jennings, and Moorwood 1973; Harper 1974). High-resolution mapping in the 1.65 to 20 μ range has led to the discovery of several distinct infrared objects in the W3 region (Wynn-Williams, Becklin, and Neugebauer 1972).

W3C1 is associated with strong H_2O and weak OH radiation as well as with millimeter-wave emission from CO, H_2S, CS, C_2H, HCN, and U89.2 (see Table 2). Absorption by OH ground and excited states ($^2\Pi_{3/2}$, $J = 5/2$) has recently been reported by Rydbeck, Elldér, and Yngvesson 1973*b*).

W3OH exhibits strong OH ground- and excited-state ($^2\Pi_{3/2}$, $J = 5/2$; $^2\Pi_{1/2}$, $J = 1/2$) as well as H_2O radiation, and also millimeter-wave emission from CO, H_2S, NH_3, CS, C_2H, HCN, H_2CO, U89.2, and 90.7 (see Table 2). VLBI measurements have shown that the OH ground-state and H_2O maser emission comes from a number of small, dense condensations or "bright knots."

Six-centimeter H_2CO absorption and CO emission are found throughout the entire W3 region (Minn and Greenberg 1973*b*; Wilson *et al.* 1974).

We have searched for CH in nine directions toward the W3 region, entered with antenna temperature bars in Figure 22. We find two main CH velocity components, at about -40 km s^{-1} (in the direction of W3C1) and -48 km s^{-1} (in the directions of W3OH and the position 15′ south of the same). The line widths are about equal in the three cases, 4 km s^{-1}.

The spectra toward W3C1 (Fig. 23) show a strongly enhanced lower satellite transition. Its shape agrees quite well with the H_2CO and main line OH absorption lines (Zuckerman *et al.* 1970; Rydbeck, Elldér, and Yngvesson 1973*b*; Chaisson 1974). It appears from Figure 22 that the enhancement of the lower satellite line at about -40 km s^{-1}, marked with open antenna temperature bars, is well correlated with the continuum background and, most likely, with the far-infrared flux. Figure 22 indicates that there is also CH emission around -40 km s^{-1} associated with the W3C2 region. In this direction CO has been found at the same velocity (Wilson *et al.* 1974). It is interesting to note that Yngvesson and Rydbeck (1973, unpublished data), who used a 22 GHz maser on the Haystack telescope, searched for H_2O emission toward W3C2 but found none.

The second feature, at about -48 km s^{-1} and marked with solid antenna temperature bars in Figure 22, is concentrated toward the southern part of the region, almost with LTE line ratios. The position of maximum CH intensities is 15′ south of W3OH and corresponds to a continuum minimum. H I self-absorption is found in this direction, as well as 6 cm H_2CO and ground-state OH absorption (Höglund and Andersson 1974). These characteristics suggest the presence of a dark dust cloud.

The CH velocities agree well with those found for the extended H_2CO clouds identified by Minn and Greenberg (1973*b*). A CO mapping performed by Wilson *et al.* (1974) shows the presence of an extended cloud at about -40 km s^{-1} with maximum emission in the direction of W3C1, and a -47 km s^{-1} feature toward W3OH. Many other molecules also display about the same velocities in the W3C1 and W3OH molecular clouds (cf. Table 2).

Finally it should be mentioned that the H109α line has been found toward W3C1, centered around -42 km s^{-1} (Reifenstein *et al.* 1970). Several carbon recombination lines have also been detected, at about -41 km s^{-1} (see Table 2).

Quite generally, the CH clouds appear to have about the same extensions as the other molecular clouds. The more dense regions are perhaps exceptions, where CH may partly disappear by chemical reactions to form more stable molecules. The very weak CH emission in the direction of W3OH may indicate such a depletion of CH in

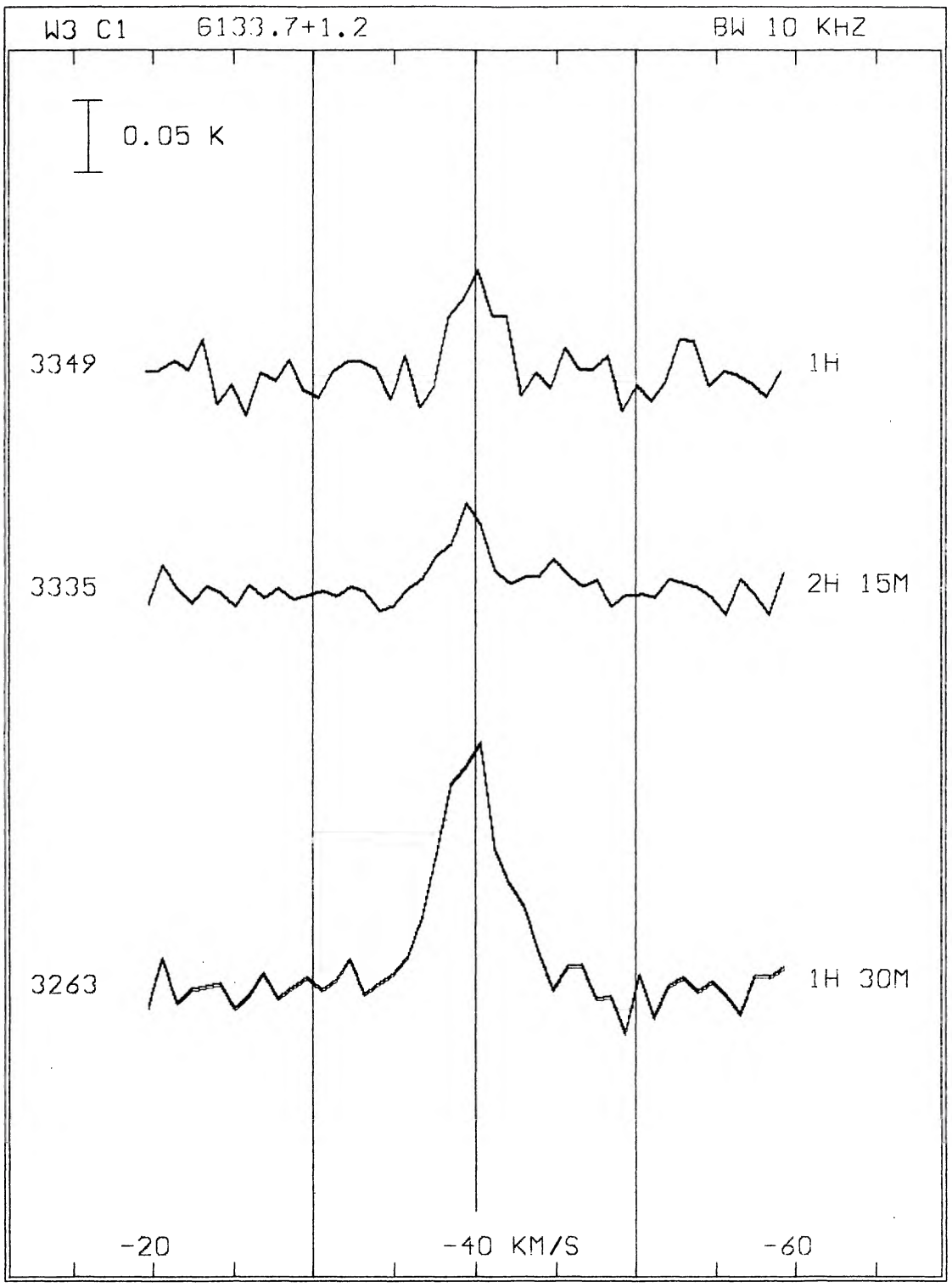

FIG. 23.—CH spectra in the direction of W3C1

very dense condensations (cf. also § VIII*a*). Therefore, CH clumping effects are likely also to reflect chemical reactions (in contrast with CO, for example, and partly also with OH, which have much longer lifetimes than CH).

xvii) *G209.0−19.4 (W10, Orion A, NGC 1976, M42); L1641*

The thermal radio source Ori A is associated with the Orion nebula, a well-known H II region in the Orion spiral arm at a distance of about 0.5 kpc (Schraml and Mezger 1969; Goss and Shaver 1970). In addition to the strong central source (M42), there is a considerably weaker secondary source (M43) about 8′ northwest of the main peak. The radio contours of the central region of the main source match the optical nebula reasonably well. A summary of the pre-1970 data on the structure of the H II region, associated OH and H_2O maser sources, and infrared sources has been given by Mezger (1970). Ori A is surrounded by the extended, diffuse, dark dust cloud L1641.

Ori A contains a very rich molecular cloud with dimensions of the order of 10′, with lines of OH, H_2O, H_2CO, CO, SiO, SO, H_2S, NH_3, CN, CS, C_2H, HCN, HCCCN, CH_3OH, $(CH_3)_2O$, CH_3NH_2, U72.4, U89.2, U90.1, U90.7, and U93.2 (see Table 2). The center of molecular emission lies about 1′ northwest of the continuum peak, close to the Kleinmann-Low infrared nebula. The water and OH sources lie in the direction of the center of the molecular cloud. H_2CO, CO, and CS are observed over a region much more extended than the main molecular cloud (Kutner and Thaddeus 1971; Davies 1973; Liszt *et al.* 1974; Phillips *et al.* 1974; Linke and Wannier 1974). Ori A is also a strong source of far-infrared radiation and millimeter-wave continuum radiation, which mainly originate in the Kleinmann-Low nebula (Erickson *et al.* 1973; Emerson, Jennings, and Moorwood 1973; Harvey *et al.* 1974; Gezari *et al.* 1974; Soifer and Hudson 1974; Fazio *et al.* 1974; Harper 1974); the size of this source is a few arcmin.

Models of the Ori A complex have been developed by Wurm (1961) and more recently by Zuckerman (1973) and ter Haar and Pelling (1974). The latter authors place the molecular cloud behind the H II region. Kutner and Thaddeus (1971) interpret their observations in a similar way, i.e., that the very extended H_2CO cloud must also lie behind the H II region.

We have found CH emission in all observed points toward L1641 on and around Ori A, as shown in Figure 24. The peak velocities lie in the range +7 to +9 km s^{-1}, in agreement with those obtained for the extended H_2CO cloud, for most molecules in the molecular cloud, and for the carbon recombination lines (see Table 2). The hydrogen recombination line velocities, on the other hand, lie at about −3 km s^{-1}. The CH emission does not peak at the continuum maximum, as it does in the direction of many other H II regions. This strongly leads us to suggest that the extended CH cloud also lies behind the H II region.

Near the continuum maximum (and hence near the Kleinmann-Low nebula) the CH lower satellite line is comparable in intensity to the main line (see Fig. 24). Since the continuum background is weak, the lower satellite transition could still be anomalously inverted (cf. Table 1). Far-infrared radiation is the most likely reason for this anomaly.

It is interesting to compare the CH line strengths and widths with those reported for the 6 cm H_2CO transition by Kutner and Thaddeus (1971). These authors found a "self-reversed" line profile at the position of the Kleinmann-Low nebula, which they interpret as arising from H_2CO emission in a region of high density. Zuckerman and Ball (1974), however, find in the same direction only a dominant H_2CO absorption feature at about +6 km s^{-1}, which they suggest may arise from a foreground cloud. OH (Goss 1968; Weaver, Dieter, and Williams 1968; Chaisson 1974), and H I (Radhakrishnan *et al.* 1972*b*) absorptions occur at the same velocity.

Our CH profiles toward the continuum maximum (Fig. 24) are quite broad and have an indication of a component at +6 km s^{-1}, as well as a more pronounced one at +9 km s^{-1}, characteristic of the molecular cloud (see Table 2). The adjacent point to the north also suggests the presence of two CH velocity components, now at about +8 and +11 km s^{-1}, the latter being stronger. This point is located only about 4′ northwest of the recently discovered second infrared complex and molecular cloud (OMC-2) about 12′ north of the Kleinmann-Low nebula. This cloud displays very narrow lines of CO, NH_3, HCN, U89.2, and U90.7 at about +11 km s^{-1}, with intensities comparable to the same lines in the Kleinmann-Low nebula (Gatley *et al.* 1974; Fazio *et al.* 1974; Morris *et al.* 1974*b*; Werner *et al.* 1974). To the south and west of the continuum maximum our profiles typically are considerably narrower, with peak intensities at +8 to +9 km s^{-1}. In these latter points the CH emission is stronger, but we do not find the very pronounced increase in line intensity shown by H_2CO at 6 cm. For comparison we also observed the OH 1667 MHz line 30′ south of the continuum maximum. We found emission at +9 km s^{-1}, with approximately the same width as the CH main line.

These different molecular data seem to indiate that the +6 km s^{-1} foreground cloud is confined to a small region at the continuum maximum. Radhakrishnan *et al.* 1972*a*) found an extension less than a few arcmin from H I interferometer observations. Our observations are thus consistent with the Zuckerman model, which places the H II region between a background extended slab of gas (containing for example CO, CS, H_2CO, OH, and CH) surrounding a denser molecular cloud, and a foreground H I region at +6 km s^{-1} containing H_2CO, OH, and CH.

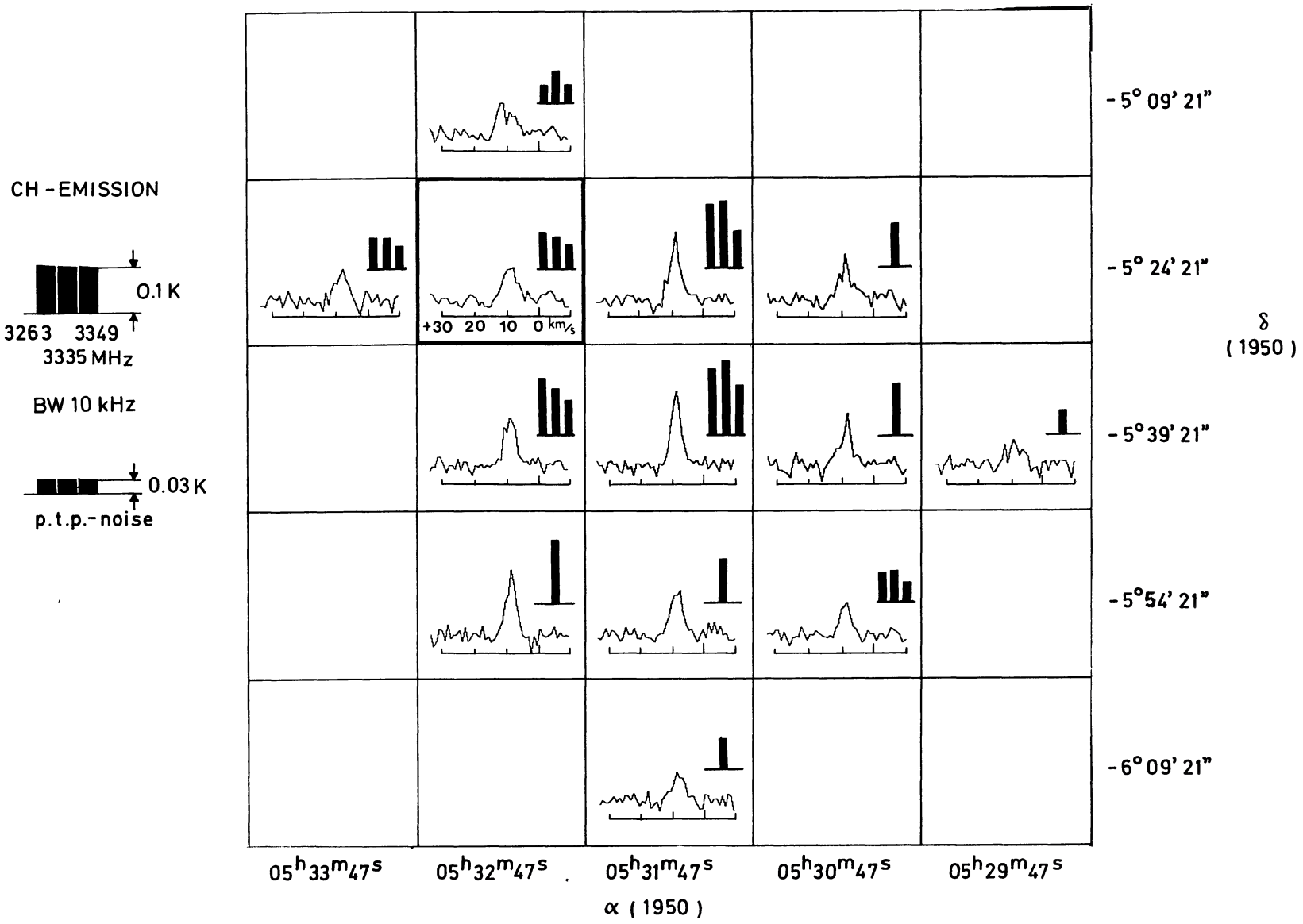

FIG. 24.—CH main line spectra of the region around W10 (Orion A). The bars represent the CH peak antenna temperatures at about +9 km s^{-1} for all three lines as shown at left. When only one bar is present in a square, the satellite lines have not been observed. Orion A and the main molecular cloud are contained within the area outlined by heavy lines. The molecular cloud and infrared complex OMC-2 is about 12′ north of Orion A, exhibiting a +11 km s^{-1} CH feature.

xviii) *G6.7−0.3 (W28 SNR)*

The radio source W28 consists of two H II regions, G7.0−0.2 (M20) and G5.9−0.4 (W28A2), and a nonthermal shell source centered on G6.4−0.2, which has been identified as a supernova remnant (Milne and Hill 1969; Milne and Wilson 1971). It is not clear whether the thermal and nonthermal sources are associated. Distance estimates to the supernova remnant vary from 1 to 4 kpc (Shaver and Goss 1970; Milne 1970; Wilson 1970, 1972; Milne and Wilson 1971; Lozinskaya 1974), and are uncertain due to the closeness to the galactic center direction.

Our CH observations of the main line toward the supernova remnant show emission features at about +7 and +21 km s^{-1}. OH main line and H I absorptions cover this velocity interval (Robinson, Goss, and Manchester 1970; Radhakrishnan *et al.* 1972*b*; Pastchenko and Slysh 1974), with maximum absorptions appearing about +6 km s^{-1}. Formaldehyde absorption features have been detected at +5 and +21 km s^{-1} (Wilson 1970, 1972), as well as CO emission around +22 km s^{-1} (Wilson *et al.* 1974).

xix) *G10.6−0.4 (W31)*

The W31 region contains three main H II condensations, G10.2−0.3, G10.3−0.1, and G10.6−0.4, which are believed to be associated (Goss and Shaver 1970; Wilson 1974). No optical nebulosity appears to be related to the radio objects. The minimum distance to the sources is estimated to be 5 kpc (Wilson 1974).

We have detected weak CH main line emission at about −1 km s^{-1} toward G10.6−0.4, close to the H109α recombination line velocity (Reifenstein *et al.* 1970). OH and H_2O maser emission has also been detected around zero velocity (Yngvesson *et al.* 1973, 1975; see also Table 2), whereas OH absorption occurs at +15 and +27 km s^{-1} (Wilson 1974). H_2CO absorption features are found at these two velocities, as well as at −3 and +37 km s^{-1} (Wilson 1974). CO emission appears around −3 (strongest), +17, and +30 km s^{-1} (Wilson *et al.* 1974).

b) Discussion of Observed and Calculated CH Properties in Tables 1 and 2

i) *Table 1 Data; CH Excitation Temperatures, Opacities, and Column Densities*

In this Table we have presented observed and calculated CH data together with available abundance information on OH, H_2CO, CO, and H I. The upper and lower CH satellite line excitation temperatures, T_x, listed in column (7), have been determined by means of relation (3) of the Cas A paragraph (cf. also equation [12]), with $T_{CR,1}$ taken from column (6). We here assume $T_B = 3$ K and $\rho_{10} = 0.6$ (i.e., the antenna main beam filled by the CH cloud). To be able to estimate the satellite line excitation temperatures for all clouds we have adopted one and the same value, $T_{x,m} = -15$ K, for the main line, guided by the approximate agreement between our Cas A and W12 results. Even if this is probably a very rough approximation, it allows us to estimate and discuss the population differences of the three CH transitions. The normalized population difference I for a transition $q \rightarrow p$ is related to its excitation temperature by (N_q, N_p are population densities; g_q, g_p statistical weights)

$$I \equiv \left(N_q - \frac{g_q}{g_p} N_p\right) \Big/ \left(N_q + \frac{g_q}{g_p} N_p\right) \approx -\frac{h\nu}{2kT_x} \quad \left[\left(\frac{h\nu}{kT_x}\right)^2 \ll 1\right], \tag{11}$$

where, for the CH ground state, $h\nu/k \approx 0.16$ K, i.e. $I_m \approx 0.5$ percent for $T_{x,m} = -15$ K.

Opacities at line center for the three transitions, calculated from relation (6) of the Cas A paragraph, and total column densities for the CH $^2\Pi_{1/2}$, $J = 1/2$ state, obtained from main line data by means of relation (7), are presented in columns (8) and (9), respectively. $R_0 = 1$ (no clumping), $\rho_{10} = 0.6$, $T_{x,m} = -15$ K, and $T_B = 3$ K were assumed. A planimeter was used to determine the area under the different spectral features expressed by the integral in relation (7). For the few cases where only lower satellite emission is visible, we assume $T_{x,s} = -1$ K for this line, a value suggested by similar sources in the table. The column densities were then calculated from the lower satellite spectrum with the appropriately modified relation (7), i.e. replacing the constant 2.9 by 5.4 (Burdyuzha and Varshalovich 1973).

Excitation Temperatures.—Our estimated excitation temperatures for the two CH satellite transitions show a considerable scatter (see col. [7] of Table 1). To investigate this we note that, by relations (3) and (11),

$$\frac{I_s}{I_m} = \frac{T_{x,m}}{T_{x,s}} = 1 + 2(Q_{sm} - \tfrac{1}{2})\left(1 - \frac{T_{x,m}}{T_{tb}}\right), \tag{12}$$

where I_s/I_m is the ratio between the normalized satellite and main line population differences, $T_{tb} = T_B + T_{CR}/\rho_{10}$ ($T_B \approx 3$ K), and $Q_{sm} = T_{A,s}/T_{A,m}$ is the ratio between the observed satellite and main line antenna temperatures. For $T_{x,m} < 0$, it is clear that $Q_{sm} \geq 1/2$ means $I_s \geq I_m$ ($|T_{x,s}| \leq |T_{x,m}|$), while $Q_{sm} \leq 1/2$ yields $I_s \leq I_m$. Table 1 and relation (12) therefore clearly demonstrate that, with only a few exceptions (weak signals, low confidence), *both the upper and lower satellite transitions are more inverted than the main line*, an interesting fact that will be discussed at some length in connection with our CH pumping considerations.

We will now discuss the influence on the estimated satellite line excitation temperatures, $T_{x,s}$, of our assumption that $T_{x,m} = -15$ K for all clouds. From relation (12) we find that for stronger background sources the ratio $I_s/I_m = T_{x,m}/T_{x,s}$ does not critically depend upon the value of $T_{x,m}$, while for weaker backgrounds this ratio may assume

TABLE 1

OBSERVATIONS OF H I AND H II REGIONS

Galactic Source Number	Position (1950) RA	DE	Antenna Temp. K F=1–0	F=1–1	F=0–1	Velocity (LSR) km s^{-1} F=1–0	F=1–1	F=0–1	Full Width at Half Intensity km s^{-1} F=1–0	F=1–1	F=0–1	T_{CR} K	T_x^+ K F=1–0	F=0–1	τ F=1–0	F=1–1	F=0–1	N_{OH} 10^{13} cm^{-2}	N_{OH}/T_{OH} 10^{13} cm^{-2} K^{-1}	N_{H_2CO}/T_{H_2CO} ^{a} 10^{12} cm^{-2} K^{-1}	N_{CO} 10^{18} cm^{-2}	N_{HI} 10^{20} cm^{-2}
(1)	(2)		(3)			(4)			(5)			(6)	(7)		(8)			(9)	(10)	(11)	(12)	(13)
G6.7–0.3	17^{h}58^{m}50^s	–23°19'00"	–	0.06	–	–	+7	–	–	3	–	2	–	–	–	–0.005	–	7	32[b]	8[c]	–	15[d]
(W28)			–	0.07	–	–	+21	–	–	5	–	2	–	–	–	–0.005	–	11	–	7[c]	–	2[d]
G10.6–0.4 (W31)	18 07 34	–19 56 30	**	0.04	**	–	–1	–	–	4	–	1	–	–	–	–0.003	–	6	–	20[c]	8[e]	–
G15.0–0.7	18 17 29	–16 13 42	–0.03	–0.03	*	+15	+14	*	5	8	*	37	See text for this absorption feature						–	–	–	–
(M17)			*	*	0.17	*	*	+20	*	*	6	37	–	–1[f]	–	–	–0.004	2	7[g]	6[h]	6[e]	–
			0.13[i]	0.19[i]	0.16[i]	+24[i]	+24[i]	+24[i]	0.4[i]	0.9[i]	1.2[i]	37	–10	–7	–0.003	–0.004	–0.004	1	–	1[h]	–	–
G29.9–0.0	18 43 30	–02 45 00	0.02	0.04	–	+7	+7	–	*	3	–	3	–15	–	–0.001	–0.003	–	4	–	4[c]	–	–
(W43)			0.06	0.09	0.13	+100	+102	+100	9	9	6	3	–8	–2	–0.006	–0.007	–0.021	24	–	24[c]	8[e]	–
G30.6–0.0	18 44 44	–02 09 30	0.03	0.04	0.07	+82	+82	+82	2	2	3	6	–8	–3	–0.002	–0.002	–0.007	2	10[b]	7[j]	–	23[d]
G30.7–0.0 (W43)	18 45 01	–02 01 36	0.05	0.06	0.25	+94	+94	+93	4	4	5	9	–7	–1	–0.004	–0.004	–0.026	7	17[b]	37[j]	–	18[d]
G30.7–0.0	18 45 01	–02 01 36	0.05	0.07	0.07	+11	+13	+12	4	3	3	9	–8	–5	–0.003	–0.004	–0.005	4	3[b]	2[j]	–	15[d]
G30.9+0.0 (W43)	18 45 03	–01 48 18										4	–7	–4	–0.005	–0.005	–0.008	5	–	–	–	–
G34.3+0.1 (W44)	18 50 48	01 11 07	0.05	0.10	0.14	+58	+59	+59	7	7	7	1	–15	–2	–0.004	–0.008	–0.036	31	–	29[c]	–	–
G43.2–0.0	19 07 53	09 01 00	**	0.02	0.16	–	+16	+14	–	5	7	6	–	–0.5	–	–0.001	–0.020	3	–	25[c]	2[k]	–
(W49)			0.02	0.04	0.02	+41	+41	+41	8	8	8	6	–15	–15	–0.001	–0.002	–0.001	7	4[l]	3[c]	–	–
			0.04	0.08	0.07	+63	+63	+61	9	9	7	6	–15	–6	–0.002	–0.005	–0.006	18	4[l]	4[c]	–	–
G49.2–0.3	19 20 25	14 09 36	0.04	0.08	0.07	+6	+6	+6	3	3	3	7	–15	–6	–0.002	–0.004	–0.006	5	4[g]	–	–	7[d]
(W51)			0.05	0.08	0.16	+62	+63	+63	7	8	7	7	–10	–2	–0.003	–0.004	–0.016	13	25[m]	33[c]	–	23[d]
G49.4–0.2	19 20 25	14 24 36	0.03	0.07	0.05	+6	+6	+6	*	3	3	3	–26	–7	–0.001	–0.005	–0.006	7	4[m]	–	–	–
(W51)			0.05	0.10	0.15	+63	+64	+64	5	5	4	3	–15	–2	–0.004	–0.007	–0.024	15	24[m]	–	–	–
G49.5–0.4	19 21 27	14 24 36	**	0.03	0.04	+6	+6	+6	*	*	3	12	–	–4	–	–0.001	–0.002	2	4[m]	–	–	6[d]
(W51)			**	**	0.08	–	–	+57	–	–	7	12	–	–1[f]	–	–	–0.006	2	7[m]	–		–
			0.08	0.08	0.37	+66	+66	+66	4	3	4	12	–6	–1	–0.005	–0.004	–0.025	6	25[m]	43[c]	25[e]	24[d]
			*	*	*	+69	+69	+69	*	*	*	12	–	–	–	–	–		16[m]			

TABLE 1—*Continued*

Galactic Source Number	Position (1950) RA	DE	Antenna Temp. K F=1-0	F=1-1	F=0-1	Velocity (LSR) km s^{-1} F=1-0	F=1-1	F=0-1	Full Width at Half Intensity km s^{-1} F=1-0	F=1-1	F=0-1	T_{CR} K	T_x^+ K F=1-0	F=0-1	τ F=1-0	F=1-1	F=0-1	N_{CH} 10^{13} cm^{-2}	N_{OH}/T_{OH} 10^{13} cm^{-2}K^{-1}	N_{H_2CO}/T_{H_2CO}[a] 10^{12} cm^{-2}K^{-1}	N_{CO} 10^{18} cm^{-2}	N_{HI} 10^{20} cm^{-2}
(1)	(2)		(3)			(4)			(5)			(6)	(7)		(8)			(9)	(10)	(11)	(12)	(13)
G69.5-1.0 (ON1)	$20^h08^m10^s$	31°22'41"	0.02	0.06	0.03	+11	+11	+11	4	3	3	0.3	(+20)	-15	(+0.002)	-0.005	-0.003	9	-	-	-	-
G70.3+1.6 (ON3,K3-50)	19 59 59	33 25 57	**	**	0.05	-	-	-22	-	-	3	1	-	-1[f]	-	-	-0.015	3	-	14[j]	10[e]	-
G75.8+0.3 (ON2)	20 19 52	37 17 03	0.02	0.03	0.04	-3	-3	-2	4	3	6	1	-6	-2	-0.003	-0.003	-0.010	6	-	-	-	-
			0.03	0.07	0.04	+4	+4	+4	4	6	6	1	-38	-9	-0.001	-0.006	-0.005	15	-	-	-	-
G78.5+1.2 (DR5)	20 24 08	40 00 20	0.03	0.03	0.03	-3	-3	-3	5	5	5	3	-4	-4	-0.004	-0.002	-0.004	3	3[n]	-	-	-
			0.07	0.14	0.10	+1	+1	+1	2	2	2	3	-15	-7	-0.005	-0.010	-0.011	11	4[g]	-	-	-
G79.2+0.3 (DR15)	20 30 22	40 03 00	*	*	*	-3	-3	-3	*	*	*	1	-	-	-	-	-	} 13	-	-	-	-
			0.05	0.08	0.05	+1	+1	+1	3	3	3	1	-7	-7	-0.007	-0.007	-0.007		3[n]	-	-	-
			0.02	0.04	0.02	+8	+9	+9	3	4	3	1	-15	-15	-0.002	-0.003	-0.002	5	-	-	-	-
G80.9-0.2 (DR22)	20 37 42	41 07 35	0.02	0.03	0.04	-2	-2	-3	3	4	3	2	-7	-2	-0.002	-0.002	-0.008	4	3[n]	-	-	-
			0.07	0.12	0.10	+6	+6	+6	4	4	4	2	-10	-5	-0.007	-0.009	-0.015	18	7[n]	9[c]	-	-
G81.7+0.5 (DR21)	20 37 14	42 09 00	0.05	0.08	0.12	-3	-3	-3	3	3	3	3	-9	-2	-0.005	-0.006	-0.019	11	40[n]	35[c]	13[e]	-
			0.05	0.09	0.06	+8	+8	+8	3	3	3	3	-11	-8	-0.004	-0.007	-0.006	10	7[n]	6[c]	-	-
G84.7-1.0 (NGC7000)	20 54 23	43 30 00	0.06	0.10	0.06	+1	+1	+1	6	7	6	0.4	-7	-7	-0.009	-0.009	-0.009	21	60[o]	-	-	-
G84.9-1.0 (NGC7000)	20 55 00	43 40 00	0.07	0.08	0.07	+2	+3	+3	5	5	5	0.5	-3	-3	-0.016	-0.007	-0.016	17	7[g]	-	-	-
G111.5+0.8 (NGC7538)	23 11 37	61 12 00	*	0.02	0.02	*	-56	-56	*	3	*	2	-	-3	-	-0.002	-0.003	1	-	} ≈50[p]	10[e]	-
			0.02	0.05	0.02	-52	-52	-52	*	4	*	2	-46	-46	-0.001	-0.004	-0.001	7	-		-	-
G111.7-2.1 (Cas A)	23 21 11	58 32 48	0.18	0.25	0.24	-47	-47	-46	4	4	4	85	-10	-7	-0.002	-0.003	-0.003	4	4[g]	1.9[j]	⩽0.3[e]	37[q]
			0.11	0.18	0.14	-40	-40	-40	3	3	3	85	-12	-9	-0.001	-0.002	-0.002	3	3[g]	1.5[j]		18[q]
			0.10	0.16	0.11	-37	-37	-36	3	3	3	85	-12	-11	-0.001	-0.002	-0.001	2	2[g]	1.2[j]		11[q]
			0.16[i]	0.16[i]	0.20[i]	-1.4[i]	-1.4[i]	-1.4[i]	0.7[i]	1.2[i]	0.9[i]	85	-7	-6	-0.002	-0.002	-0.002	1	1[g]	0.6[j]		2[q]
			0.10[i]	0.15[i]	0.12[i]	-0.1[i]	-0.1[i]	-0.1[i]	0.8[i]	0.9[i]	1.0[i]	85	-11	-9	-0.001	-0.002	-0.001	1	1[g]	0.5[j]		5[q]

TABLE 1—*Continued*

Galactic Source Number	Position (1950) RA	DE	Antenna Temp. K			Velocity (LSR) km s^{-1}			Full Width at Half Intensity km s^{-1}			T_{CR} K	T_x^+ K		τ			N_{CH} 10^{13} cm^{-2}	N_{OH}/T_{OH} 10^{13} cm^{-2} K^{-1}	N_{H_2CO}/T_{H_2CO} [a] 10^{12} cm^{-2} K^{-1}	N_{CO} 10^{18} cm^{-2}	N_{HI} 10^{20} cm^{-2}
			F=1-0	F=1-1	F=0-1	F=1-0	F=1-1	F=0-1	F=1-0	F=1-1	F=0-1		F=1-0	F=0-1	F=1-0	F=1-1	F=0-1					
(1)	(2)		(3)			(4)			(5)			(6)	(7)		(8)			(9)	(10)	(11)	(12)	(13)
G118.1+5.0	23^{h}58^{m}35^s	67°05'00"	0.03	0.03	0.04	-13	-13	-13	2	3	3	2	-3	-2	-0.005	-0.002	-0.008	4	2[g]	-	-	-
(W1)			**	0.02	0.03	-	-7	-7	-	3	3	2	-	-2	-	-0.002	-0.006	2	1[g]	-	-	-
G133.7+1.2 (W3 C1)	02 21 55	61 52 00	0.07	0.06	0.17	-40	-40	-40	4	3	4	6	-4	-1	-0.007	-0.004	-0.020	5	15[r]	9[c]	6[e]	-
G133.9+1.1 (W3 OH)	02 23 17	61 39 00	0.01	0.02	0.01	-48	-48	-48	3	3	3	1	-15	-15	-0.001	-0.002	-0.001	2	-	14[s]	3[e]	-
G134.0+0.8 (W3)	02 23 17	61 24 00	0.04	0.07	0.04	-49	-49	-49	5	4	4	0.4	-9	-9	-0.005	-0.006	-0.005	10	-	13[t]	-	-
G205.3-14.3	05 44 12	00 02 18	0.02	0.04	0.02	+6	+6	+6	4	4	4	<1	-15	-15	-0.002	-0.003	-0.002	6	-	~	-	-
(NGC2068)			0.06	0.12	0.08	+11	+11	+11	3	2	2	<1	-15	-6	-0.005	-0.010	-0.012	10	-	10[u]	6[v]	-
G206.6-16.4	05 39 12	-01 57 42	*	*	*	+6	+6	+6	*	*	*	5	-	-	-	-	-	} 15	43[w]	10[c]	8[e]	} 8,30[x]
(W12)			0.08	0.13	0.20	+10	+10	+10	3	3	2	5	-10	-3	-0.006	-0.008	-0.024					
			*	*	*	+13	+13	+13	*	*	*	5	-	-	-	-	-					
G208.0-16.5 (L1630)	05 41 12	-03 12 42	0.02	0.03	0.02	+8	+8	+8	7	7	7	<1	-5	-5	-0.004	-0.003	-0.004	8	-	-	-	-
G208.8-19.3	05 32 47	-05 09 21	0.03	0.04	0.03	+8	+8	+8	*	3	*	<1	-4	-4	-0.007	-0.004	-0.007	5	-	-	-	-
(Ori A)			0.06	0.06	0.05	+11	+11	+11	*	4	*	<1	-2	-3	-0.019	-0.006	-0.014	8	-	-	-	-
G208.9-19.6	05 31 47	-05 24 21	*	*	*	+6	+6	+6	*	*	*	<1	-	-	-	-	-	} 22	-	-	-	-
(Ori A)			0.07	0.14	0.13	+9	+9	+9	3	3	3	<1	-15	-2	-0.006	-0.013	-0.039					
			*	*	*	+12	+12	+12	*	*	*	<1	-	-	-	-	-					
G209.0-19.4	05 32 47	-05 24 21	*	*	*	+6	+6	+6	*	*	*	29[y]	-	-	-	-	-	} 17	0.5[g]	-	-	10[d]
(Ori A)			0.04	0.07	0.07	+9	+9	+9	6	6	6	-	-8	-2	-0.006	-0.006	-0.022		-	-	15[e]	-
G209.1-19.7 (Ori A)	05 31 47	-05 39 21	0.10	0.16	0.15	+9	+9	+9	4	4	3	<1	-6	-2	-0.018	-0.015	-0.045	23	-	10[z]	-	-

NOTES TO TABLE 1

(a) N_{H_2CO} is the population in the 0_{00}, 1_{11}, and 1_{10} levels (see Ref. j).
(b) Robinson *et al.* 1970; $T_x = T_B \approx 3$ K.
(c) Wilson (1972); $T_x = T_B \approx 3$ K. The column densities for the 1_{11} level have been multiplied by 2.2 to account for population in the 1_{10} and 0_{00} levels.
(d) Radhakrishnan *et al.* 1972*b*; $T_x = 50$ K.
(e) Wilson *et al.* 1974.
(f) Assumed value.
(g) Goss 1968; $T_x = 3$ K.
(h) Lada and Chaisson 1975; $T_x = 1.7$ K (cf. Ref. j).
(i) From 1 kHz resolution data smoothed to 3 kHz.
(j) Zuckerman *et al.* 1970; $T_x = 3$ K?
(k) Scoville and Solomon 1973.
(l) Calculated from data by Pastchenko and Slysh 1973; $T_x = 3$ K.
(m) Slysh 1973; $T_x = T_B \approx 3$ K.
(n) Pashchenko 1974; $T_x = T_B \approx 3$ K.
(o) Turner 1973; $T_x \approx 10$ K, main beam filling factor 0.7.
(p) Estimated from the column density given by Minn and Greenberg 1975 for the point of maximum absorption of complex 1. $T_x = 1.7$ K.
(q) Davies and Matthews 1972; $T_x = 100$ K, except for their -1.9 km s^{-1} component, where $T_x = 50$ K.
(r) Calculated from data by Chaisson 1974; $T_x = 3$ K.
(s) Wilson's 1972 value reduced to account for nonzero $T_x - T_B$ which cannot be neglected in this case in comparison with continuum source contribution. $T_x = 1.5$ K is assumed.
(t) Höglund and Andersson 1974; $T_x = 1.5$ K.
(u) Dieter 1973.
(v) Calculated from data by Tucker *et al.* 1973.
(w) Goss *et al.* 1975; $T_x = 4.2$ K, main beam filling factor 0.3.
(x) From d. Single dish and interferometer value, respectively.
(y) Continuum source assumed between $+6$ and $+9$ km s^{-1} clouds.
(z) Calculated from data by Kutner and Thaddeus 1971; $T_x = 1.5$ K.
$^+$ T_x assumed to be -15 K for the main line ($F = 1$–1).
* Feature too weak or blended to permit any value.
** No feature above the noise level.

large values even for very moderate deviations of the observed Q_{sm} from 1/2. If $Q_{sm} < 1/2$, even $T_{x,s} > 0$ may result, probably erroneously, as for the source G69.5−1.0 (ON 1).

Thus it is obvious that the probable errors in our estimated satellite line excitation temperatures increase with decreasing continuum background. It is quite possible that the real $T_{x,s}$ values do not vary much among the CH clouds associated with weak background. For such clouds the great scatter evident from column (7) of Table 1 may just indicate, besides the observational uncertainties, that our assumed $|T_{x,m}|$ is too large and/or that the value $\rho_{10} = 0.6$ should be considerably reduced (for the smaller clouds). If we instead assume that $T_{x,m} = -5$ K (greater main line inversion) which is still within the error bounds of our Cas A and W12 determinations, the great variations of I_s/I_m ($=T_{x,m}/T_{x,s}$) are considerably reduced for the weaker backgrounds, and also the ON 1 upper satellite line excitation temperature becomes negative. Even though we cannot definitely exclude the possibility that the satellite line pumping conditions may vary drastically among these clouds (with weak background sources), we prefer to believe that $T_{x,m}$ is probably closer to -5 than -15 K, and that it also varies from cloud to cloud. It is also quite natural that in many cases $\rho_{10} < 0.6$ (i.e., that the clouds do not fill the main beam of the antenna).

Contrary to these somewhat indefinite cases, there are "normal" H I spiral arm clouds for which the enhanced satellite line inversions are clearly established, e.g., toward W43, W51, and Cas A, where both the signal strengths and the continuum backgrounds are high enough.

The most striking examples of strongly enhanced lower satellite line inversions are found for the CH clouds associated with the H II regions M17, W43, W44, W49, W51, K3–50 (ON 3), DR 21, W3C1, W12, and W10 (in order of galactic longitude). For some of these clouds (toward W49, W51, and K3–50) the main line is barely visible in (part of) the enhanced lower satellite velocity interval. Toward a few sources the lower satellite spectrum contains more than one strongly enhanced feature (e.g., W43, W44, W49, and W51), which probably implies that we observe contributions from more than one region of anomalous lower satellite pumping. This has already been discussed for the individual sources. There seems to be a definite correlation between strong enhancement of the lower satellite population inversion (e.g., for the W49 $+15$ km s^{-1} cloud, $I_s/I_m \approx 30$) and observed far-infrared flux (W49 is also the most luminous far-infrared source) believed to emanate from dust, heated by the Lyman ultraviolet flux from the very same O-type star(s) responsible for the ionization of the H II region (cf. Neugebauer, Becklin, and Hyland 1971; Caroff *et al.* 1973; Johnson 1973; Wynn-Williams and Becklin 1974; Pottasch 1974; Panagia 1974). A possible far-infrared pumping model was already suggested by Rydbeck *et al.* (1974*b*), and will be discussed at some length in a following section. In Table 3 we have listed information on far-infrared luminosities for those H II regions where such data are available. The CH satellite-to-main-line antenna temperature ratios (Q_{um} = upper to main; Q_{lm} = lower to main) are also given, together with ratios between the normalized satellite (I_u, I_l) and main (I_m) line population differences calculated by means of relation (11) or (12).

Opacities.—Even though the excitation temperatures used for the opacity calculations are very uncertain, there is no doubt that the CH main and satellite lines are optically thin. The absolute values of the listed opacities are all below 0.05, but since in all calculations we have assumed $R_0 = 1$ (no clumping), this limit must be considered too low; cf. relation (6).

Column densities.—The CH column densities listed in Table 1 are of the order of 10^{14} cm^{-2}. As was already discussed for Cas A, the accuracy of a column density estimation is rather low. Relation (7) demonstrates that our choice of $\rho_{10} = 0.6$ and $R_0 = 1$ results in lower limits to the column densities, and also indicates that for the

weaker continuum sources N_{CH} is not *critically* dependent on the value of $T_{x,m}$. For the stronger background sources the dependence on $T_{x,m}$ increases.

We have also calculated the CH quantities of Table 1 assuming $T_{x,m} = -7.5$ K and $\rho_{10} = 0.6$, and furthermore with $T_{x,m} = -15$ K and $\rho_{10} = 0.3$. The changes in the numerical values of excitation temperatures and opacities were considerable, as expected from our earlier discussions. But the estimated column densities for most cases decreased or increased, respectively, by less than a factor 1.5. Relation (7) implies a variation by less than a factor 3 for all cases, if we allow the main line excitation temperature to vary between the bounds determined for Cas A (i.e. -5 to -45 K).

The comparison of CH densities with those of other species is deferred to § VIII, where theories of CH formation are also discussed.

ii) *Table 2 Data; Comparison of Molecular Velocities and Line Widths*

We have in this Table listed radial velocities and line widths of CH, OH, H_2CO, H I, ^{12}CO, ^{13}CO, and other observed "molecular cloud" species, together with hydrogen recombination line velocities for the observed regions. Adopted source distances and kinematic distances to the CH clouds, using the Schmidt (1965) galactic (circular) rotation model, are also given. For completeness, velocity information (emission interval and velocity of dominant peak) for ground- and excited-state OH and H_2O maser sources associated with the observed H II regions is also included.

The agreement between CH and other molecular velocities is very good (excluding the strong maser sources), remembering the limited velocity resolution for many millimeter-wave molecular lines. With a few exceptions the widths (typically a few km s^{-1}) of CH emission and OH and H_2CO absorption features are about the same. The emission lines of CO and the "molecular cloud" species are often somewhat broader, partly due to the sometimes poor millimeter line spectral resolution.[2] A detailed discussion of the general similarities and differences in velocities and widths among these various species is beyond the scope of the present communication. Velocities, widths, and other data for H I, OH, H_2CO, and CO have been extensively discussed (e.g., Goss 1968; Turner 1972*a*; Wilson 1972; Wilson *et al.* 1974). The (on average) small but seemingly definite velocity difference between the hydrogen recombination lines and the associated molecular cloud species suggested in these papers is supported by our CH data. However, this conclusion must be taken with some caution, since the observed H II velocities frequently must be a result of a superposition of recombination lines from several compact H II condensations in an extended diffuse background. A more definite interpretation must await high-angular-resolution recombination line observations of the compact H II regions revealed by the continuum aperture synthesis maps (referred to in our source descriptions).

c) *General Discussion of* CH *Spectra Observed towards* H I *and* H II *Regions*

Detailed discussions of the observed CH spectra have been given in the individual source descriptions. In this section we will consider some general characteristics of these spectra.

We find for an optically thin cloud the following simplified expression for the observed line antenna temperature as a function of radial velocity (cf. Rydbeck *et al.* 1975),

$$T_A(v) = RF(T_x - T_B)\tau(v) - R_0 T_{CR}\tau_0(v)\,, \tag{13}$$

where R and $\tau(v)$, R_0 and $\tau_0(v)$, are the average clumping factors and optical depths of (first) the entire cloud and (second) in front of the discrete background continuum source. The beam dilution factor is F. T_x is the excitation temperature of the observed transition, T_B denotes the diffuse background radiation temperature (≈ 3 K), and T_{CR} is the observed continuum antenna temperature of the discrete source. We furthermore find for the optical depths that

$$\tau(v) \propto \frac{N_c(v)}{T_x}\,, \tag{14}$$

and a corresponding relation for $\tau_0(v)$, where $N_c(v)$ is the column density as a function of radial velocity. We here allow $\tau(v)$ to differ from $\tau_0(v)$ [i.e. by equation [14], the average values of $N_c(v)$ and T_x over the cloud and in front of the discrete background source may be different).

From relations (13) and (14) it is evident that (*a*) *for* $T_x > 0$ ($\tau > 0$) we will observe *emission* if $RF(T_x - T_B)\tau(v) > R_0 T_{CR}\tau_0(v)$. The emission will *decrease* when the continuum background (T_{CR}) *increases*, even to the point that an *absorption* feature may appear, if T_{CR} becomes large enough. For $T_x < T_B$ an absorption line always results (as for 6 cm H_2CO). (*b*) *for* $T_x < 0$ ($\tau < 0$) we can only observe (maser) *emission lines*. The line intensity will *increase* when the continuum background (T_{CR}) *increases*. The sensitivity to variations of T_{CR} becomes greater when $|T_x|$ decreases. (*c*) *Toward the stronger continuum sources* we may expect, assuming that the molecular species are well mixed, *a conspicuous similarity in shape* between absorption lines of H_2CO and OH (the latter sometimes disturbed

[2] The recently reported 2cm (2_{11}–2_{12}) H_2CO absorption studies by Evans *et al.* (1975) fit in with the Table 2 data.

TABLE 2

RADIAL VELOCITIES AND HALF-POWER WIDTHS (V_{LSR}, ΔV, km s^{-1}), ADOPTED CONTINUUM SOURCE DISTANCES (D_S, kpc), AND CLOUD KINEMATIC DISTANCES (D_{CL}, kpc)

Source	CH[a]		OH Abs.[b]		H_2CO Abs.[c]		HI Abs.		^{12}CO		^{13}CO		Other Molecules			H109α	D_S	D_{CL}	OH Emission[d]		H_2O Emission[e]	Remarks
	V_{LSR}	ΔV	V_{LSR}	ΔV	V_{LSR}	ΔV	V_{LSR}	ΔV	V_{LSR}	ΔV	V_{LSR}	ΔV	Species	V_{LSR}	ΔV	V_{LSR}	kpc	kpc	Line	V_{LSR}	V_{LSR}	
G6.7−0.3	+7	3	+6[f]	16	+5[g]	5	+7[h]	6	–	–	–	–	–	–	–	–	–	2	–	–	–	Distances uncertain
(W28)	+21	5	+21[i]	9	+21[g]	4	+18[h]	4	+22[j]	12	–	–	–	–	–	+14[m]	3–4	3–4	1720[f]	+11	–	due to closeness to Galactic center direction
G10.6−0.4	−1	4	–	–	−3[l]	6	–	–	−3[j]	12	−3[j]	7	–	–	–	0[m]	>5[l]	>5	1665[n]	(−3,0)	(−4,+5)[n]	– " –
(W31)			+15[l]	4	+15[l]	4	–	–	+17[j]	9	–	–	–	–	–	–	–	2	1667[n]	(−3,0)	–	
			+27[l]	6	+27[l]	4	–	–	+30[j]	15	+32[j]	12	–	–	–	–	–	4	–	–	–	
			–	–	+37[l]	5	–	–	–	–	–	–	–	–	–	–	–	5	–	–	–	
G15.0−0.7	+15A	7	–	–	–	–	–	–	–	–	–	–	SO[o]	+17	7	–	–	–	–	–	+13[p]	A denotes CH absorption.
(M17)	+20	6	+20[q]	8	+20[r]	13	(0,+30)[s,h]	–	+20[o]	8	+20[o]	5	NH_3[r]	–	–	+18[k]	2.5[h]	2.5	–	–	–	$C167\alpha$[t]:+21 km s^{-1}
	+24	<1	–	–	+24[r]	1	–	–	–	–	–	–	CS[r]	–	–	–	–	–	–	–	–	$C76\alpha$[pd]:+24 km s^{-1}
													C_2H[u]	+20	6							
													HCN[o]	+20	6							
													H_2CO[o]	+20	7							
G29.9−0.0	+7	3	+7[v]	2	+7[g]	3	+5[h]	10	–	–	–	–	–	–	–	–	–	0.5	–	–	–	
(W43)	+100	8	+100[w]	6	+100[g]	6	+100[h]	15	+100[j]	14	+99[j]	10	–	–	–	+96[m]	7,10[h]	7,10	1612[w]	+101	–	
G30.6−0.0	+82	2	+82[f]	6	+82[x]	3	+82[h]	14	+84[j]	12	–	–	–	–	–	–	–	6	1612[y]	+97	–	
G30.7−0.0	+94	4	+93[f]	6	+92[x]	7	+94[h]	12	+92[j]	15	–	–	NH_3[z]	+95	15	+92[m]	7[h]	7	1665[n]	(+86,+92)	+91[n,aa]	
(W43)																			1667[n]	(+86,+92)[ba]	(+92,100)[aa]	
																			1720[n]	(+83,+93)[ba]		
G30.7−0.0	+12	3	+12[f]	4	+14[x]	3	+13[h]	8	–	–	–	–	–	–	–	–	7[h]	1	–	–	–	
G30.9+0.0																						
(W43)																						
G34.3+0.1	+59	7	+60[w]	4[ca]	+60[g]	4	–	–	+55[j]	15	–	–	–	–	–	+54[m]	4[rd]	4,(13)	1665[n]	(+55,+60)	(+25,+80)[n,da]	
(W44)									+64[j]	9	–	–	–	–	–	–	–	–	1667[n]	(+56,+59)[ba]		
																			1720[n]	(+55,+60)[ba]		
G43.2−0.0	+15	6	+10[ea]	–	+14[g]	9	+10[h]	20	+3,+10[j]	9,9	+5,+12[fa]	10,5	CS[ga]	+9	14	+9[m]	14[h]	(1),14	1612[ha]	+15	(−200,+200)[ia,ja]	$C85\alpha$[ka]:+4 km s^{-1}.
(W49)			+17[ea]																			Possible carbon recombination line[ca] at +64 km s^{-1}
	+41	8	+40[ea]	11[la]	+40[g]	1	+38[h]	15	–	–	–	–	HCN[ma]	+6	18	–	–	3,11	1665[ha]	(0,+23)	–	
	+62	8	+63[ea]	4	+62[g]	2	+62[h]	23	–	–	–	–	U93.2[na]	+3,+10	–	–	–	5,9	1667[ha]	(0,+23)	–	
																			1720[ha]	+14		
																			4765[lc]	+8		
																			6035[lc]	(+9,+18)		

TABLE 2—*Continued*

Source	CH[a]		OH Abs.[b]		H_2CO Abs.[c]		HI Abs.		^{12}CO		^{13}CO		Other Molecules			H109α	D_S	D_{CL}	OH Emission[d]		H_2O Emission[e]	Remarks
	V_{LSR}	ΔV	V_{LSR}	ΔV	V_{LSR}	ΔV	V_{LSR}	ΔV	V_{LSR}	ΔV	V_{LSR}	ΔV	Species	V_{LSR}	ΔV	V_{LSR}	kpc	kpc	Line	V_{LSR}	V_{LSR}	
G49.2-0.3	+6	3	+6[q]	2	-	-	+6[h]	6	-	-	-	-	-	-	-	-	-	0.5	1720[pa]	+5	-	CH position
(W51)	+63	7	+65[qa]	7	+66[g]	3	+61[h]	14	+68[j]	9	-	-	-	-	-	+66[k]	6.5[h]	6.5	-	-	-	about 5′ W of HII region G49.2-0.3. $C248\alpha^{ra}$: +63 km s^{-1}
G49.4-0.2	+6	3	-	-	-	-	+6[sa]	-	-	-	-	-	-	-	-	-	-	0.5	-	-	-	CH position about
(W51)	+64	5	+63[qa]	5	+63[ta]	7	+62[sa]	-	+54,+66[j]	15,6	-	-	-	-	-	+53[k]	8[ua]	6.5	-	-	-	7.5′ NW of HII region G49.4-0.3
G49.5-0.4	+6	3	+6[w]	3	-	-	+8[h]	10	-	-	-	-	SO^{va}	+59	8	-	-	0.5	1612^{wa}	+59	(+50,+74)[aa]	
(W51)	+57	7	-	-	+58[xa]	-	+51[h]	12	+57[j]	15	+57[j]	15	H_2S^{va}	+57	7	+59[k]	8[h]	8	1665^{wa}	(+56,+62)	-	$C92\alpha^{za}$: +56 km s^{-1}
	+66	4	+66[qa]	6	+67[xa]	7	+65[h]	12	+67[j]	9	-	-	NH_3^z	+56	19	-	-	6.5	1720^{wa}	(+54,+65)	-	
	+69	-	-	-	-	-	-	-	+69[fa]	4	-	-	CN[ab]	+57	-	-	-	-	-	-	-	
													CS[ga]	+58	10							
													C_2H^u	+57	10							
													HCN[ma]	+53	15							
													H_2CO^{bb}	+53	11							
													H_2CS^{ob}	+52	8							
													HNCO[yd]	+63	10							
													$HCCCN^{db}$	-	-							
													$U89.2^{eb}$	+61	12							
													$U90.7^{fb}$	+60	10							
													$U93.2^{na}$	+57	-							
G69.5-1.0	+11	3	-	-	-	-	-	-	+14[gb]	8	-	-	CS[hb]	+11	4	-	-	1,5	1665^{ib}	(+12,+17)	(+5,+26)[aa,jb]	
(ON1)													$U93.2^{na}$	+11	5				1667^{ib}	+14		
																			4765^{sd}	+9		
																			6035^{td}	-		
G70.3+1.6	-22	3	-	-	-21[x]	4	-23[kb]	12	-23[j]	8	-26,-22[j]	8,8	HCN[lb]	-20	-	-24[m]	9[m]	9	1665^{ib}	(-24,-19)	(-27,-22)[n]	$C94\alpha^{zd}$: -22 km s^{-1}
(ON3,K3-50)													$U89.2^{lb}$	-22	12				1667^{ib}	-21		
																			1720^{ib}	-13		
G75.8+0.3	-3	4	-	-	-	-	-	-	-	-	-	-	-	-	-	-5[m]	5.5[m]	5.5	1665^{ib}	(-6,+3)	(-20,+14)[aa]	
(ON2)	+4	5	-	-	-	-	-	-	-	-	-	-	-	-	-	-	-	4	1667^{ib}	(-6,+3)	-	

TABLE 2—*Continued*

Source	CH[a]		OH Abs.[b]		H_2CO Abs.[c]		HI Abs.		^{12}CO		^{13}CO		Other Molecules			H109α	D_S	D_{CL}	OH Emission[d]		H_2O Emission[e]	Remarks
	V_{LSR}	ΔV	V_{LSR}	ΔV	V_{LSR}	ΔV	V_{LSR}	ΔV	V_{LSR}	ΔV	V_{LSR}	ΔV	Species	V_{LSR}	ΔV	V_{LSR}	kpc	kpc	Line	V_{LSR}	V_{LSR}	
G78.5+1.2	−3	5	−2[mb]	5	–	–	–	–	Yes[nb]		–	–	–	–	–	−7[m]	5[m]	4	–	–	–	
(DR5)	+1	2	+1[mb]	3	–	–	–	–	–	–	–	–	–	–	–	–	–	<1,4	–	–	–	
G79.2+0.3	−3	–	–	–	–	–	–	–	Yes[nb]		–	–	–	–	–	−2[m]	4[m]	4	–	–	–	
(DR15)	+1	3	+1[mb]	6	–	–	–	–	–	–	–	–	–	–	–	–	–	<1,3	–	–	–	
	+9	3	–	–	–	–	–	–	–	–	–	–	–	–	–	–	–	–	–	–	–	
G80.9−0.2	−2	3	−2[mb]	7	–	–	(−8,+14)[s,ob]	–	−11,−1[j]	6,9	–	–	–	–	–	−1[m]	3[m]	3	–	–	–	
(DR22)	+6	4	+5[mb]	5	+7[g]	2	–	–	–	–	–	–	–	–	–	–	–	<1.5[mb]	–	–	–	
G81.7+0.5	−3	3	−2[mb]	9	−3[g]	4	(−4,−2)[s,ob]		−3[nb]	8	−3[j]	7	SO[va]	−4	4	+2[m]	3[mb]	3	1665[pb]	(−2,+6)	(−12,+6)[aa]	
(DR21)	+8	3	+9[mb]	7	+9[g]	3	(+8,+14)[s,ob]		+8[nb]	4	–	–	H_2S[ya]	−3	9	–	–	<1.5[mb]	–	–	–	
													NH_3[qb]	−3	3							
													CS[hb]	−2	3							
													C_2H[u]	−2	3							
													HCN[hb]	−3	5							
													H_2CO[rb]	–	–							
													CH_3OH[rb]	–	–							
													U90.7[fb]	–	–							
													U93.2[na]	−2	6							
G84.7−1.0	+1	6	+1[sb]	2	–	–	–	–	+2[tb]	10	–	–	NH_3[ub]	+1	2	+1[vb]	1[wb]	1	1612[sb]	+4	–	
(NGC7000)			+4[sb]	1	–	–	–	–	–	–	–	–	–	–	–	–	–	–	1720[sb]	0	–	
G84.9−1.0	+3	5	–	–	+1[xb]	3	–	–	–	–	–	–	–	–	–	+1[vb]	1[wb]	1	–	–	–	
(NGC7000)					+5[xb]	<1	–	–	–	–	–	–	–	–	–	–	–	–	–	–	–	
G111.5+0.8	−56	3	–	–	−56[yb]	6	–	–	−57[j]	10	−57[j]	9	H_2S[ya]	−57	4	−61[m]	4[zb]	4	1665[w]	(−61,−53)	(−115,−109)[aa]	6 cm H_2CO emission
(NGC7538)	−52	4	–	–	−53[yb]	2	–	–	–	–	–	–	CS[ga]	−57	6	–	–	4	1667[w]	−59	(−62,−52)[aa]	at −60 and −58 km s^{-1} [ac]
													C_2H[u]	−57	6				1720[w]	(−61,−57)		
													HCN[hb]	−58	4				6035[ud]	–		
													U89.2[ga]	–	–							
													U90.7[ga]	–	–							

TABLE 2—*Continued*

Source	CH[a]		OH Abs.[b]		H_2CO Abs.[c]		HI Abs.		^{12}CO		^{13}CO		Other Molecules			H109α	D_S	D_{CL}	OH Emission[d]		H_2O Emission[e]	Remarks
	V_{LSR}	ΔV	V_{LSR}	ΔV	V_{LSR}	ΔV	V_{LSR}	ΔV	V_{LSR}	ΔV	V_{LSR}	ΔV	Species	V_{LSR}	ΔV	V_{LSR}	kpc	kpc	Line	V_{LSR}	V_{LSR}	
G111.7-2.1	-47	4	-47[q]	4	-47[bc]	4	-48[bc]	8	-	-	-	-	-	-	-	-	3.4[cc]	4	-	-	-	
(Cas A)	-40	3	-41[q]	4	-40[bc]	4	-38[bc]	9	-42[j]	9	-	-	-	-	-	-	-	{3	-	-	-	
	-37	3	-37[q]	3	-37[bc]	3			-	-	-	-	-	-	-	-	-	3	-	-	-	
	-1.4	0.9	-1.4[q]	0.8	-1.5[x]	0.8	-1.5[md]	2	-1[j]	15	-	-	-	-	-	-	-	<0.2	1720[dc]	-1	-	
	-0.1	0.9	0.0[q]	0.9	-0.2[x]	1.0	-0.4[md]	3	-	-	-	-	-	-	-	-	-	<0.1	-	-	-	
G118.1+5.0	-13	3	-14[ec]	4	-	-	-	-	-12[j]	15	-	-	-	-	-	-	-	1	-	-	-	Optical CH and CN lines[gc]: -12 to -8 km s^{-1}. $H134\alpha$[hc]: -19 km s^{-1}
(W1)	-7	3	-7[ec]	3	-	-	-	-	-	-	-	-	-	-	-	-8[fc]	1[ec]	< 1	-	-	-	
G133.7+1.2	-40	4	-39[za]	5	-40[g]	4	-40[ic]	8	-41[j]	9	-41[j]	7	H_2S[ya]	-39	9	-42[m]	3[m]	3	1612[lc]	(-39,-32)	(-48,-32)[aa]	Cα lines[kc]: -41 km s^{-1}.
(W3 C1)			-40X[lc]	4	-	-	-	-	-	-	-	-	CS[ga]	-42	6	-	-	-	1665[lc]	-40	-	X denotes excited state OH absorption
													C_2H[u]	-40	7				1667[jc]	-54,-23	
													HCN[hb]	-43	7				1720[lc]	-41	
													U89.2[lb]	-39	6				4765[lc]	-34	
G133.9+1.1	-48	3	-	-	-46[g]	5	-	-	-47[j]	8	-46[j]	6	H_2S[ya]	-48	8	-	-	4	1612[mc]	-42	(-56,-46)[aa]	
(W3 OH)													NH_3[z]	-48	2				1665[mc]	(-50,-41)	
													CS[ga]	-46	7				1667[mc]	(-46,-42)	
													C_2H[u]	-48	5				1720[mc]	(-46,-43)	
													HCN[ma]	-49	14				4765[vd]	(-46,-43)	
													H_2CO[bb]	-48	7				6030[wd]	(-49,-42)	
													U89.2[lb]	-47	8				6035[wd]	(-49,-42)	
													U90.7[ld]	-	-				13441[xd]	-44	
G134.0+0.8	-49	4	-50[nc]	3	-49[nc]	3	-49[nc]	-	-	-	-	-	-	-	-	-	-	4	-	-	-	HI self-absorption feature[nc]
(W3)																						
G205.3-14.3	+6	4	-	-	-	-	-	-	-	-	-	-	-	-	-	-	-	0.5	-	-	-	
(NGC2068)	+11	2	-	-	+11[oc]	2	-	-	+11[pc]	3	+10[pc]	2	-	-	-	-	-	1	1667[qc]	+10	-	Cα lines[nd]: +11 km s^{-1}
G206.6-16.4	+6	-	-	-	-	-	-	-	-	-	-	-	SO[va]	+10	2	+7[m]	0.5[h]	0.5	-	-	+9[rc],+11[p],+18[p]	Cα lines[ka]: +10 km s^{-1}
(W12)	+10	3	+10[rc]	1.5	+9[rc]	1.5	+10[h]	8	+11[j]	8	+10[j]	6	CS[hb]	+11	3	-	-	{1	-	-	-	
	+13	-	+13[rc]	1	+13[rc]	-	+13[sc]	-	-	-	-	-	C_2H[u]	+10	3	-	-	1	-	-	-	
													HCN[hb]	+11	2							
													U89.2[lb]	+15	8							
													U90.7[ld]	-	-							

TABLE 2—*Continued*

Source	CH[a]		OH Abs.[b]		H_2CO Abs.[c]		HI Abs.		^{12}CO		^{13}CO		Other Molecules			$H109\alpha$	D_S	D_{CL}	OH Emission[d]		H_2O Emission[e]	Remarks
	V_{LSR}	ΔV	V_{LSR}	ΔV	V_{LSR}	ΔV	V_{LSR}	ΔV	V_{LSR}	ΔV	V_{LSR}	ΔV	Species	V_{LSR}	ΔV	V_{LSR}	kpc	kpc	Line	V_{LSR}	V_{LSR}	
G208.8−19.3	+8	3	–	–	–	–	–	–	–	–	–	–	NH_3[uc]	+11	1	–	–	0.5	–	–	–	CH position 4′NW
(Ori A)	+11	4	–	–	+10[vc]	–	–	–	+11[wc]	3	–	–	CS[wc]	–	–	–	–	1	–	–	–	OMC-2[wc]
													HCN[uc]	+11	2							
													U89.2[uc]	+11	2							
													U90.7[uc]	+11	2							
G208.9−19.6	+6	–	–	–	–	–	–	–	–	–	–	–	–	–	–	–	–	0.5	–	–	–	
(Ori A)	+9	3	–	–	–	–	–	–	+9[xc]	3	+9[xc]	–	–	–	–	–	–	1	–	–	–	
	+12	–	–	–	–	–	–	–	–	–	–	–	–	–	–	–	–	1	–	–	–	
G209.0−19.4	+6	–	+6[za]	2	+6[yc]	2	+5[h]	8	–	–	–	–	SiO[zc]	+8	15	−3[m]	0.5[ad]	0.5	1612[q]	(+6,+24)	(−8,+26)[ia]	Vibrationally
(Ori A)	+9	6	–	–	–	–	–	–	+9[j]	7	+9[j]	6	SO[bd]	+9	25	–	–	1	1665[q]	(−10,+26)	–	excited SiO maser
													H_2S[ya]	+9	9							emission[ad,dd]: −7
													NH_2[z]	+8	3							and +16 km s^{-1}.
													CN[fd]	+9	4							CO lines[ka,ed]:
													CS[ga]	+9	5							+8 km s^{-1}. HDO[od]
													C_2H[u]	+9	4							at +6 km s^{-1}
													HCN[gd]	+9	4							width 9 km s^{-1}
													H_2CO[hd]	+9	5							
													HCCCN[db]	–	–							
													CH_3OH[id]	+8	1							
													$(CH_3)_2O$[jd]	+9	–							
													CH_3NH_2[kd]	–	–							
													U72.4[qd]	+9	–							
													U89.2[lb]	+10	4							
													U90.1[od]	–	–							
													U90.7[ld]	–	–							
													U93.2[na]	+9	5							
G209.1−19.7	+9	4	–	–	+8[vc]	3	–	–	–	–	–	–	–	–	–	–	–	–	–	–	–	
(Ori A)																						

NOTES TO TABLE 2

(a) Average of the CH lines.
(b) 1667 MHz line if not otherwise noted. Velocities based on rest frequencies of ter Meulen and Dymanus 1972.
(c) 4830 MHz line. Velocities based on rest frequency of Tucker *et al.* 1971.
(d) Line frequency in MHz. Velocities in parentheses give limits within which emission peaks occur.
(e) Velocities in parentheses give limits within which emission peaks occur.
(f) Robinson *et al.* 1970.
(g) Wilson 1972.
(h) Radhakrishnan *et al.* 1972*b*. Velocities and widths estimated from spectra.
(i) Pastchenko and Slysh 1974.
(j) Wilson *et al.* 1974.
(k) Wilson *et al.* 1970*b*.
(l) Wilson 1974.
(m) Reifenstein *et al.* 1970.
(n) Yngvesson *et al.* 1975.
(o) Lada *et al.* 1974*a*.
(p) Johnston *et al.* 1973.
(q) Goss 1968.
(r) Lada and Chaisson 1975.
(s) Denotes interval of absorption.
(t) Menon 1970.
(u) Tucker *et al.* 1974.
(v) This paper (Fig. 19).
(w) Unpublished Onsala data.
(x) Zuckerman *et al.* 1970.
(y) Turner 1969*a*.
(z) Morris *et al.* 1973*b*.
(aa) Cato *et al.* 1975.
(ba) Broad, weak emission feature.
(ca) 1612 MHz data. 1667 MHz absorption is blended with maser emission.
(da) Dominant peak at $+60$ km s^{-1}.
(ea) Pastchenko and Slysh 1973. $+17$ km s^{-1} feature observed at 1720 MHz.
(fa) Estimated from Scoville and Solomon 1973.
(ga) Turner *et al.* 1973.
(ha) Weaver *et al.* 1968.
(ia) Sullivan 1973.
(ja) Dominant peaks in the interval -10 to $+20$ km s^{-1}.
(ka) Chaisson and Ball 1971.
(la) Uncertain because of closeness to maser emission.
(ma) Snyder and Buhl 1971.
(na) Turner 1974.
(oa) Pankonin *et al.* 1973.
(pa) Goss *et al.* 1973.
(qa) Slysh 1973.
(ra) Parrish *et al.* 1972. Beam centered about 7′.5 south of our position.
(sa) Estimated from Sato 1973, and Sato and Akabane 1974.
(ta) Whiteoak and Gardner 1970.
(ua) Wilson *et al.* 1970*a*.
(va) Gottlieb and Ball 1973.
(wa) Elldér *et al.* 1973.
(xa) This paper (Fig. 30).
(ya) Thaddeus *et al.* 1972.
(za) Chaisson 1974.
(ab) Jefferts *et al.* 1970.
(bb) Thaddeus *et al.* 1971.
(cb) Cato *et al.* 1972.
(db) Morris *et al.* 1973*a*.
(eb) Buhl and Snyder 1970.
(fb) Snyder and Buhl 1972*c*.
(gb) Schwartz *et al.* 1973 about 30′ off the CH position. Ref. nb reports detection toward ON1.
(hb) Morris *et al.* 1974*a*.
(ib) Winnberg 1970.
(jb) Dominant peak at $+10$ km s^{-1}.
(kb) Thompson *et al.* 1969.
(lb) Buhl and Snyder 1973.
(mb) Pashchenko 1974.
(nb) Dickel *et al.* 1974, and private communication.
(ob) Sato 1968.
(pb) Rydbeck *et al.* 1969.
(qb) Mayer *et al.* 1973.
(rb) Kutner *et al.* 1973.
(sb) Turner 1973.
(tb) Penzias *et al.* 1972.
(ub) Cheung *et al.* 1973.
(vb) Pedlar and Matthews 1973.
(wb) Hippelein 1973.
(xb) Minn and Greenberg 1973*a*.
(yb) Minn and Greenberg 1975.
(zb) Habing *et al.* 1972.
(ac) Downes and Wilson 1974*a*.
(bc) Estimated from Davies 1973.
(cc) Minkowski 1968.
(dc) Turner 1969*a*.
(ec) Winnberg and Lundahl 1970.
(fc) Dickel and Milne 1972.
(gc) Münch 1964.
(hc) Downes and Wilson 1974*b*.
(ic) Minn and Greenberg 1973*b*.
(jc) Turner 1970.
(kc) Zuckerman and Ball 1974; Chaisson 1974; Pedlar and Hart 1974.
(lc) Rydbeck *et al.* 1973*b*. Excited state absorption in W3C1 in the 6030 and 6035 MHz lines.
(mc) Rydbeck *et al.* 1972.
(nc) Höglund and Andersson 1974.
(oc) Dieter 1973.
(pc) Tucker *et al.* 1973.
(qc) Goss *et al.* 1975. Broad ($\Delta V \approx 4$ km s^{-1}) dust cloud emission.
(rc) This paper (Fig. 13).
(sc) Greisen 1973*b*.
(tc) Kinematic distance greater than source distance.
(uc) Morris *et al.* 1974*b*.
(vc) Kutner and Thaddeus 1971.
(wc) Gatley *et al.* 1974.
(xc) Linke and Wannier 1974.
(yc) Zuckerman and Ball 1974.
(zc) Dickinson 1972.
(ad) Zuckerman 1973.
(bd) Clark and Johnson 1974.
(cd) Thaddeus *et al.* 1974.
(dd) Buhl *et al.* 1974.
(ed) Balick *et al.* 1974.
(fd) Penzias *et al.* 1974.
(gd) Snyder and Buhl 1973.
(hd) Ref. bb, Kutner *et al.* 1971; Harvey *et al.* 1974.
(id) Chui *et al.* 1974.
(jd) Snyder *et al.* 1974.
(kd) Fourikis *et al.* 1974; Kaifu *et al.* 1974.
(ld) Snyder and Buhl 1972*b*.
(md) Clark 1965.
(nd) Brown *et al.* 1975.
(od) Turner *et al.* 1974*b*.
(pd) Gull and Balick 1974.
(qd) Wilson *et al.* 1973.
(rd) Turner *et al.* 1974*a*.
(sd) Baudry 1974.
(td) Rickard *et al.* 1973.
(ud) Rickard *et al.* 1972.
(vd) Rydbeck *et al.* 1970; Rydbeck *et al.* 1972.
(wd) Ref. vd, Zuckerman *et al.* 1972.
(xd) Turner *et al.* 1970*b*.
(yd) Snyder and Buhl 1972*a*.
(zd) Chaisson and Goad 1972.

TABLE 3

CH SATELLITE LINE EXCITATION DATA AND FAR-INFRARED LUMINOSITIES OF ASSOCIATED SOURCES

Source	Adopted Distance (kpc)	Line Ratios		Relative Population Difference Ratios		$L_{100\mu}$[a]	$L_{350\mu}$[b]	$L_{114-196\mu}$[c]	$L_{30-300\mu}$[d]	$L_{40-350\mu}$[e]	$L_{45-750\mu}$[f]	L^{g}	Fig.No.
		Q_{um}	Q_{lm}	I_u/I_m	I_l/I_m	10^{19} W Hz^{-1}	10^{17} W Hz^{-1}	10^{31} W Hz^{-1}	10^{31} W	10^{31} W	10^{31} W	10^{31} W	
G15.0-0.7 (M17)	2.5	-	-	-	15.0[h]	17	4[i]	21	71	-	55	81	14
G29.9-0.0 (W43)	7,10	0.7	1.4	1.9	7.5	22,44	-	-	-	-	-	-	21
G30.7-0.0 (W43)	7	0.8[j] 0.8[k]	1.8[j] 4.2[k]	1.9[j] 2.1[k]	5.0[j] 15.0[k]	40	-	73	-	-	-	-	20
G34.3+0.1 (W44)	4,13	0.5	1.4	1.0	7.5	-	-	18,192	-	-	-	-	22
G43.2-0.0 (W49)	14	-	8.0	-	30.0	178	520	-	-	-	726	302	23
G49.2-0.3 (W51)	6.5	0.6	2.0	1.5	7.5	12	-	-	-	-	-	-	27
G49.4-0.2 (W51)	8	0.5	1.5	1.0	7.5	-	-	-	-	-	92	-	28
G49.5-0.4 (W51)	8	- 1.0[m]	- 4.6[m]	- 2.5[m]	15.0[l] 15.0[m]	100	207	-	-	-	490	230	29
G70.3+1.6 (ON3,K3-50)	9	-	-	-	15.0[n]	15	-	-	-	-	48	81	32
G81.7+0.5 (DR 21)	3	0.6	1.5	1.7	7.5	4	25	-	-	-	9	15	39
G133.7+1.2 (W3 C1)	3	1.2	2.8	3.8	15.0	-	-	-	45	39	-	29	45
G206.6-16.4 (W12)	0.5	0.6	1.5	1.5	5.0	-	-	-	1	1	1	1	12
G209.0-19.4 (Ori A)	0.5	0.6	1.0	1.9	7.5	1	-	-	7	4	6	10	49

NOTES TO TABLE 3

(a) Calculated from Hoffman *et al.* 1971 from total 100 μ flux density.
(b) Calculated from Rieke *et al.* 1973.
(c) Calculated from Olthof 1974.
(d) Calculated from Harper 1974.
(e) Calculated from Emerson *et al.* 1973.
(f) Calculated from Harper and Low 1971.
(g) Calculated from Pottasch 1974.
(h) Assumed value ($+20$ km s^{-1} feature). Lower satellite completely dominant.
(i) May be an order of magnitude too small (Rieke *et al.* 1973).
(j) $+82$ km s^{-1} feature.
(k) $+94$ km s^{-1} feature.
(l) Assumed value ($+57$ km s^{-1} feature). Lower satellite completely dominant.
(m) $+66$ km s^{-1} feature.
(n) Assumed value. Lower satellite completely dominant.

by OH maser emission) and the strongly enhanced lower satellite CH emission features (i.e., if $|T_x| \ll T_{CR}$ for all three species). This similarity occurs since the dominant contributions to these lines emanate from the very same part of the cloud, the solid angle cut out of the cloud by the continuum source observed. Thus, as long as the cloud and antenna solid angles are much greater than the continuum source solid angle, the similarity in line shape is almost independent of the observing antenna. This conclusion holds even if the strong continuum source consists of several compact components, which still cut out the same parts of the molecular cloud when observed with different antennas for OH, H_2CO, and CH. For such a case we only have to modify relation (13) by summing over the compact sources and the diffuse background in which they may be embedded, which results in

$$T_A(v) = RF(T_x - T_B)\tau(v) - \sum_i R_i T_{CR,i}\tau_i(v)\,. \tag{15}$$

Obviously, aperture-synthesis high-resolution observations of the stronger H II regions are important for deciding how the various background components contribute to T_A (often one or two of the compact sources are an order of magnitude brighter than the others). This has already been pointed out in our source descriptions.

We have detected CH absorption features (in the main and upper satellite lines; $T_x > 0$) only toward the *strongest* ($T_{CR} \approx 37$ K) of our observed H II regions, M17, which is more than 3 times stronger than any of the other observed H II regions, except Ori A (where the cloud is believed to lie behind the H II region). Toward W49A, W51, and ON 3 (K3–50), no absorption features in the upper satellite and main lines are found in the velocity interval of the strongly enhanced lower satellite. The continuum background probably is too small to produce observable absorption features, even if $T_x > 0$ (i.e., assuming the same CH pumping conditions as those in the M17 cloud). In the southern hemisphere, CH absorption features have been observed only for a few *high-flux-density* sources (Robinson *et al.* 1974; Gardner and Robinson 1974). It is evident from relation (13) or (15) that absorptions are more easily detected by a larger antenna yielding a higher observed T_{CR}.

The weak maser behavior of CH is clearly demonstrated by the observations toward and around our strongest discrete continuum source, Cas A (for which $T_{CR} \approx 85$ K). Off-source the Orion and Perseus spiral-arm clouds are detectable only after very long integration times. On-source the spectra are among the strongest that we have observed.

Our mappings of the W3, W12, W43, and W51 regions demonstrate the expected strong intensity increase with T_{CR} of the anomalously excited lower satellite CH transition. The anomalous excitation is probably caused by far-infrared radiation, which will be discussed in § VII.

Toward the strongest discrete continuum source, Cas A, we expect by equation (13) or (15) a very good agreement in shape between OH and H_2CO absorption features and all three emission lines of CH. The observed profiles confirm this expectation to a remarkable degree. For several other sources we find a very good agreement in shape between OH and H_2CO absorption lines and lower satellite CH emission profiles, as expected. This strongly suggests that OH, H_2CO, and CH are well mixed.

Toward M17 the agreement in shape is also good between the anomalously enhanced lower satellite CH emission and the molecular-cloud millimeter lines of CO, H_2CO, SO, and HCN. This clearly indicates that the dominant contribution to the observed CH profile also emanates from the molecular cloud in front of the strong continuum background source.

Such similarities (and differences) between ground-state CH, OH, and H_2CO spectra and millimeter lines from molecular cloud species, together with aperture-synthesis maps of the associated continuum sources, should be very useful for the evaluation of molecular cloud–far–infrared–radio source configurations. The fact that the CH lower satellite line seems to be a sensitive far-infrared indicator may be important in this context.

IV. OBSERVATIONS OF DARK DUST CLOUDS

The galactic dust clouds, such as those studied for optical extinction by Lynds (1962) and first examined for OH radio emission by Heiles (1968), are cold regions of high gas and dust density, the majority of known clouds being located within a few hundred parsecs from the Sun. On the basis of CO observations, Penzias *et al.* (1972) estimate typical hydrogen densities $> 10^3$ cm^{-3}, and kinetic temperatures, $T_{kin} \lesssim 10$ K. Such conditions would seem to be very conducive to molecule formation and preservation, and observations have revealed that most such clouds contain OH (e.g., Crutcher 1973) and H_2CO (Minn and Greenberg 1973*a*; Dieter 1973), while a significant fraction probably contains CO also (Penzias *et al.* 1972) and NH_3 (Cheung *et al.* 1973). Hydrogen is presumed to

TABLE 4

OBSERVATIONS OF DUST CLOUDS[a]

Cloud	Position (1950)		Antenna Temp. K			CH[b]		OH[c]		H_2CO[d]		Other Species		
	RA	DE	F=1-0	F=1-1	F=0-1	Velocity km s^{-1}	Width	Velocity km s^{-1}	Width	Velocity km s^{-1}	Width	Species	Velocity	Width
G4.2+35.8 (L134)	$15^h50^m54^s$	$-4°31'$	0.08	0.14	0.08	+2.6	0.8	+2.5[e]	0.9	+2.6[f]	0.6	CO^g	+2.9	2.0
												HI^t	+0.5	5
G6.0+36.7 (L134N)	15 51 28	-2 45	0.06	0.11	0.06	+2.5	0.8	+2.5[e]	0.7	+2.0[h]	1.3	NH_3^i	+2.5	1.0
G93.5+9.6 (L1036)	20 37 00	57 00	0.02	0.04	0.02	-2	3	-	-	-2.4[h]	1.4	-	-	-
G97.0+10.1 (L1082)	20 50 00	60 00	0.02	0.05	0.03	-2	2	(-6.8[j])	-	(-39.0[k]	0.5)	-	-	-
G114.2+14.8 (Heiles Cloud 1)	22 30 00	75 00	0.04	0.07	0.04	-4.3	1.1	-4.6[e]	1.2	-4.3[f]	1.6	CO^g	-4.5	3.0
G150.2+3.9 (L1399)	04 20 00	55 00	0.04	0.06	0.03	+3	1	(-4.8[j])	-	+3.1[h]	0.9	-	-	-
G158.3-20.5 (NGC1333)	03 25 55	31 11	-	0.05	-	+8	3	+7.6[l]	3	+7.9[m]	1.8	NH_3^m	+8	1.3
												CO^m	+8	3
												CS^m	+8.2	1.6
												HCN^m	+7.7	1.7
												H_2O^n	-25.4	1.6
												HI^l	+4.5	-
G159.3-20.2 (Per OB 2 dust cloud)	03 30 15	30 48	0.06	0.13	0.07	+6.5	2.0	+6.4[l]	2	-	-	HI^l	+5.5	-
G160.5-17.8 (IC 348)	03 41 26	32 03	-	0.06	-	+9	2	+8.2[l]	3	-	-	CO^p	+8	2
						+6o	-					HI^l	+7	-
						+8q	-							
G172.7-14.4 (Heiles Cloud 2)	04 30 30	26 12	0.10	0.19	0.10	+6.1	0.9	+6.5[e]	0.8	+6.2[r]	0.4	-	-	-
G174.3-13.4 (Heiles Cloud 2)	04 38 30	25 38	0.12	0.20	0.15	+5.7	1.3	+5.7[e]	1.4	+5.7[s]	1.0	CO^g	+5.2	3.1
												HI^u	+5.6	3.1

NOTES TO TABLE 4

(a) Listed velocities are relative to the local standard of rest. Widths are full widths at half-maximum intensity.
(b) The values are averages of the three lines. Parameters given with decimals are deduced from 1 kHz spectra; those without are from 10 kHz data, in which case widths are corrected for instrumental broadening.
(c) Velocities (main line) based on rest frequencies of ter Meulen and Dymanus 1972.
(d) Velocities based on rest frequencies of Tucker *et al.* 1971.
(e) From SUM spectra of Turner 1973.
(f) Sume *et al.* 1975.
(g) Penzias *et al.* 1972.
(h) Dieter 1973.
(i) Cheung *et al.* 1973.
(j) Cudaback and Heiles 1969.
(k) Minn and Greenberg 1973*a*.
(l) Sancisi *et al.* 1974. Widths corrected for instrumental broadening.
(m) Lada *et al.* 1974*b*.
(n) Dickinson *et al.* 1974.
(o) Cohen 1973 from optical data toward o Per.
(p) Milman 1974.
(q) Chaffee 1974 from optical data toward o Per.
(r) Heiles 1973.
(s) Heiles and Gordon 1974.
(t) Sancisi 1971.
(u) Knapp 1974.

be largely in the form of H_2, although direct evidence for this is not generally available (cf. Heiles and Gordon 1973; Sancisi 1971). Detailed observations of OH show that the main line intensities (1665 and 1667 MHz) are usually compatible with thermal emission with excitation temperature $T_{x,\mathrm{OH}} \approx T_{\mathrm{kin}}$, although some anomalies occur, while the satellites generally show anomalous excitation (Turner 1973). The OH and H_2CO features appear to have approximately the same velocity and widths, and hence seem to occur in the same parts of the clouds (Minn and Greenberg 1973*a*; Crutcher 1973; Dieter 1973).

We have detected CH in the clouds Heiles 1, Heiles 2, L134, L134N, L1036, L1082, L1399, the Perseus OB 2 dust cloud (including NGC 1333 and IC 348), and have also examined points immediately adjacent to L134. Dust clouds occurring in the direction of some of the observed H II regions are described in connection with these sources (e.g., Ori A, W12, Cyg X). We found all three CH transitions in emission in the observed clouds (with the exception of a few directions, in which the main line was too weak for meaningful observations of the satellite transitions). The observations are summarized in Table 4, which also lists radial velocities and widths of other species. (The recently reported 2 cm H_2CO observations by Evans *et al.* 1975 toward dust clouds fit in well with these data). The observed CH velocities mostly agree very well with the corresponding OH and H_2CO velocities. This suggests that these three molecular species are well mixed in the dark clouds. It must be borne in mind, however, that the observations at four of these locations have been used together with Cas A spectra in our determination of the CH transition frequencies (Rydbeck *et al.* 1974*c*).

The observed CH line intensities for most dust clouds approximately exhibit the 1:2:1 ratio characteristic of LTE and small optical depths. However, an important exception appeared (after long integrations) in our position G174.3−13.4 of Heiles's Cloud 2, where at least the lower satellite line is definitely enhanced above the LTE value. This is discussed at some length in § VI. Apart from this case the assumption of LTE is not contradicted by the observed line ratios. Although we have not performed detailed excitation calculations, it seems possible on the basis of the relatively high density and the apparent near-equality $T_{x,\mathrm{OH}}$ (main lines) $\approx T_{x,\mathrm{CO}} \approx T_{\mathrm{kin}}$ (cf. Penzias *et al.* 1972; Turner 1973) to consider therefore the case $T_{x,\mathrm{CH}} \approx T_{\mathrm{kin}}$.

The CH opacities and total column densities of the observed clouds, presented in Table 5, have been determined by means of relations (6) and (7) of the Cas A paragraph (with $T_{\mathrm{CR},1} = 0$). The value of T_B has been taken as the sum of the cosmic background ($\approx$2.7 K) and the nonthermal galactic continuum ($\approx$0.1 K). The latter value was obtained from the 404 MHz data of Seeger *et al.* (1965) by using a spectral index of 2.9 (Heiles 1969; Turner 1973). The optical depths, listed in column (4), were obtained with $T_{x,\mathrm{CH}} = T_{\mathrm{kin}}$, where T_{kin}, given in column (2), was chosen as a mean of the kinetic temperatures determined from OH and CO observations (Heiles 1968; Penzias *et al.* 1972; Turner 1973; Sancisi *et al.* 1974). When no published value was available, 6 K was used for $T_{x,\mathrm{CH}}$. We list in column (5) two values of the column densities in each cloud. One value was calculated with $T_{x,\mathrm{CH}} = T_{\mathrm{kin}}$ (assuming LTE) and the other with $T_{x,\mathrm{CH}} = -15$ K, i.e., assuming that CH is a weak maser, as for H I clouds and clouds associated with H II regions.

To estimate the range of possible values of the CH column densities due to the uncertainty of the excitation temperature, we note by relation (7) that the rather extreme values $T_{x,\mathrm{CH}} = +4$ K and -1 K result in a column density increase and decrease by a factor 4 from the nominal value obtained with $|T_{x,\mathrm{CH}}| \gg T_B$. Uncertainties due to beam dilution and clumping, as discussed below, increase this range (cf. also discussion in § III*b*).

Recent observations toward and around the extragalactic source 3C 123, which lies behind Lynds's cloud L1500, seem to indicate a CH weak maser behavior also in a dark dust cloud. These observations are briefly discussed in § VI, and will be treated in a separate paper on further observations of dust clouds. It should be noted in this context that the approximate 1:2:1, LTE–type line ratios observed toward many dust clouds do not contradict the possible weak maser behavior. By relation (3) in the Cas A paragraph, we find that the lines will be observed in the approximate LTE ratio irrespective of the sign of the excitation temperatures, when the influence of the weak background radiation is small compared to the cloud emission.

Following Heiles (1968) and Turner (1973), we have estimated the beam dilution factor ($=\rho_{10}$) from the Palomar Sky Survey Prints (PSS), under the assumption that the CH emission is uniform over the contour of the optically obscured area. Our mapping of L134 (cf. Fig. 27) indicates that this is a fairly reasonable assumption. We have, of course, neglected possible clumping of CH, which may be concentrated in a number of small regions within

TABLE 5

DUST CLOUD COLUMN DENSITIES

Cloud	Adopted Kinetic Temp. K	Beam Dilution Factor	$T_{x,CH}=T_{kin}$	N_{CH} 10^{14} cm^{-2} Radio Data $T_{x,CH}=T_{kin}$	Radio Data $T_{x,CH}=-15$ K	Optical Data	N_{OH} 10^{15} cm^{-2}	N_{H_2CO}[a] 10^{13} cm^{-2}	N_{HI} 10^{20} cm^{-2}
(1)	(2)	(3)	(4)	(5)			(6)	(7)	(8)
G4.2+35.8 (L134)	5.4	0.6	0.09	1	0.4	-	1[b]	0.4[c] 0.7[d] 5[e]	70[f]
G6.0+36.7 (L134N)	6	0.4	0.09	1	0.7	-	0.5[b]	0.3[c] 8[e]	-
G93.5+9.6 (L1036)	6	0.6	0.02	1	0.5	-	-	0.9[c]	-
G97.0+10.1 (L1082)	6	0.2	0.08	3	1	-	-	-	-
G114.2+14.8 (Heiles Cloud 1)	4.4	0.25	0.18	2	0.6	-	1[b]	8[c] 8[d] 7[e]	-
G150.2+3.9 (L1399)	6	0.4	0.05	1	0.7	-	-	2[c]	-
G158.3-20.5 (NGC1333)	10	0.4	0.02	1	0.8	-	0.2[g]	-	13[g]
G159.3-20.2 (Per OB 2 dust cloud)	10	0.5	0.04	2	1	-	0.2[g]	-	12[g]
G160.5-17.8 (IC348)	10	0.3	0.03	2	1	0.2[h] 0.3[i]	0.2[g]	-	12[g] 10[j]
G172.7-14.4 (Heiles Cloud 2)	6	0.45	0.13	2	0.9	-	1[b]	7[e]	-
G174.3-13.4 (Heiles Cloud 2)	5.5	0.5	0.15	3	1	-	2[b]	5[c] 7[d] 6[e]	5[k]

NOTES TO TABLE 5

(a) N_{H_2CO} is the population in the 0_{00}, 1_{11}, and 1_{10} levels.
(b) Turner 1973.
(c) Dieter 1973 with $T_x = 1$ K.
(d) Sume *et al.* 1975.
(e) Heiles and Gordon 1974. Their values have been multiplied by 1.3 to account for population in the 0_{00} level
(f) Sancisi 1971.
(g) Sancisi *et al.* 1974; probably underestimated.
(h) Cohen 1973 from optical data toward o Per.
(i) Chaffee 1974 from optical data toward o Per.
(j) Jenkins and Savage 1974 from Lyman α absorption toward o Per.
(k) Knapp 1974.

the antenna beam. Clumping is, for example, suggested by observations of H_2CO, CS, and NH_3 at higher resolution (Cheung *et al.* 1973; Turner *et al.* 1973). If CH clumping occurs, which is likely, our column densities may be underestimated. We again point out that CH may combine to form heavier molecules in the denser regions of a cloud.

For comparison, Table 5 also lists OH, H_2CO, and H I column densities. Penzias *et al.* (1972) estimate typical CO column densities of 10^{18} cm^{-2}. A discussion of the abundance ratios appears in § VIII.

a) G4.2+35.8 (L134); G6.0+36.7 (L134N)

Although these small clouds are separated by about 2°, they appear to be part of the same complex. A summary of parameters for L134 has been presented by Sancisi (1971), who finds a deficiency of H I at the position of the cloud. OH appears to be concentrated toward the southern part of L134 (Heiles 1970). Turner (1973) finds only one velocity component toward both clouds, which is compatible with our CH spectra, shown in Figures 25 and 26. Observers have found H_2CO, NH_3 (at L134N), and CO (Penzias *et al.* 1972; Dieter 1973; Heiles 1973; Cheung *et al.* 1973). The velocities and widths of these species are given in Table 4.

Within the errors of observation, the CH line intensity ratios toward L134 correspond to LTE (see Table 4). Figure 25 depicts a 1 kHz spectrum smoothed to 3 kHz of the main line. The half-power line width is about 0.8 km s^{-1}, which corresponds to a Doppler temperature of ≈180 K. This should be compared with the most narrow width observed by us, 0.3 km s^{-1} (≈30 K), in the direction of M17. In the latter case, the background source is seen through a very small part of the cloud so that the lower line width value may be more closely related to the actual kinetic temperature (it may be an upper limit to the same).

Figure 26 shows 1 kHz spectra (also smoothed to 3 kHz) for all transitions, observed toward L134N. For L134N the OH line width is 0.7 km s^{-1} (Turner 1973), which corresponds to about the same Doppler temperature as the line width (0.8 km s^{-1}) of the somewhat lighter CH molecule.

Since the CH transitions are seen in the approximate LTE ratio toward L134 and L134N, it should be mentioned that the ground state OH satellite lines show an anomalous behavior (Turner 1973). In the case of L134, the 1720 MHz emission equals about one-third of the 1667 MHz intensity, whereas no 1612 MHz emission is seen. These anomalies are more pronounced in the direction of L134 than in L134N, and are believed to be caused by infrared pumping.

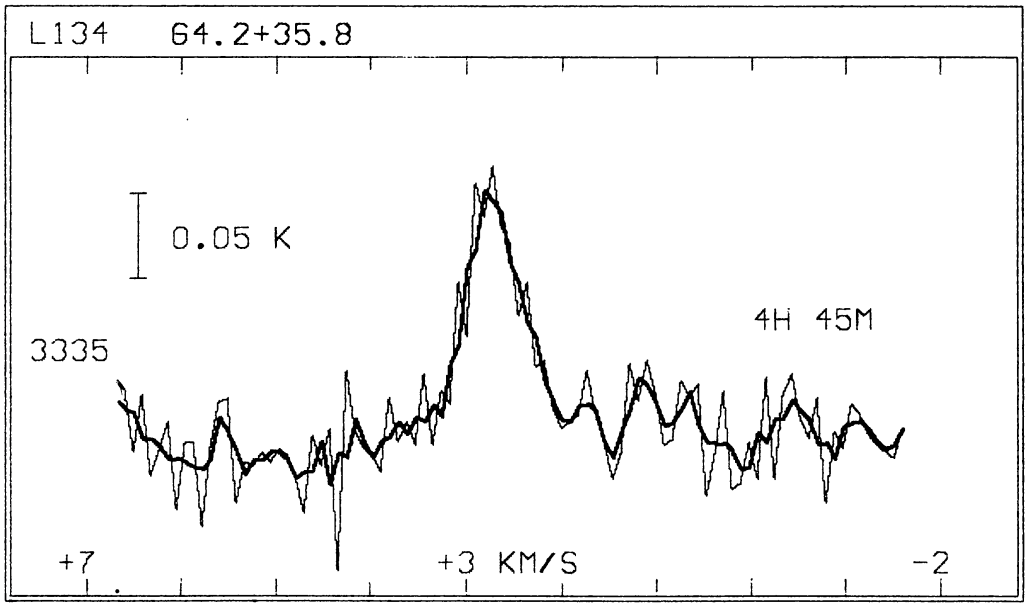

FIG. 25.—Main line CH spectrum toward L134. Heavy line is a three-point running mean of the 1 kHz spectrum (*light line*).

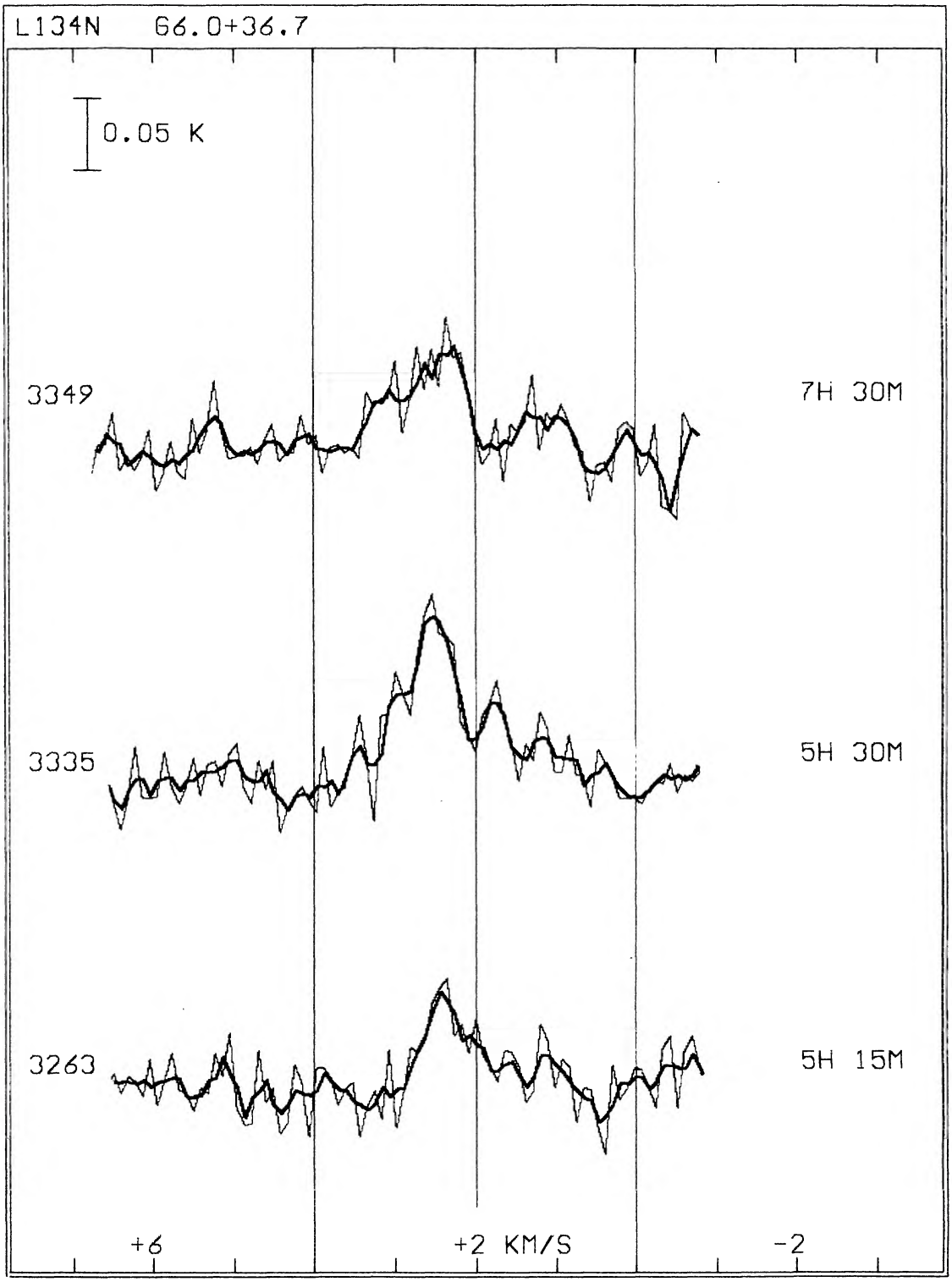

FIG. 26.—CH spectra toward L134N. Heavy lines are three-point running means of 1 kHz spectra (*light lines*).

In an effort to obtain a preliminary idea of the extent of the CH emission, relative to the distribution of dust and other molecules, we have observed all three CH transitions in four directions around the center of L134, as shown in Figure 27. The approximate visual cloud contour, obtained from PSS (Heiles 1970), has been entered in the figure. Our observations indicate that there is a fairly good resemblance between the optical cloud boundaries (which are not too well defined) and the CH emission. The latter appear to have some concentration toward the south, as is also observed for OH (Heiles 1970).

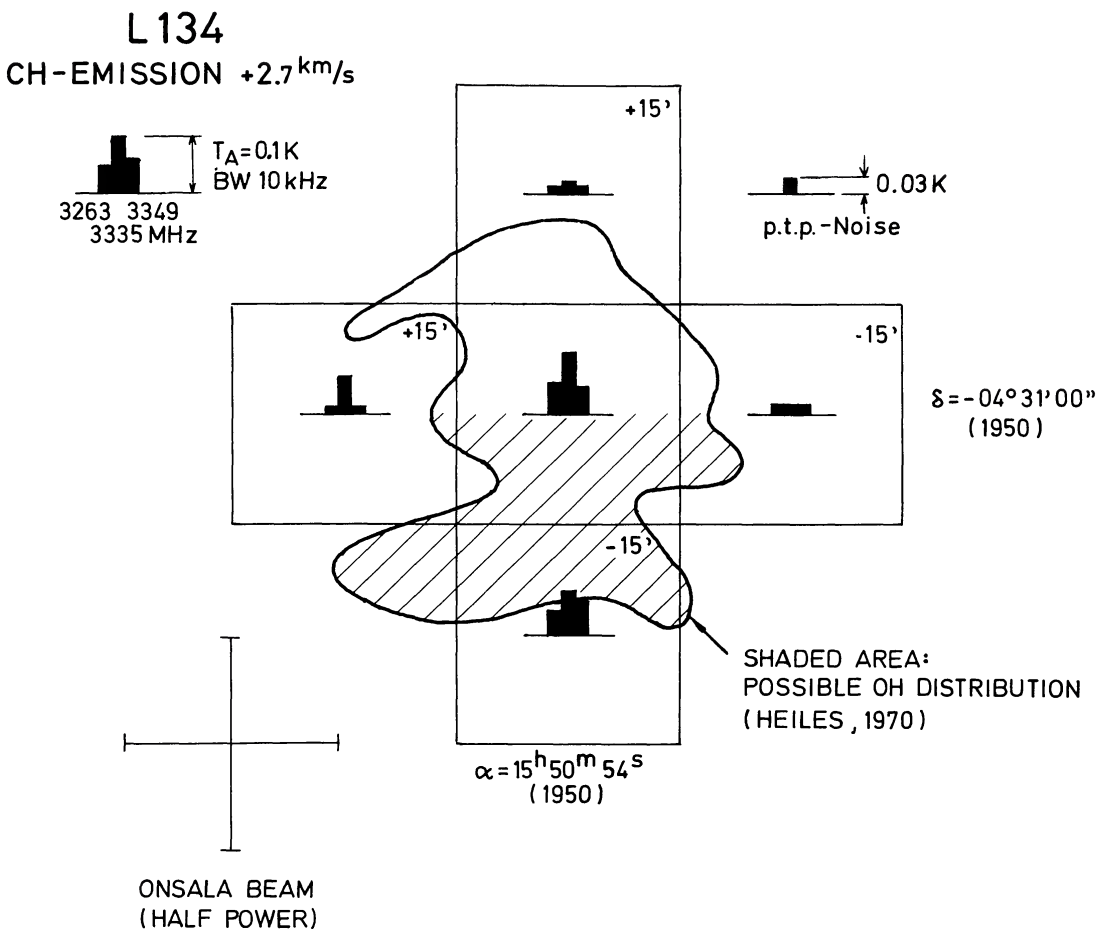

FIG. 27.—CH observations toward L134, superposed on a contour of the approximate optical appearance of the cloud on the Mount Palomar Sky Survey Print (Heiles 1970). The CH antenna temperatures are represented by bars as shown at upper left.

b) G114.2+14.8 (Heiles's Cloud 1)

Figure 28 demonstrates our CH spectra, observed for all three transitions, in the direction of Heiles's Cloud 1. They display the typical LTE-like appearance of a dark dust cloud. One infers that the half-power line width equals about 1.1 km s^{-1}, i.e., somewhat larger than toward the L134 region, and in good agreement with the OH line width (Turner 1973). As in the case of the L134 region, the upper OH satellite is fairly strong, and the lower one absent (within the observational errors).

The OH data, observations of CO (Penzias *et al.* 1972) and of 6 cm H_2CO (Heiles 1973) show good agreement with the CH velocities. The velocities of these species are compatible with -4.5 ± 0.5 km s^{-1}. It should be mentioned that Heiles (1970) suspects the existence of two or three separate OH features. There is, however, no clear evidence of such a structure in the CH spectra. This could be due to the fact that the CH antenna temperatures are much lower than those for OH.

c) Per OB 2 region; G158.3−20.5 (NGC 1333); G159.3−20.2 (center of Per OB 2); G160.5−17.8 (IC 348)

This extended dust cloud is situated in the region of the young stellar association Per OB 2 (Sancisi *et al.* 1974). This cloud is particularly interesting because it is located in a region of recent star formation. T Tauri stars seem to be associated with the dark nebulosity near the open cluster IC 348 and the reflection nebula NGC 1333. Several Herbig-Haro objects have been found in the area around NGC 1333. A large, dense molecular cloud with narrow lines (width $\lesssim 2$ km s^{-1}) from NH_3, CO, CS, HCN, and 2 mm H_2CO has been found toward NGC 1333 at about $+8$ km s^{-1} (Lada *et al.* 1974*b*). This agrees well with the CH velocity obtained toward NGC 1333 (see Table 4). The CH line width (~ 3 km s^{-1}) is larger than the widths found for the molecular lines. Most likely this is due to the much larger beamwidth used for the CH observations. It should be mentioned that Dickinson, Kojoian, and Strom (1974) have observed strong H_2O emission at about -25 km s^{-1} in the direction of NGC 1333.

Figure 29 depicts our weak main line CH spectrum, with a peak at about $+9$ km s^{-1}, obtained toward IC 348. This object and the star o Per are only 6′ apart. Optical CH absorption has recently been detected toward this star

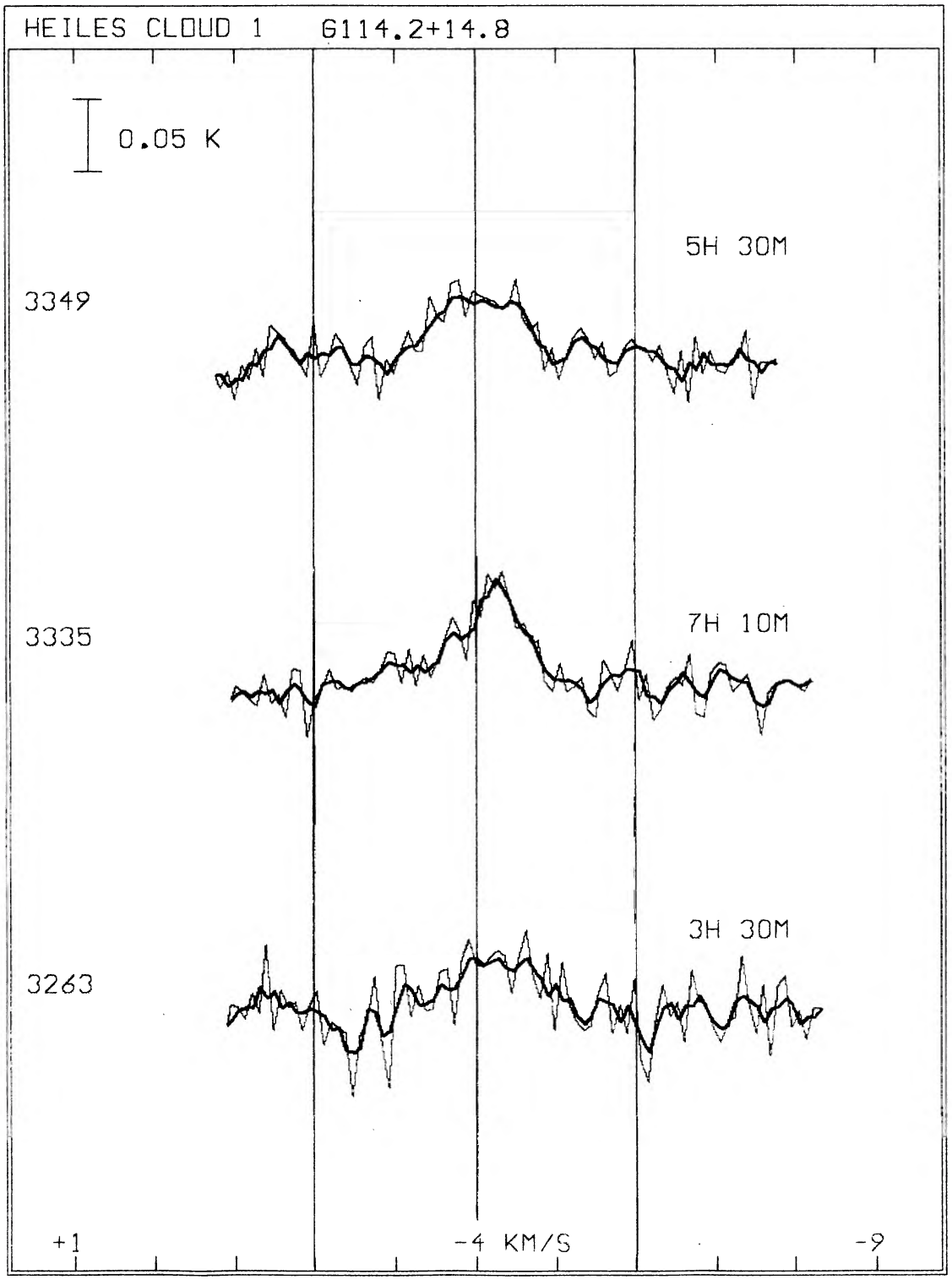

FIG. 28.—CH spectra toward Heiles's Cloud 1. Heavy lines are three-point running means of 1 kHz spectra (*light lines*).

(Cohen 1973; Chaffee 1974). The optical velocities found by these authors are $+6$ and $+8$ km s^{-1}, respectively. CO has been found by Milman (1974) in the direction of IC 348, with a peak velocity of $+8$ km s^{-1} and a half-power line width of about 2 km s^{-1}, i.e., about the same as for CH. Since the CH spectrum is very weak, the correspondence between the CH and CO data must be considered very good. On account of the large errors in the optically determined velocities, it is fair to say that the optical and radio velocities overlap. The optically determined CH column density is smaller than that determined from the radio observations (see Table 5), perhaps

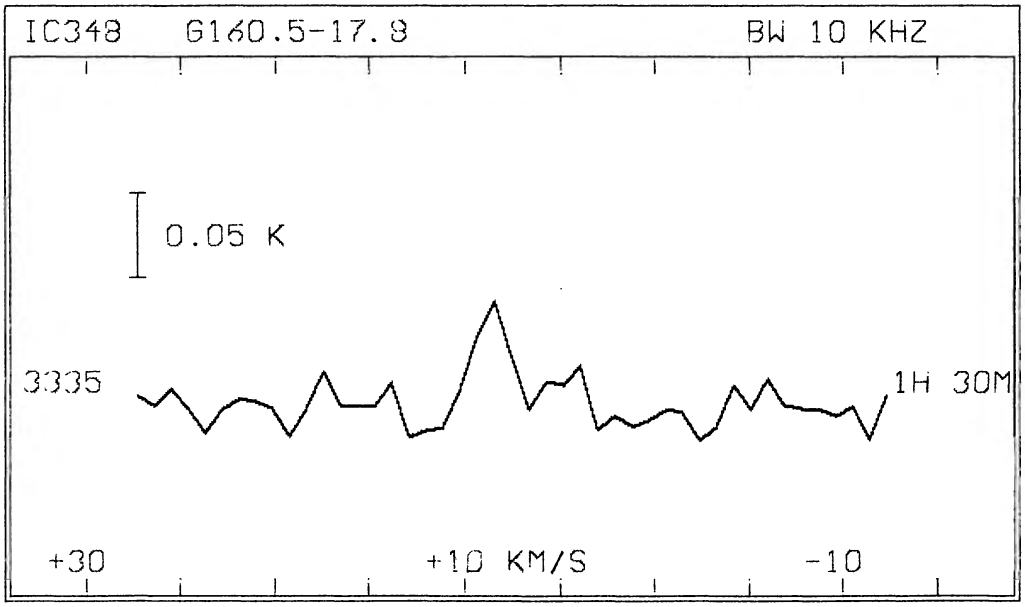

FIG. 29.—CH main line spectrum toward IC 348. No satellite line spectra were determined.

because the dust cloud seems to be located mainly behind o Per (Blaauw 1952). It should also be remembered that the radio data yield an average column density across the 15′ telescope beam.

We also obtained CH spectra of all three transitions toward a point G159.3−20.2 approximately in the center of the Per OB 2 dust cloud. The OH emission shows a local maximum at this point. Provisional CH observations, in adjacent directions, indicate that this is the point of strongest CH emission. As in many other dark clouds the CH transitions appear in LTE ratios. The emission is peaked at a velocity of $+6.5$ km s^{-1}, with a width of about 2 km s^{-1} (i.e., about the same as toward IC 348). An Onsala OH 1667 MHz spectrum obtained in this direction yields a peak velocity of about $+6.4$ km s^{-1} and a line width of about 2 km s^{-1}, i.e., essentially the same values as for CH. A more detailed analysis of the Onsala OH and CH spectra toward the Per OB 2 region, including a comparison with H I and optical extinction data, has recently been performed by Sancisi *et al.* (1974).

d) G172.7−14.4 and G174.3−13.4 (positions in Heiles's Cloud 2)

Heiles's cloud 2 is one of the strongest OH main line emitters of its category. The OH 1667 MHz transition peaks up to about 0.8 K in the NRAO 43 m telescope (Turner 1973), toward both positions which we have observed. It is, therefore, not surprising that the CH emission features (spectra shown in Figs. 30, 31, and 32) are the two strongest we have observed thus far toward any dust cloud. The CH main line peaks at no less than about 0.2 K in both directions.

The high-resolution, low-noise spectra toward G174.3−13.4 (Fig. 32) are suitable for a check of the accuracy of our CH rest-frequency determination (Rydbeck *et al.* 1974*c*). Figure 33 demonstrates the very good correspondence in shape between the CH main line spectrum toward G174.3−13.4 and that of the OH 1667 MHz main line (from Turner 1973). The latter was obtained with a slightly larger beam, about 2′ away from our position. Judging from this comparison alone, the uncertainty in the CH main line rest frequency is less than ± 1 kHz, if the OH rest frequency is that determined by ter Meulen and Dymanus (1972), and if the two species are well mixed in the cloud. A similar comparison with the satellite lines brings down their rest frequency uncertainties to about the same value.

The CH peak velocities are slightly different for the two positions, G172.7−14.4 and G174.3−13.4, *viz.* $+6.1$ and $+5.7$ km s^{-1}. The line widths are 0.9 and 1.3 km s^{-1}, respectively. The corresponding OH values are $+6.5$, $+5.7$, 0.8, and 1.4 km s^{-1}, i.e., substantially the same as for CH. The H_2CO peak velocities are also about equal to those of CH, but the line widths are considerably smaller, 0.4 and 1.0 km s^{-1}, as expected for this heavier molecule.

There appear to be at least two OH velocity components throughout the Cloud 2 region (Heiles 1970; Turner 1973), a strong one at the velocities just mentioned, and a weaker one at a slightly lower velocity. No such velocity structure is readily discernible in our high-resolution CH spectra, Figures 30 and 32. However, 6 cm H_2CO observations also indicate the presence of a second, weak component (Dieter 1973; Heiles 1973). Data of Palmer *et al.* (1969) indicate that the 6 cm H_2CO absorption is strongly correlated with the optical extinction. Turner (1973), however, cites unpublished observations which show that there is an extended region of OH and H_2CO around

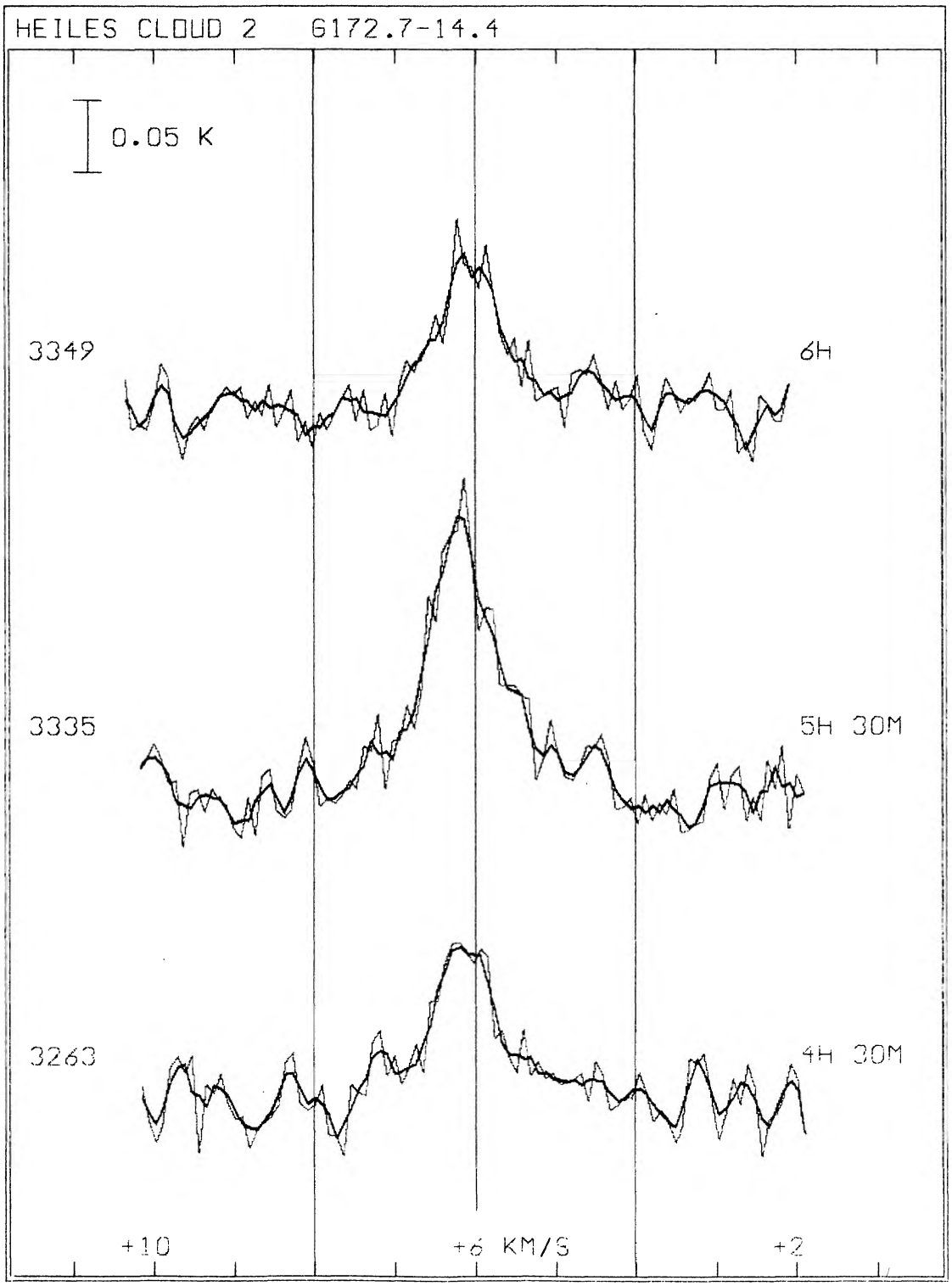

FIG. 30.—CH spectra toward G172.7−14.4 in Heiles's Cloud 2. Heavy lines are three-point running means of 1 kHz spectra (*light lines*).

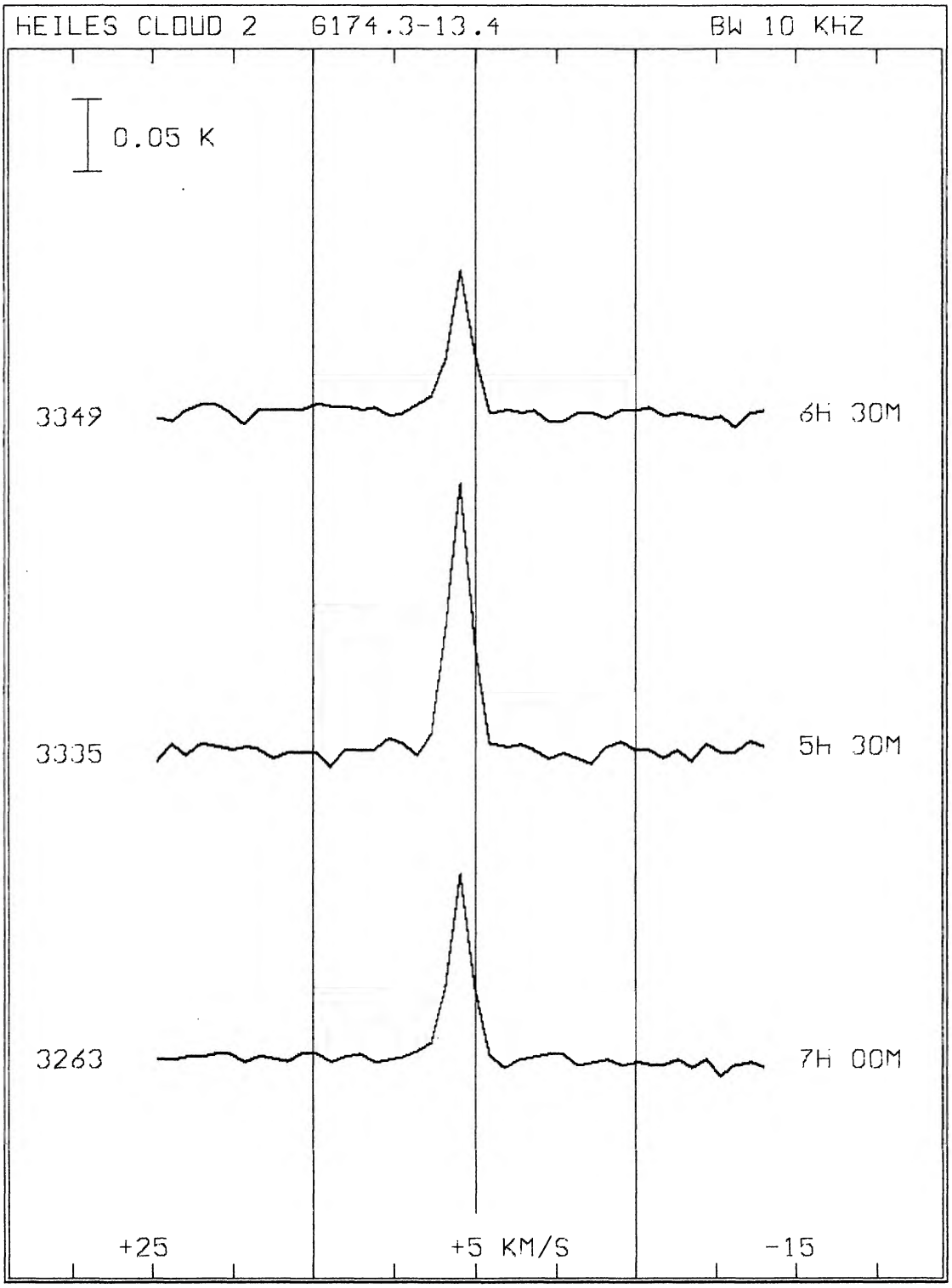

FIG. 31.—CH spectra toward G174.3−13.4 in Heiles's Cloud 2

the (optically visible) dust cloud. According to Heiles and Gordon (1973), the relative abundance of OH to H_2CO varies by a factor of 5 across the cloud. A recent discussion of Cloud 2 has been given by Davies (1973).

CO, at a peak velocity of $+5.2$ km s^{-1} (perhaps too low), and with a line width of about 3 km s^{-1}, has been observed toward G174.3−13.4 (Penzias *et al.* 1972). No NH_3 has been seen in this direction, however (Cheung *et al.* 1973).

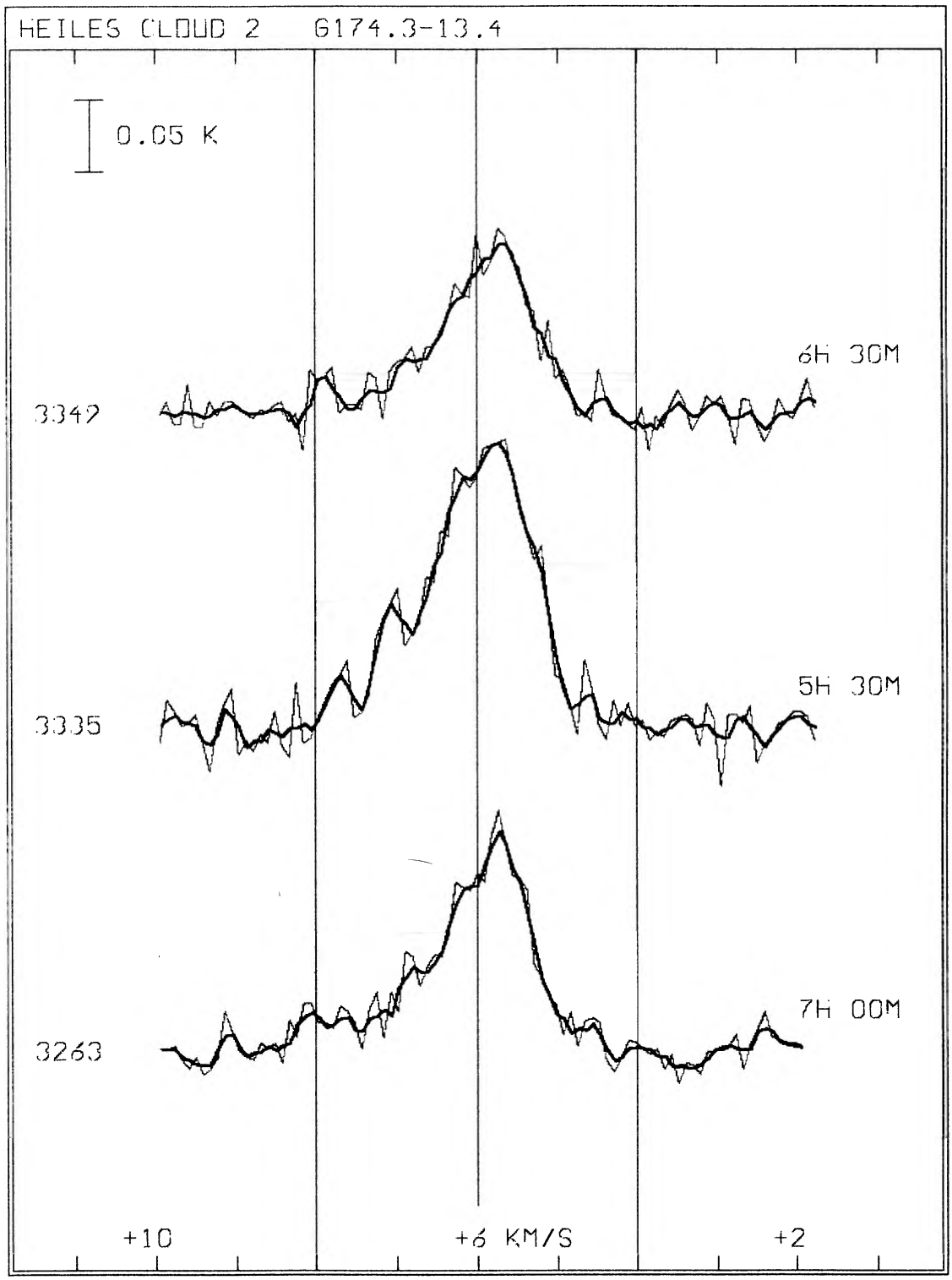

FIG. 32.—CH spectra toward G174.3−13.4 in Heiles's Cloud 2. Heavy lines are three-point running means of 1 kHz spectra (*light lines*).

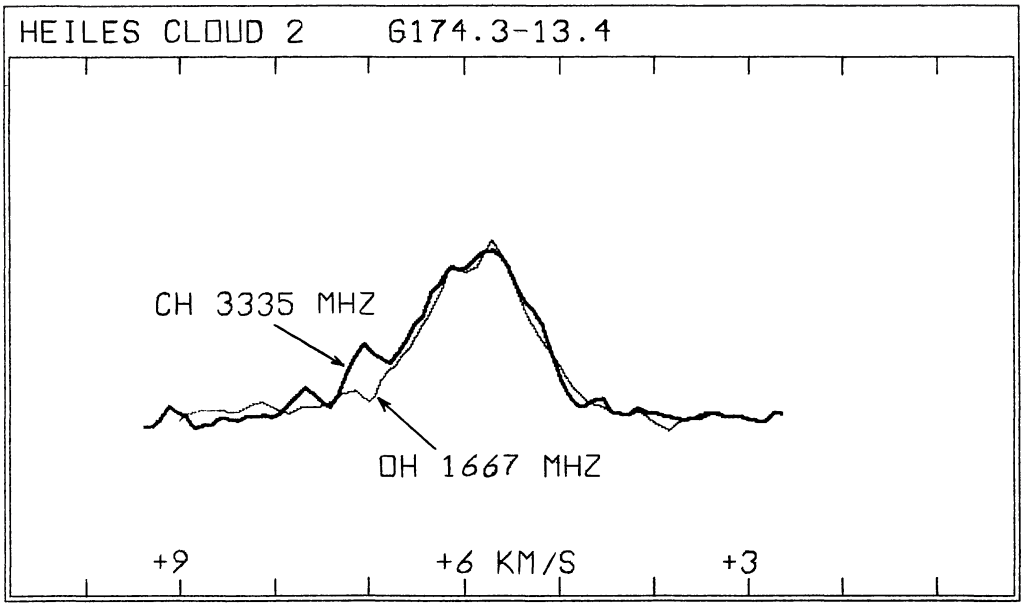

FIG. 33.—Comparison between our 3 kHz CH main line spectrum and an OH 1667 MHz spectrum (from Turner 1973; velocity scale based on the rest frequency 1667.35903 MHz) toward G174.3−13.4 in Heiles's Cloud 2. The spectra have been scaled to the same height. If the OH spectrum is used as a reference, the very good agreement in shape limits the velocity uncertainty of the CH spectrum to less than ± 0.1 km s^{-1} (± 1 kHz).

All OH transitions appear in approximate LTE ratios toward G172.7−14.4. In the other direction, G174.3−13.4, there are, however, indications of slight anomalies in the satellite features, and perhaps also in the main lines. In the former direction, we see no significant departures from the LTE ratios in our CH spectra. Toward G174.3−13.4, however, both CH satellite lines seem to be enhanced, especially the lower one (cf. Fig. 32). Since these CH features are quite strong, one is tempted to believe that significant CH satellite anomalies exist in this cloud. We will return to this problem in § VI.

e) G93.5+9.6 (L1036); G97.0+10.1 (L1082); G150.2+3.9 (L1399)

These Lynds dust clouds were chosen for observation from practical considerations, because of their high declinations. Our CH data for the three directions are given in Tables 4 and 5. Dieter (1973) found 6 cm H_2CO absorption toward L1036 and L1399, at velocities close to ours, but not in the direction of the third cloud. Minn and Greenberg (1973*a*) found 6 cm H_2CO absorption in the direction of L1082 (a Barnard object), but at a velocity of -39 km s^{-1}, which was not covered by our observations. Finally it should be mentioned that the OH velocities reported by Cudaback and Heiles (1969), near our positions in L1082 and L1399, differ considerably from ours, and also from those reported for H_2CO by Minn and Greenberg (cf. Table 4).

V. NEGATIVE RESULTS

Table 6 lists sources searched in which no detection of CH was made within the limits given. The sources have been divided into three groups in the table and will be discussed in that order.

a) OH/IR Stars

Stars which are strong infrared sources and also exhibit OH maser emission appear to be either M-type supergiants or Mira variables (e.g., Hyland *et al.* 1972; Wilson and Barrett 1972). The apparent supergiants thus far discovered have their peak OH microwave emission at 1612 MHz. The Mira variables may be more luminous in either the 1612 MHz line or at the main OH lines. Both types of star may show H_2O maser emission (e.g. Dickinson, Bechis, and Barrett 1973), and typically exhibit OH emission in two distinct velocity ranges, with the separation between these being greater for the supergiants. An infrared intensity in excess of that expected from a blackbody is frequently observed at 10–20 μ, suggesting the presence of a circumstellar dust shell. Carbon monoxide has been detected in the supergiants at infrared (Geballe, Wollman, and Rank 1973), but not at microwave frequencies. Significantly, it seems that all these stars are oxygen-rich and that none are carbon stars; Hyland *et al.* (1972) conclude that the OH is probably photospheric, rather than interstellar. Recent interferometric studies of the OH emission from NML Cyg and VY CMa (Masheder, Booth, and Davies 1974) can be interpreted in terms of an expanding, rotating gas cloud.

TABLE 6

UPPER LIMITS OF CH ANTENNA TEMPERATURES IN VARIOUS SOURCES

Galactic Source Number	Position (1950)		Line	Antenna Temp. Upper Limit[a]	Velocity Interval[b]	N_{CH}[c]
	RA	DE	MHz	K	km s^{-1}	10^{13} cm^{-2}
OH/IR Stars						
OH26.5+0.6	$18^h34^m52^s$	$-05^\circ27'24''$	3263	0.03	-7 ,+37 (+80)	
G35.3+40.3	16 23 35	19 00 18	3335	0.02	-36,+8 (+51)	
(U Her)			3263	0.02		
G77.9+0.2	20 26 54	38 56 00	3349	0.02	-70,-26 (+17)	
(ON4)			3349	0.02	-49,-5 (+38)	
			3335	0.03	-49,-5 (+38)	
			3263	0.02	-70,-26 (+17)	
G80.8-1.9	20 44 39	39 55 42	3349	0.03	-42,+42	
(NML Cyg)			3335	0.02		
			3263	0.02		
G114.6-10.6	23 55 53	51 06 36	3263	0.02	+5 ,+49 (+92)	
(R Cas)						
G239.3-5.1	07 20 55	-25 40 11	3335	0.03	-6 ,+38 (+81)	
(VY CMa)			3263	0.03		
Objects with Optical CH or CH^+ Absorption						
G6.3+23.6	16 34 26	-10 28 23	3335	0.02	-44, 0 (+43)	3.0
(ζ Oph)						
G166.6-23.7	03 43 21	23 47 39	3335	0.03	-4 ,+40 (+83)	
(23 Tau)						
G172.4-2.7	05 12 15	33 47 40	3335	0.04	-51,+53 (+96)	
(IC 405)			3263	0.03	-21,+23 (+66)	
G357.8+20.7	16 24 07	-18 20 40	3263	0.03	-21,+23 (+66)	5.6
(χ Oph)						
Other Sources						
G76.2+5.8	19 57 44	40 35 46	3335	0.02	-106,-68 (-18)	
(Cyg A)			3335	0.02	-17,+27 (+70)	
			3263	0.03	-17,+27 (+70)	
G119.9-22.9	00 34 00	39 35 00	3335	0.02	-525,-435	
(M31, Andromeda)						
G123.1-6.3	00 49 58	56 20 33	3335	0.03	-21,+23 (+111)	
(NGC281, S184)						
G179.9-0.0	05 42 00	29 00 00	3335	0.03	-21,+23 (+66)	
(Anticenter)						

a. 1/2 peak-to-peak noise of 10 kHz data.

b. Between the stated upper limit and the value in parentheses, only half the integration time was obtained, so the upper limit of the antenna temperature is $\sqrt{2}$ times the value in the preceding column. Velocities are relative to the local standard of rest.

c. Determined from optical interstellar absorption lines by Frisch (1972).

We have observed two of the well-studied supergiants, VY CMa and NML Cyg, the type II OH/IR source ON4 (Elldér, Rönnäng, and Winnberg 1969), and a fourth strong source, OH 26.5+0.6 (Andersson *et al.* 1974), which has an integrated 1612 MHz flux characteristic of a supergiant, but a spectrum consistent with a Mira variable (Type II OH/IR star). In addition, observations were made of R Cas and U Her, two of the Mira variables which have their maximum OH emission at 1665/1667 MHz (Wilson *et al.* 1972). The observations are summarized in Table 6. The results are all negative, with the possible exception of the NML Cyg direction, where the possible presence of a broad, weak emission feature ($T_A \approx 0.02$ K) in the velocity interval +3 to +14 km s^{-1} seems more likely to be associated with the general distribution of interstellar gas in the Cyg X region than with NML Cyg itself.

The absence of detectable CH emission is not surprising, considering the OH properties of these objects. The $^2\Pi_{1/2}, J = 1/2$ state of CH does not appear to mase strongly, so that if CH is present in the photospheres or circumstellar clouds associated with OH/IR stars, it may be detected only with much greater spatial resolution than is available with our instrumentation. We note that formaldehyde is also not observed toward the supergiants (Zuckerman *et al.* 1970; the Mira variables do not seem to have been studied for H_2CO), and, as mentioned above, none of the OH/IR stars are carbon stars.

b) Optical Sources

We have also investigated the H I regions in the directions of bright stars for which CH or CH^+ has been observed in absorption in the optical spectra. The locations are listed in Table 6. The star χ Oph has the largest CH column density of the 30 stars studied by Frisch (1972), while ζ Oph has been extensively studied, for example, by Herbig (1968) and from the *Copernicus* satellite (Jenkins *et al.* 1973). The star 23 Tau is in the midst of a striking reflection nebulosity in the Pleiades, and the detection of CH might be important for theories of interstellar grains (CH^+, but not CH, is seen optically in absorption for this star). IC 405 shows both an emission and a reflection spectrum, and includes the star AE Aur, which exhibits strong optical CH absorption (Münch 1964).

In all cases our results were negative.[3] Observations with larger antennas and/or longer integration times are desirable, since a comparison of optical and radio data may provide valuable information on molecular excitation, as well as insuring the compatibility of the data-reduction procedures for these two spectral regions. In addition, microwave observations are necessary to distinguish between circumstellar and interstellar CH (important for models of grain formation and destruction), and to compare these clouds with those in the directions of Cas A and Cyg X, for instance.

c) Other Sources

We have observed in four directions, listed in Table 6, associated with objects not belonging to the categories treated above.

The extragalactic source Cyg A exhibits OH and H_2CO absorption at about +4 km s^{-1} (Goss 1968; Zuckerman *et al.* 1970). Although we have an indication of CH main line emission at that velocity, we tentatively consider the present result to be negative.

H_2CO and OH have been detected in absorption in three external galaxies (Weliachew 1971; Gardner and Whiteoak 1974). We tried to detect the CH main line in Andromeda, M31, at a position in the southwestern part near the major axis, where the H I emission is strong and relatively narrow (Gottesman, Davies, and Reddish 1966). The result was, however, negative (see Table 6).

Negative results were also obtained for the main CH line in the direction of the open cluster NGC 281 (S184) where OH, H_2O, and CO have been sought but not detected (Turner 1969*b*; Turner *et al.* 1970*a*; Wilson *et al.* 1974), and in the galactic anticenter direction.

VI. THEORETICAL CONSIDERATIONS OF EXCITATION TEMPERATURE AND OPTICAL DEPTH DETERMINATIONS

In order to evaluate the excitation temperatures and the optical depths, we have to study and compare the equations of radiative transfer for the three CH transitions in considerable detail. If we introduce the notations T_m and τ_m, which denote the excitation temperature and the optical depth of the main line, $T_{A,m}$ for the line antenna temperature observed for the same, with subscripts u and l for the upper and lower satellites, and $T_{tb} = T_B + T_{CR}/F$ for the total background temperature (see the Cas A section), we may write

$$\begin{aligned} T_{A,m} &= F(T_m - T_{tb})[1 - \exp(-\tau_m)], \\ T_{A,u} &= F(T_u - T_{tb})[1 - \exp(-\tau_u)], \\ T_{A,l} &= F(T_l - T_{tb})[1 - \exp(-\tau_l)]. \end{aligned} \tag{16}$$

It is to be noticed that not only T_{tb} but also the beam dilution factor F varies from object to object.

[3] We have subsequently detected CH in the direction of the star ζ Per (Hjalmarson *et al.* 1975).

The satellite-to-main-line intensity ratios, which are important quantities, become

$$Q_{um} = \frac{1 - T_{tb}/T_u}{1 - T_{tb}/T_m}\frac{T_u}{T_m}\frac{1 - \exp(-\tau_u)}{1 - \exp(-\tau_m)} \equiv \frac{1 - T_{tb}/T_u}{1 - T_{tb}/T_m} Q_{um}{}^0 ,$$
$$Q_{lm} = \frac{1 - T_{tb}/T_l}{1 - T_{tb}/T_m}\frac{T_l}{T_m}\frac{1 - \exp(-\tau_l)}{1 - \exp(-\tau_m)} \equiv \frac{1 - T_{tb}/T_l}{1 - T_{tb}/T_m} Q_{lm}{}^0 . \quad (17)$$

Furthermore (see Rydbeck *et al.* 1975),

$$\tau_u = \frac{1}{2}\frac{T_m}{T_u}\tau_m , \quad \text{and} \quad \tau_l = \frac{1}{2}\frac{T_m}{T_l}\tau_m , \quad (T_u, T_l \neq 0) . \quad (18)$$

In the case $T_m = T_u = T_l$, which corresponds to LTE when $T_m > 0$, we find by relations (17) and (18) that $Q_{um} = Q_{lm} = Q_{um}{}^0 = Q_{lm}{}^0$. Then Q_{um} assumes the particularly simple form

$$Q_{um} = \frac{1}{1 + \exp(-\tau_m/2)} = \tfrac{1}{2}[1 + \tanh(\tau_m/4)] , \quad (T_m = T_u = T_l) . \quad (19)$$

Q_{um} is greater than 1/2 when τ_m is positive, tends to 1 for an optically thick medium, and tends to zero for a strongly masing medium ($-\tau_m \gg 1$).

Let us first study the basic case $T_m = T_u = T_l$. The optical depth becomes by equation (19)

$$\tau_m = 2 \ln \frac{Q_{um}}{1 - Q_{um}} = 8(Q_{um} - 1/2)[1 + \tfrac{4}{3}(Q_{um} - 1/2)^2 + \cdots] . \quad (20)$$

Relations (16) and (19) now yield the following exact expression for T_m,

$$T_m(=T_u = T_l) = T_{tb} + \frac{T_{A,m}}{8F}\frac{(2Q_{um})^2}{Q_{um} - 1/2} . \quad (21)$$

When $Q_{um} - 1/2$ goes from $+0$ to -0, τ_m changes from $+0$ to -0, and T_m from $+\infty$ to $-\infty$.

In order to get reliable values of T_m and τ_m, *long* integration times must be used for signals as weak as those of CH.

In the general case with unequal excitation temperatures we have four unknown quantities (F and T_{tb} are assumed to be known and we continue to assume eq. [18]) but only three independent equations, (16), and we need another set of measurements to be able to determine the three excitation temperatures and τ_m. When no discrete continuum background source is available, the obvious and important choices are the (interrelated) line ratios at half-power points of the main line, i.e., when $\tau_m = \frac{1}{2}\tau_{m,\max}$ for the optically thin medium (when we have a strong background point source, as in the case of Cas A, the off-line-center, half-power measurements are replaced by on-line-center, off-background-source-center [e.g., half-power] measurements). This has been discussed in considerable detail by Rydbeck *et al.* (1975). However, in practice CH spectra are of insufficient quality to allow an unambiguous application of this method.

We will now apply the derived expressions to the most reliable dark dust cloud spectra. (For details of the various spectra the reader is referred to the section on dust clouds. The F values used have been estimated visually from Palomar Sky Survey prints). We will first assume that LTE exists and see what excitation temperatures and optical depths can be inferred.

In the case of LTE, Q_{um} must be equal to Q_{lm} and be greater than 1/2. As we have found this to be the case in most directions toward those dust clouds where the signal-to-noise ratio has been good enough for $T_{A,m}$, Q_{um}, and Q_{lm} to be determined with reasonable accuracy, the assumption of LTE is generally not contradicted by the observations.

Lynds's Cloud 134N (G6.0+36.7).—We observe $T_{A,m} = 0.11$ K and $Q_{um} = Q_{lm} = 0.52$, and take $F = 0.40$. With $T_{tb} = 2.8$ K, relations (21) and (20) yield

$$T_m(=T_u = T_l) = 4.7 \text{ K}; \quad \tau_m = 0.16 .$$

Turner (1973) obtains $T_{m,\mathrm{OH}} = 6.0$ K.

Heiles' Cloud 1 (G114.2+14.8).—For $T_{A,m} = 0.07$ K and $Q_{um} = Q_{lm} = 0.56$, $F = 0.25$ yields

$$T_m = 3.5 \text{ K}; \quad \tau_m = 0.48 .$$

Turner (1973) obtains $T_{m,\mathrm{OH}} = 4.4$ K.

Per OB 2 dust cloud (*G159.3−20.2*).—For $T_{A,m} = 0.13$ K and $Q_{um} = Q_{lm} = 0.52$, $F = 0.50$ implies

$$T_m = 4.6\ \mathrm{K}; \qquad \tau_m = 0.16\,.$$

No value of $T_{m,\mathrm{OH}}$ seems to have been determined.

Heiles's Cloud 2 (*G172.7−14.4*).—For $T_{A,m} = 0.19$ K and $Q_{um} = Q_{lm} = 0.55$, $F = 0.45$ yields

$$T_m = 4.1\ \mathrm{K}; \qquad \tau_m = 0.40\,.$$

Turner (1973) finds $T_{m,\mathrm{OH}} \approx 6$ K (point 2 GK in his notation). It is interesting to note that $T_{m,\mathrm{OH}}/T_{m,\mathrm{CH}} = 1.3$ for L134N and Heiles's Cloud 1 (note their different opacities), and 1.5 for G172.7−14.4 in Heiles's Cloud 2. Within the errors of measurements, $T_{m,\mathrm{OH}}$ thus appears not to be more than about 30–50 percent higher than $T_{m,\mathrm{CH}}$, if LTE exists (see also G174.3−13.4 in Heiles's Cloud 2). It should be added in this context that our values of τ_m appearing in Table 5 are based on the assumption that $T_{m,\mathrm{CH}} = T_{\mathrm{kin}}$, where T_{kin} was taken as a mean of the OH main line and the CO excitation temperatures.

Heiles's Cloud 2 (*G174.3−13.4*).—The observations yield $T_{A,m} = 0.20$ K; $Q_{um} = 0.60$; $Q_{lm} = 0.75$, while $F = 0.5$. In this case one must suspect complications as far as the lower satellite line is concerned. Let us, however, assume first that the main and the upper satellite lines have an LTE relation. Relations (21) and (20) then yield

$$T_m = 3.5\ \mathrm{K}; \qquad \tau_m = 0.81\,.$$

Turner (1973) obtained $T_{m,\mathrm{OH}} = 4.3$ K (point 2D in his notation).

Since, however, Q_{lm} is considerably larger than Q_{um}, we must consider the general situation when the excitation temperatures are unequal. First we can assume that the spectra are due to two clouds; one main cloud where LTE exists, and one anomalous cloud responsible for the enhanced part of the lower satellite spectrum. This latter cloud could either be a foreground or background cloud, or be embedded in the main cloud. In order to affect only the lower satellite, such a cloud would have to be subjected to a strong population transfer within the hyperfine doublet levels, for instance by a far-infrared background (as discussed in more detail in the following section).

We will consider the case where the anomalous cloud is in front of the main cloud. If we denote the excitation temperature of the lower satellite line in the anomalous cloud by $T_l < 0$ and assume that $T_l = T_m(=T_u)$ in the main cloud, and that F is the same for both clouds, $T_{A,l}$ can be written, for a foreground anomalous cloud, as

$$T_{A,l} = F\{(|T_l| + T_{tb})[\exp(+|\tau_l|) - 1] + [\exp(+|\tau_l|)](T_m - T_{tb})[1 - \exp(-\tau_m/2)]\}\,, \tag{22}$$

i.e. the lower satellite emission from the main cloud is amplified by the factor $\exp(+|\tau_l|)$. Since

$$T_{A,m} = F(T_m - T_{tb})[1 - \exp(-\tau_m)]\,, \tag{23}$$

the resulting, *total* Q_{lm} value, denoted $Q_{lm}^{(t)}$ becomes,

$$Q_{lm}^{(t)} = \frac{|T_l| + T_{tb}}{T_m - T_{tb}} \cdot \frac{\exp(+\tau_l) - 1}{1 - \exp(-\tau_m)} + \exp(+|\tau_l|)Q_{um}\,. \tag{24}$$

The case of a background cloud with $T_l < 0$ can be treated similarly.

In Figure 34 we have plotted (3 kHz frequency resolution throughout) the two satellite line spectra, and the main line spectrum multiplied by 0.55 for best congruence with the upper satellite spectrum. The latter has been shifted 0.6 kHz toward higher velocities from its position in Figure 32 for best velocity correspondence with the two other spectra (this shift is well within the rest frequency uncertainty). Within the noise fluctuations, the upper satellite and the normalized main line spectra are congruent. To reduce the noise, we have averaged these two spectra and subtracted this average from the lower satellite line spectrum in order to obtain $Q_{lm}^{(t)} - Q_{um}$. The resulting spectrum is also shown in Figure 34. What remains is a feature of maximum amplitude $\approx 0.16T_{A,m}$, with a half-width of about 0.7 km s^{-1} and a peak velocity of about +5.6 km s^{-1}, or somewhat lower than that of the main cloud. The OH satellite line anomalies observed at about the same velocity (Turner 1973) could also be due to the same "anomalous" cloud.

If we assume that the anomalous cloud is in front of the main cloud and that $|\tau_l|^2 \ll 1$, we obtain by relation (24)

$$0.16 \approx \frac{|\tau_l|}{\tau_m} \frac{|T_l| + T_{tb}}{T_m - T_{tb}}\,. \tag{25}$$

With $T_{tb} = 2.8$ K and $T_m = 3.5$ K, this yields

$$|T_l| \approx -2.8\left(1 - \frac{\tau_m}{25|\tau_l|}\right)\,.$$

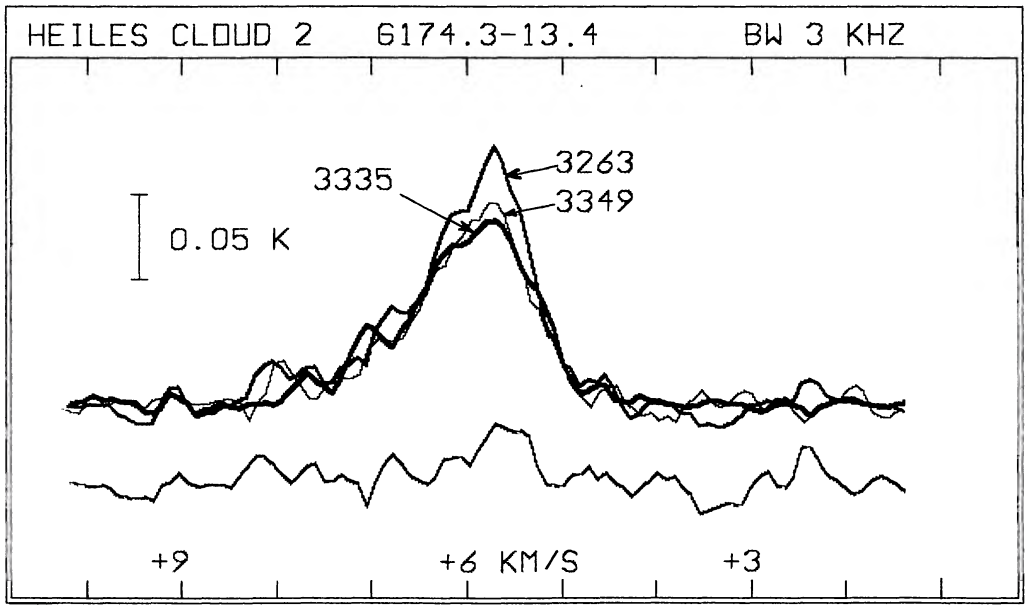

FIG. 34.—CH spectra toward G174.3−13.4 in Heiles's Cloud 2. The three upper spectra are identified by their transition frequencies in MHz. The main line spectrum has been multiplied by 0.55 for best congruence with the upper satellite spectrum. The latter has been shifted 0.6 kHz toward higher velocities from its position in Fig. 32 for best velocity correspondence to the two other spectra. The antenna temperature scale refers to the satellite lines. The lower spectrum is the difference between the lower satellite line and the average between the upper satellite and the normalized main line spectra. A possible interpretation of this resulting spectrum is described in the text.

Since $|T_l|$ must be positive (and $\neq 0$ for our approximations to hold), $|\tau_l|$ is smaller than $\tau_m/25$. This should be compared with the LTE ratio $\tau_l = \tau_m/2$. The masing front cloud therefore is optically thin, in accordance with our assumptions. For example, if we assume that $T_l = -5.6$ K, $|\tau_l| = \tau_m/75$.

Finally, we will examine the situation when all three lines have negative excitation temperatures and emanate from one and the same cloud. The main line excitation temperature is assumed to be the same as that determined for the dust cloud L1500 (about −10 K) by means of measurements on and off the extragalactic continuum source 3C 123 (G170.6−11.7), which is behind L1500. The details of these measurements, which were performed in 1974 October to December, will be presented in a separate publication. Given the main line excitation temperature, we can calculate the satellite line excitation temperatures for G174.3−13.4 from the Q_{um} and Q_{lm} values by relations (17), assuming $Q_{um}^0 = Q_{lm}^0 \approx 1/2$. With $Q_{um} = 0.60$ and $Q_{lm} = 0.75$ we get $T_u = -5$ K and $T_l = -3$ K. By equation (16) the main line optical depth becomes $\tau_m = -0.03$ (similarly one finds from the spectra toward 3C 123 [$T_{tb} = 5.1$ K] that $Q_{um} = 0.58$ and $Q_{lm} = 0.64$; i.e., $T_u \approx -7$ K and $T_l \approx -5$ K).

Of the different models presented here for the position G174.3−13.4 in Heiles's Cloud 2, we believe this last one to be the most probable, even though it assumes a negative main line excitation temperature determined for another dust cloud. However, it seems natural to assume that conditions are similar in the dark dust clouds.

Another indication that CH exhibits weak maser properties also in dark dust clouds is obtained from our observations toward M17. The very narrow CH emission features at +24 km s^{-1} coincide with a sharp H_2CO absorption, typical of a cold (dust) cloud; in this case there is clear reason to believe that it lies in front of the continuum source (Lada and Chaisson 1975). The total background brightness temperature $T_{tb} \approx 65$ K indicates that the CH excitation temperature in this foreground cloud is negative.

If CH is a weak maser even in the dark dust clouds, CH exhibits a very coherent picture in that the $^2\Pi_{1/2}$, $J = 1/2$ Λ doublet is inverted almost everywhere, with somewhat greater inversion for the satellite lines than for the main line. We will return to this question in connection with our pumping considerations, § VII.

VII. ENERGY LEVELS AND EXCITATION OF CH

a) Energy Levels

The net Λ doublet frequencies are given to first order by the following expression (Van Vleck 1929; Mulliken and Christy 1931; Dousmanis, Sanders, and Townes 1955):

$$\nu_\Lambda^{(3/2)} \quad \text{or} \quad \nu_\Lambda^{(1/2)} = \pm(J + 1/2)\left[(\tfrac{1}{2}p + q)\left(\pm 1 + \frac{2 - Y}{X}\right) + \frac{2q}{X}(J - 1/2)(J + 3/2)\right](-1)^{J+1/2} \quad (Y > 0), \quad (26)$$

where $Y = A/B$, B is the rotational "constant," A is the spin-orbit coupling "constant,"

$$X = +[4(J - 1/2)(J + 3/2) + (Y - 2)^2]^{1/2},$$

and the two plus signs on the right-hand side of the equation corresponds to $\nu_\Lambda^{(3/2)}$, while the minus signs are appropriate to $\nu_\Lambda^{(1/2)}$. When $Y < 0$, the two $\pm$ signs become $\mp$. The quantity $\nu_\Lambda^{(3/2)}$ corresponds to the nominal states $^2\Pi_{3/2}$, sometimes labeled $F_2(J)$. Similarly, the $^2\Pi_{1/2}$ states (for which the splitting is $\nu_\Lambda^{(1/2)}$) are referred to as the $F_1(J)$ ladder. When $\nu_\Lambda > 0$, the parity is taken to be positive for the upper level of the doublet. The molecular parameters p and q may be expressed as

$$\frac{p}{2} = 2\sum [\langle ^2\Pi|H_{so}|^2\Sigma\rangle\langle ^2\Pi|B(L^+ + L^-)|^2\Sigma\rangle]/(E_\Pi - E_\Sigma), \tag{27}$$

and

$$q = 2\sum [\langle ^2\Pi|B(L^+ + L^-)|^2\Sigma\rangle^2]/(E_\Pi - E_\Sigma), \tag{28}$$

where the summation extends over all vibrational levels of all $^2\Sigma$ states, with the contribution from $^2\Sigma^-$ taken as negative. Matrix elements are taken over both electronic and vibrational wave functions. H_{so} is the spin-orbit coupling operator, and B is the rotational operator $h/(8\pi^2\mu r^2)$. L^+ and L^- are raising and lowering electron orbital operators. The energy of the Σ states above the Π state is denoted $E_\Sigma - E_\Pi$.

Evenson, Radford, and Moran (1971) have, for CH, determined $B = 14.162 \pm 0.001$ cm^{-1} and $Y = 1.99 \pm 0.2$, from (far-) infrared laser magnetic resonance measurements of a flame spectrum. From optical measurements Herzberg and Johns (1969) found $B = 14.190$ cm^{-1} and $Y = 1.97$. Later, optical determinations by Botterud, Lofthus, and Veseth (1973) led to $B = 14.208$ cm^{-1} and $Y = 2.24$. It is interesting to notice that the results found

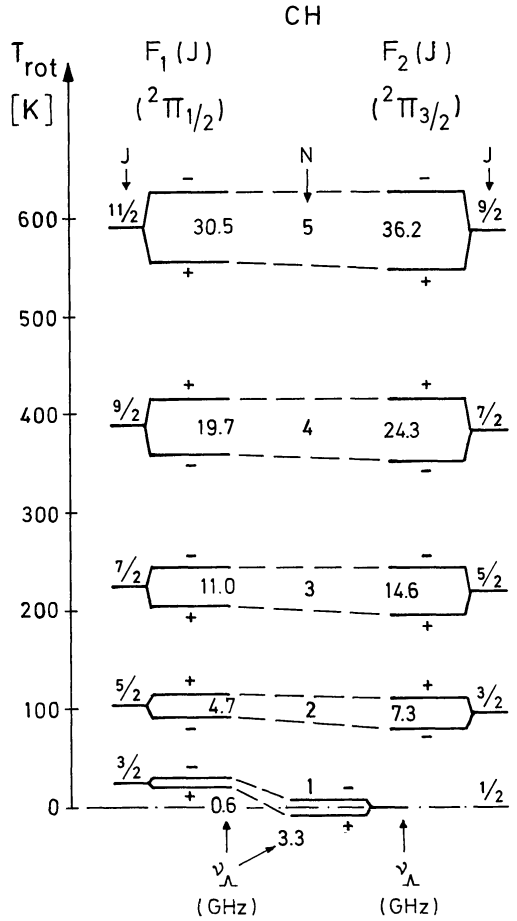

FIG. 35.—The lowest rotational energy levels of CH in the F_1 ($^2\Pi_{1/2}$) and F_2 ($^2\Pi_{3/2}$) ladders as functions of J (or N). The energy is given as the equivalent rotation temperature T_{rot}. The Λ doublet frequencies ν_Λ are shown for $Y = 2$ and $q = 0.038$ cm^{-1} (not to scale). Parities are also included.

by Herzberg and Johns are in better agreement with the far-infrared measurements by Evenson, Radford, and Moran. Douglas and Elliot (1965) found $q = 0.038\ \mathrm{cm}^{-1}$. These results should be compared with the historical measurements by Mulliken and Christy (1931) which led to $B = 14.21\ \mathrm{cm}^{-1}$, $Y = 2.0$, and $q = 0.037\ \mathrm{cm}^{-1}$. It ought to be noted in passing that microwave absorption measurements performed by Dousmanis, Sanders, and Townes (1955) led to $Y = -7.444$ for OH (which thus is an irregular Λ-doublet), whereas Dieke and Crosswhite (1948) found $Y = -7.547$, i.e., a deviation of about 1.4 percent from the microwave measurements.

The rotational energy terms corresponding to equation (26) are, to first order (Hill and Van Vleck 1928; Van Vleck 1929; Dousmanis, Sanders, and Townes 1955),

$$E^{(3/2)} \quad \text{or} \quad E^{(1/2)} = F_2(J) \quad \text{or} \quad F_1(J) = B[(J - 1/2)(J + 3/2) \pm X/2] \quad (Y > 0)\,, \tag{29}$$

with reversed signs when $Y < 0$. In the case of CH, with $Y \approx 2$, for values as small as $N = 2(J = 5/2; 3/2)$, equation (29) can be written

$$\left.\begin{aligned} E^{(1/2)} = F_1(J) &\approx B\{N(N+2) - [N(N+2)]^{1/2}\} \\ E^{(3/2)} = F_2(J) &\approx B\{N^2 - 1 + [N^2 - 1]^{1/2}\} \end{aligned}\right\} \quad (Y \approx 2; N = 2, 3, \cdots)\,, \tag{30}$$

where $J^{(1/2)} = N + 1/2$ and $J^{(3/2)} = N - 1/2$. Thus

$$E^{(1/2)} - E^{(3/2)} = \frac{B}{N}\left(1 - \frac{1}{2N} + \frac{3}{4N^2} - \cdots\right), \quad (Y \approx 2; N = 2, 3, \cdots)\,. \tag{31}$$

Since B corresponds to $\sim$20.4 K for CH, this energy difference is small even for $N = 2$, being about 9.5 K [Note: $E^{(1/2)}(N = 2) \approx 105$ K]. Thus when rotationally excited (for example by collisions), the $F_1(J)$ and $F_2(J)$ ladders should be about equally populated already when $N = 2$ (in contrast to OH).

If $Y = 2 \pm 0$, the interpretation of (26) causes some difficulties. In order to secure an analytical continuation of the coupling coefficients, which appear in the total wave functions, and of the energies appearing in (29), we have assumed that X changes sign with $2 - Y$ when $J = 1/2$, a matter that will be discussed in a later communication. When, therefore, $Y = 2 \pm 0$, $\nu_\Lambda^{(3/2)} \equiv 0$ and $\nu_\Lambda^{(1/2)} = -(p + 2q)$. The corresponding nominal state is labelled $^2\Pi_{1/2}$ and is referred to the $F_1(J)$ ladder as shown in Figure 35, in which we have plotted the CH rotational levels as functions of J (or N) and shown ν_Λ (not to scale) for $Y \approx 2$ and $q = 0.038\ \mathrm{cm}^{-1}$. It is important to note that the $^2\Pi_{1/2}$, $J = 1/2$, and $J = 3/2$ states have the same parities. For the latter state to change parity, Y must be greater than 2.5.

As appears from the Introduction, our measurements yield $p/2 + q = 0.0551\ \mathrm{cm}^{-1}$, which is extremely close to the value 0.0552 recently found by Hammersley and Richards (1974) from elaborate theoretical computations. Their value $q = 0.0379\ \mathrm{cm}^{-1}$ (in very good agreement with that of Douglas and Elliott) must therefore be regarded as very reliable.

In order to study the pumping and cascading of CH through the F_1 and F_2 ladders it is, most obviously, important to detect the next higher rotation states. Because $\nu_\Lambda^{(1/2)}, J = 3/2$, roughly equals 0.6 GHz, there are practical difficulties in detecting this important transition, but the next higher ones, at about 4.7 and 7.3 GHz, should be worth a try. If both are found, Y and q could be determined with great accuracy, as is apparent from Table 7,

TABLE 7

ENERGY LEVELS AND FREQUENCIES OF ROTATIONALLY EXCITED CH Λ DOUBLETS FOR $q = 0.038\ \mathrm{cm}^{-1}$ AND $Y = 1.8$, 2.0, AND 2.2

J	$T_{\mathrm{rot}}^{(1/2)}$ (K)	λ_{rot} (μ)	$\nu_\Lambda^{(1/2)}$ (MHz)		
			$Y = 1.8$	$Y = 2.0$	$Y = 2.2$
A. F_1(J) ($^2\Pi_{1/2}$)					
1/2.....	...	...	3306.494	3306.494	3306.494
3/2.....	25.7	560.7	826	642	445
5/2.....	105.3	136.6	4882	4713	4531
7/2.....	226.7	63.5	11211	11046	10870
9/2.....	389.1	37.0	19819	19656	19481
11/2.....	592.0	24.3	30705	30543	30370
B. F_2(J) ($^2\Pi_{3/2}$)					
3/2.....	96.4	149.2	7439	7255	7058
5/2.....	220.7	65.2	14801	14632	14451
7/2.....	384.5	37.4	24437	24272	24096
9/2.....	588.2	24.5	36351	36188	36014

in which we have calculated ν_Λ as a function of J from equation (20) for three Y-values, 1.8, 2.0, and 2.2, under the assumption that $q = 0.038$ cm^{-1}. The 4.7 GHz transition, for example, varies in frequency by not less than 351 MHz through this range of Y-values. The corresponding variation in the frequency of the 7.3 GHz transition is about the same, or 381 MHz.

b) Excitation Considerations

It appears from the paragraph on Cas A that the excitation temperature of the main line equals about -15 K in the Orion and Perseus arm clouds, and that the satellite line excitation temperatures are of the (rough) order of -7.5 K. Moreover, it appears from the previous chapter that there are indications, in the direction of the dust cloud L1500 (in which the 3C 123 background seems to be weakly amplified) and perhaps also toward G174.3 − 13.4 in Heiles's Cloud 2, that the excitation temperatures are negative also in these objects, with about the same temperature ratios as in the Orion and Perseus arm clouds. Since the excitation mechanisms must vary widely in these different regions, the net, but very small inversion ($h\nu_\Lambda/k \approx 0.16$ K for the ground-state doublet) could be a function of the CH ladder structure itself.

In the Orion and Perseus arm clouds, collisions with H atoms should be considered as a likely mechanism (as was proposed by Townes 1968 for OH). In the denser dust clouds (where the abundance of CH may decrease, however, due to its probable part in the formation of more stable molecules) collisions with H_2 may have to be considered; but these must also lead to a net inversion of the CH ground state doublet, if our excitation temperature estimates (in the previous chapter) are roughly correct. We list the "collisional reactions" as follows (cf. the discussion for OH by Gwinn *et al.* 1973):

$$\text{(I)}\quad \mathrm{H} + \mathrm{CH(lower)} + \text{translational energy} \rightarrow \mathrm{H} + \mathrm{CH(upper)}\,,$$

$$\text{(II)}\quad \mathrm{H_2} + \mathrm{CH(lower)} + \text{translational energy} \rightarrow \mathrm{H_2} + \mathrm{CH(upper)}\,.$$

Process (I) probably destroys nuclear spin information, but not (II). A discussion of these differences falls, however, outside the scope of our present, more preliminary discussion.

CH_2 in its ground state is slightly bent (Herzberg and Johns 1971) and should have a rotation spectrum of the same type as H_2O. Formation of rotationally excited CH by collisions between H (or H_2) and CH_2 (analogous to the mechanism proposed for H_2O by Gwinn *et al.* 1973) may therefore have to be considered. In principle this should not alter much of the following discussion, however. It is interesting to note that, according to Black and Dalgarno (1973), CH_2 may be present with an abundance approaching that of CH in interstellar clouds containing a significant amount of molecular hydrogen.

Process (I) converts the translational energy of an H atom into ground-state CH doublet repopulation via collisional excitation to higher J-values. In each Λ doublet the upper levels are, more or less, selected under the following conditions: (1) the "initial" CH radicals must be essentially nonrotating ("they must be quite cold in the presence of translational energy"); and (2) the H atom that leaves after the collision should form a partial chemical bond with CH, so that the attractive chemical force depends upon the angle of the chemical bond (i.e., it should not be a central force).

The spontaneous relaxation of the rotationally excited CH radical is rapid. In the F_2 ladder it will reach the ground-state doublet in less than a minute. The relaxation time in the F_1 ladder is determined essentially by the small A coefficients connecting the two lowest rotational states, and will equal about half an hour (estimated from the Einstein A coefficients of Burdyuzha and Varshalovich 1973).

If the kinetic temperature is of the order of 100 K (which is possible in the denser spiral arm regions), the collision rate is about $10^{-11} n_{\mathrm{H}}$ [s^{-1}]. With $n_{\mathrm{H}} = 1$ cm^{-3}, there would thus be one collision per 3000 years on the average. Any non–LTE population in the "final" CH ground-state quartet may thus persist for 10 years or more. It should be added in this context that, even at a hydrogen density of about 10^7 cm^{-3} and temperature of, say, 1000 K, the time to thermalize the ground state is very roughly of the order of minutes (cf. the discussions for OH by Gwinn *et al.* 1973).

The following should be emphasized when one considers the relaxation down the ladders. Even though the matrix components $|\langle a|\mu|b\rangle|^2$ (between levels a and b) are comparable for transitions across a Λ doublet and between doublets, the $\nu_{ab}{}^3$ factor contained in the Einstein A coefficient leads to a very great difference between the rates of spontaneous emission (for the two types of transitions).

Furthermore, it is important to note that, especially for CH with its great ladder symmetries (see cf. [30] and Fig. 35), the effect of the $\nu_{ab}{}^3$ term is more or less to retain, throughout the cascade process down to the levels $N = 2$, the population specificity of the state originally produced at higher N-values. The results at $N = 2$ levels should, therefore, be relatively independent of the N- or F-values initially developed by the (for example collisional) excitation.

In cascading down, the lower spin levels have a tendency to be selected by the action of trapped resonant radiation, caused by infrared radiation of the CH radicals during their relaxation to the ground state. The effect of such infrared population transfer (Litvak 1969), so important in the case of CH, will be discussed in more detail in a following section.

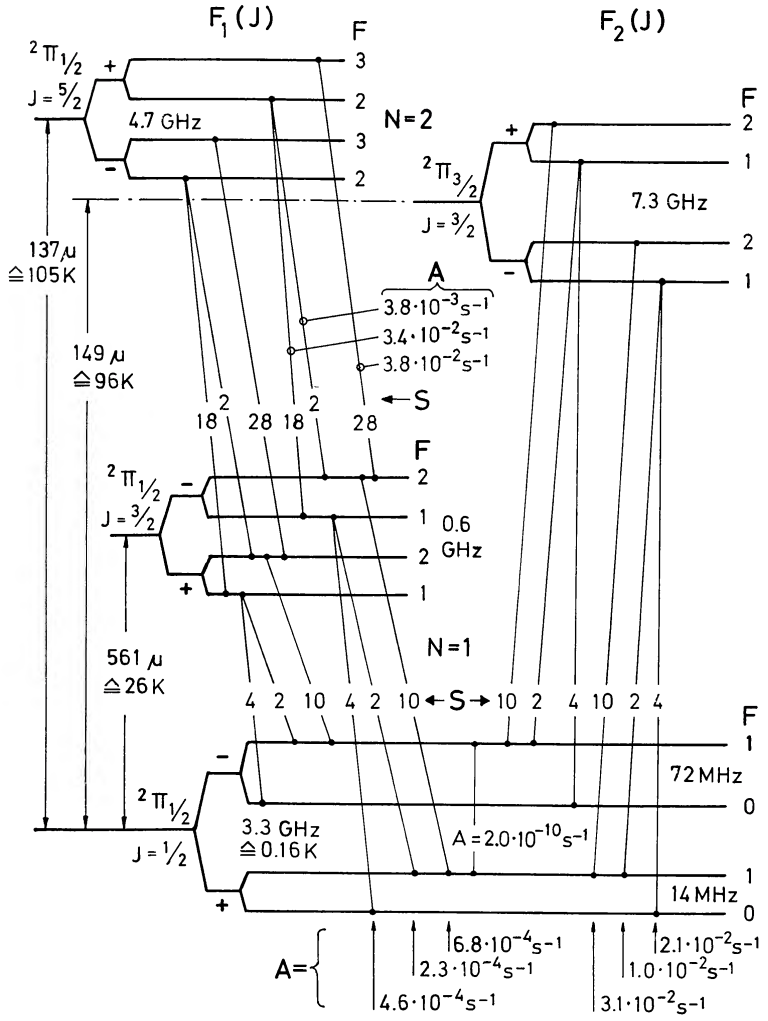

FIG. 36.—The lowest rotational energy levels of CH. Allowed far-infrared transitions within each ladder are shown with line strengths S and Einstein A coefficients (from Burdyuzha and Varshalovich 1973). Equivalent far-infrared wavelengths and rotation temperatures for excitation of the rotational levels are shown. The Λ doublet splittings (not to scale) of the excited states are based on $Y = 2$ and $q = 0.038$ cm^{-1}.

An interesting, and for CH probably very important fact, is that we have a "population transformer" in the $F_1(J)$ ladder, *viz.*, the $^2\Pi_{1/2}$, $J = 3/2$ state (which has the same parities as the ground state), as illustrated with line strengths and A coefficients in Figure 36 (unfortunately, the hyperfine splittings of this state are not well known; they can, however, be estimated from the configuration interaction that we have deduced from the observations of the ground-state transition frequencies).

Let us next assume that CH is excited in equal amounts in both ladders, at some level $N = 2$ or higher, and that there is no initial net inversion. Since $h\nu_\Lambda/k$ is a small number even at these levels, the relative population differences (degeneracies considered) are very small.

If we next follow the $F_1(J)$ ladder down to the (noninverted) $J = 3/2$ doublet, we note that its spontaneous emission to the ground state will tend to invert the latter, whereas the transfer from the $F_2(3/2)$ level will have the opposite effect. These effects may cancel out, but only a moderate initial overpopulation of the F_1 ladder may tend to produce a net inversion of the ground-state doublet. It is important, therefore, to note that it does not seem necessary to assume a net inversion of the initial (equally populated) N-states in order to obtain a slight inversion of the CH ground-state doublet. If we assume this to be the case, the net inversion is practically independent of the initial N-values, i.e., the mechanism will be about the same, as long as the kinetic energies of the colliding particles are of the order of 100 K. Actually, there would be an $N = 2$ level population that cannot be neglected, even if the translational energy of the colliding particle is smaller.

It is also of some importance to note that our proposed mechanism (which awaits confirmation by computer calculations of the total cascading process) would hold for CH formed in a rotationally excited state by some chemical reactions, or by evaporation from grains. Formation of roughly equal amounts of CH in the F_1 and F_2 ladders is to be expected even in such cases.

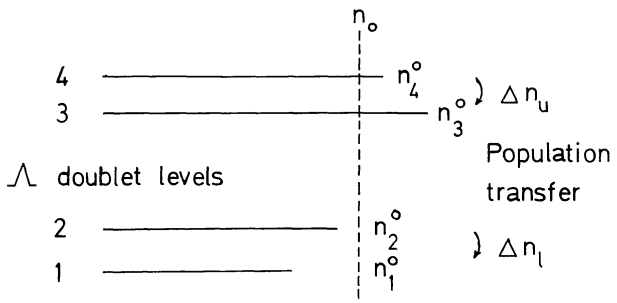

FIG. 37.—Initial, normalized populations of the ground state Λ doublet, indicated by length of horizontal lines. See discussion in the text.

Even if the initial excited states (at $N = 2$, 3, or higher) were quite strongly inverted, the presence of the "population transformer" would more or less destroy this effect at the ground-state doublet [if the initial $F_1(J)$ and $F_2(J)$ states are about equally populated]. This should explain why CH never has been observed to be a strong maser in its ground state. To verify this hypothesis it should be of great importance to detect the interstellar $J = 5/2$ transitions (at about 4.7 GHz; cf. Fig. 35) of the F_1 ladder. As a by-product, such a detection would yield a much-needed, more exact Y-value for the lowest rotational states of CH.

Next, let us come to the case of the possible negative doublet temperatures in dust clouds. Generally, a not inconsiderable fraction of the CH radicals will be found in the $F_1(3/2)$ state, and with a doublet temperature of, say, 5–10 K, more or less corresponding to the observed population of the OH ground state. As in the previous case, spontaneous emission to the ground state (in the time of about 30 minutes, which is extremely short compared with the radiative lifetimes within the ground state) would tend to invert the state, probably easily leading to the negative doublet temperatures estimated by us (see the previous section).

Whether it be in H I regions, or in dust clouds, the $F_1(3/2)$ "population transformer" may serve to explain the negative ground-state doublet temperatures (which it may maintain for a considerable time—10 years or more in H I regions, for example).

c) Far-Infrared Pumping

We have on many occasions in this paper suggested that the enhancement of the CH lower satellite line often found for clouds associated with H II regions is caused by the far-infrared radiation from heated dust. The correlation between the enhancement and the far-infrared radiation was already discussed in the excitation temperature discussion appearing in § III*b* and was illustrated in Table 3.

Figure 36 depicts the energy levels of the CH ground-state $^2\Pi_{1/2}$, $J = 1/2$ Λ doublet as well as some excited rotational states of the $^2\Pi_{1/2}$ and $^2\Pi_{3/2}$ ladders. In the latter doublets there are presumptive interlocking levels, causing far-infrared population transfers between the hyperfine levels $F = 1$–0 within each half of the ground state Λ doublet (cf. Litvak 1969, 1972). The connecting far-infrared transitions are indicated in the figure together with the line strengths and Einstein A coefficients taken from Burdyuzha and Varshalovich (1973). A population transfer in the direction $F = 1 \rightarrow 0$ is needed to account for the observed lower satellite enhancement. Such a transfer may occur since the line strengths are unequal and hence yield unequal trapping and unequal intensities for the interlocking transitions.

In order to estimate the effect of far-infrared population transfers between the hyperfine levels of the ground-state Λ doublet, we make use of the simplified presentation in Figure 37 of the normalized populations, $n_q = N_q/g_q$, where g_q is the degeneracy factor. To simplify matters further, we assume that the nuclear spin information is preserved in the absence of far-infrared population transfers (cf. § VII*b*), but that the two spin states ($F = J \pm 1/2$) have different inversions. With these assumptions we may write

$$\left.\begin{matrix} n_4^0 \\ n_2^0 \end{matrix}\right\} = n_0(1 \pm \Delta_1); \left.\begin{matrix} n_3^0 \\ n_1^0 \end{matrix}\right\} = n_0(1 \pm \Delta_2)\,. \tag{32}$$

If $\Delta_2 \approx 3\Delta_1$, and >0, this situation approximately corresponds to our results in the direction of the Orion and Perseus arm clouds (expressions for the line ratios and excitation temperatures in terms of Δ_1 and Δ_2 are given by Rydbeck *et al.* 1975). Since Δ_1 is a very small quantity in our case ($h\nu_\Lambda/k \approx 0.16$ K), we assume that the population transfer $\Delta n_{u,l}$ (see Fig. 37) is proportional to the mean populations, and write

$$\Delta n_u = n_0\left(1 + \frac{\Delta_1 + \Delta_2}{2}\right)\delta_u\,, \tag{33a}$$

and

$$\Delta n_l = n_0\left(1 - \frac{\Delta_1 + \Delta_2}{2}\right)\delta_l\,, \tag{33b}$$

i.e.,

$$\begin{aligned} n_4 &= n_0\left[1 + \Delta_1 - \delta_u\left(1 + \frac{\Delta_1 + \Delta_2}{2}\right)\right], \\ n_3 &= n_0\left[1 + \Delta_2 + \delta_u\left(1 + \frac{\Delta_1 + \Delta_2}{2}\right)\right], \\ n_2 &= n_0\left[1 - \Delta_1 - \delta_l\left(1 - \frac{\Delta_1 + \Delta_2}{2}\right)\right], \\ n_1 &= n_0\left[1 - \Delta_2 + \delta_l\left(1 - \frac{\Delta_1 + \Delta_2}{2}\right)\right]. \end{aligned} \tag{34}$$

Here δ_u and δ_l are determined by the coupled rate and radiative-transfer equations (Litvak 1969). For the present discussion it would serve no practical purpose to burden the presentation with complete expressions for δ_u and δ_l.

The population differences thus become

$$\begin{aligned} \Delta n_{42} &= n_4 - n_2 = n_0\left[2\Delta_1 - (\delta_u - \delta_l) - \frac{\delta_u + \delta_l}{2}(\Delta_1 + \Delta_2)\right] \quad \text{(the main line)}\,, \\ \Delta n_{41} &= n_4 - n_1 = n_0\left[\Delta_1 + \Delta_2 - (\delta_u + \delta_l) - \frac{\delta_u - \delta_l}{2}(\Delta_1 + \Delta_2)\right] \quad \text{(the upper satellite)}\,, \\ \Delta n_{32} &= n_3 - n_2 = n_0\left[\Delta_1 + \Delta_2 + \delta_u + \delta_l + \frac{\delta_u - \delta_l}{2}(\Delta_1 + \Delta_2)\right] \quad \text{(the lower satellite)}\,. \end{aligned} \tag{35}$$

Let us neglect second-order terms in relations (35) and assume, for the sake of an initial discussion, that $\Delta_2 = 3\Delta_1$. This yields

$$\begin{aligned} \Delta n_{42} &\approx n_0[2\Delta_1 - (\delta_u - \delta_l)]\,, \\ \Delta n_{41} &\approx n_0[4\Delta_1 - (\delta_u + \delta_l)]\,, \\ \Delta n_{32} &\approx n_0[4\Delta_1 + (\delta_u + \delta_l)]\,. \end{aligned} \tag{36}$$

If the two far-infrared transitions which connect the two lowest ground-state hyperfine levels (with a frequency difference of only 13.7 MHz) with a common excited level, for example $F_2(3/2)$ in Figure 36, overlap, this means that $\delta_l \approx 0$. The effect of such an overlap will be considered in the following discussion.

As appears from our previous sections on the various CH observations, the upper satellite line is rarely anomalously enhanced. It is therefore of interest to consider the case of zero population difference for the upper satellite, and see what happens to the main line and the lower satellite.

Case a $\delta_u = \delta_l$.—Relations (35) now yield to first order $\Delta n_{32} \approx n_0 2(\Delta_1 + \Delta_2)$; $\Delta n_{42} \approx n_0 2\Delta_1$; both main and lower satellite lines are weak masers.

If the ground-state doublet were not initially inverted ($\Delta_1, \Delta_2 < 0$), both the upper satellite and the main line would be seen in absorption, as appears from equation (35) (whenever we mention absorption, the background is tacitly assumed to be strong enough for this to appear). The lower satellite, however, would be masing if $(\delta_u + \delta_l) > |\Delta_1 + \Delta_2|$.

Case b $\delta_l = 0$ (*overlap of lower levels*).—We now obtain, again for a vanishing upper satellite population difference,

$$\Delta n_{32} \approx n_0 2(\Delta_1 + \Delta_2);\ \Delta n_{42} \approx n_0(\Delta_1 - \Delta_2)\,.$$

If the doublet is initially inverted ($\Delta_1, \Delta_2 > 0$), we notice the interesting circumstance that the main line is seen in absorption if $\Delta_2 > \Delta_1$ (for a strong background source). In the characteristic initial case $\Delta_2 \approx 3\Delta_1$ (eq. [36]), we thus obtain $\Delta n_{32} \approx n_0 8\Delta_1$, and $\Delta n_{42} \approx -n_0 2\Delta_1$. This agrees quite well (by relations [3] and [11]) with the result found by Gardner and Robinson (1974) toward the high-brightness H II regions RCW 38 and G327.3−0.5.

In order to continue the discussion, let us assume that the upper satellite line is seen in weak absorption. This will occur if $\delta_u = \Delta_1 + \Delta_2 + \zeta$ (where $0 < \zeta \ll 1$), where we still take $\delta_l = 0$. We obtain

$$\Delta n_{32} \approx n_0[2(\Delta_1 + \Delta_2) + \zeta];$$

$\Delta n_{41} \approx -n_0\zeta$; and $\Delta n_{42} \approx n_0(\Delta_1 - \Delta_2 - \zeta)$. If $\Delta_2 > (\Delta_1 - \zeta)$, the main line is also seen in absorption. This may correspond to the situation in that part of our M17 spectrum where both the upper satellite and the main line are observed in weak absorption. Clearly, the initial population (more precisely, the difference between Δ_1 and Δ_2) is most important in this context (i.e., when $\delta_l = 0$). Thus we can more or less explain any observed situation by a suitable choice of Δ_2 (provided that the far-infrared population transfer between the upper hyperfine levels of the doublet is large enough—which, of course, depends upon the strength of the infrared background radiation).

For an additional possibility, assume that there is no initial net inversion ($\Delta_1, \Delta_2 < 0$). For the lower satellite to be seen in maser emission, we must require that $\delta_u = |\Delta_1 + \Delta_2| + \zeta$ (if $\delta_l = 0$), which yields $\Delta n_{32} \approx n_0\zeta$; $\Delta n_{41} \approx -n_0(2|\Delta_1 + \Delta_2| + \zeta)$; and $\Delta n_{42} \approx -n_0(3|\Delta_1| + |\Delta_2| + \zeta)$. Thus when the lower satellite is a faint maser, the other lines are seen in strong absorption. No such situation has been observed by us.

With $\delta_l = 0$ and $\Delta_2 \gtrsim \Delta_1$ (both being positive), most CH spectra, seen against a strong far-infrared background, can be adequately explained to first order. Let us therefore see what the condition $\delta_l = 0$ implies. If we assume a half-power Doppler width of the ground state of about 1 km s^{-1}, and also assume that its far-infared connection is with the F_2 (3/2) state (which, according to Fig. 36 or Table 7, lies about 96 K [$\lambda_{rot} \approx 150\mu$] above the ground state), the far-infrared Doppler line width then would be about 7 MHz. This is approximately one-half of the hyperfine splitting of the ground state. Therefore, in view of the observed CH line widths, there is good reason to assume that $\delta_l \approx 0$, except perhaps in the cold dust clouds (see the previous section, for example).

VIII. ABUNDANCES AND FORMATION OF CH

The estimated column densities of CH are listed in Table 1 for H I clouds and clouds associated with H II regions, and in Table 5 for dark dust clouds. The assumptions and uncertainties inherent in the calculations were discussed in §§ III*b* and IV. We will now compare the CH densities with those of other species, and also comment upon existing theories of CH formation in relation to the observational data.

a) Comparison of Observed Abundances

In spite of the great uncertainties inherent in all column-density determinations, we have used the abundance information on CH, OH, H_2CO, CO, and H I given in Tables 1 and 5 to find possible similarities and differences in abundance ratios between (*a*) compact molecular clouds (observed in millimeter-wave molecular lines other than CO), associated with H II regions and far-infrared sources (e.g., M17, W43, W49, W51, K3–50, DR21, W3C1); (*b*) extended clouds (probably not contained in category *a*), associated with H II regions; (*c*) dark dust clouds; and (*d*) H I spiral arm clouds not associated with H II regions.

The spectral line and distance information in Table 2 was used to assign the different features of Table 1 into the categories *a*, *b*, or *d*. Although a definite classification is difficult in some cases, the result contained in Table 8, listing unweighted average values and ranges of variation of the abundance ratios, is very interesting. For the data taken from Table 1 we have assumed the excitation temperatures $T_{x,OH} = 5$ K (see paragraph on Cas A; cf. also W12 estimates by Manchester and Gordon 1971; Goss *et al.* 1975) and $T_{x,H_2CO} = 2$ K. The dust clouds L134 and L134N have not been included in the N_{CH}/N_{H_2CO} comparison, as the reported H_2CO column densities show such a large scatter (see Table 5).

We find a very interesting pattern in the abundance ratios between different kinds of regions. The compact molecular clouds have a characteristic abundance ratio $N_{CH}/N_{OH} \approx 0.06$, with a surprisingly small scatter. This ratio increases for the less dense regions, to about 0.4 for the H I clouds. Similarly we find that N_{CH}/N_{H_2CO} increases by an order of magnitude, from about 1 for the molecular clouds to about 10 for the H I clouds. Deviations of beam filling (ρ_{10}), clumping (R_0), and excitation temperatures for the three species to such an extent that the above abundance ratios for these two cloud categories overlap are believed to be highly improbable; cf. relation (7). For instance, an increased value of $T_{x,OH}$, which is quite probable for the molecular clouds (if the OH population

TABLE 8

ABUNDANCE RATIOS[a]

Cloud Type	N_{CH}/N_{OH}	N_{CH}/N_{H_2CO}	$10^6\ N_{CH}/N_{CO}$	$10^8\ N_{CH}/N_{HI}$
Compact molecular clouds	0.06	1	6	...
	(0.06–0.08)	(0.6–3)	(1–15)	...
Extended clouds associated with H II regions	0.2	3	18	3
	(0.03–0.5)	(0.7–5)	(8–30)	(1–6)
Dark dust clouds	0.2,[b] 0.4[c]	3,[b] 5[c]	≈ 100[d]	8,[b] 18,[c][3][e]
	(0.04–0.5),[b] (0.1–1)[c]	(1–6),[b] (3–11)[c]	...	(0.6–20),[b] (1–60)[c]
H I clouds	0.4	10	>70; >300[f]	4
	(0.1–0.9)	(4–23)	...	(2–7)

NOTES.—(a) The ranges of variation are given in parentheses below the unweighted average values. (b) Calculated with $T_{x_2CH} = -15$ K. (c) Calculated with $T_{x,CH} = T_{kin}$. (d) Order of magnitude, assuming $N_{CO} \approx 10^{18}$ cm^{-2} (Penzias *et al.* 1972). (e) Determined from the optical CH and H I data toward o Per, given in Table 5. (f) Cas A, Orion and Perseus arms, respectively.

distribution is mainly determined by thermalizing collisions), decreases N_{CH}/N_{OH} further. A more inverted CH main line (than that corresponding to $T_{x,CH} = -15$ K), as suggested earlier in § III*b*, also results in a decrease. The above deduced rough ratios $N_{CH}/N_{OH}/N_{H_2CO} \approx 1/2.5/0.1$ for the H I clouds agree well with those obtained toward Cas A for all the individual features of the Orion and Perseus arms (1/4/0.1).

The reason for the apparent CH deficiency in the molecular clouds may be that in such dense clouds this highly reactive radical is consumed by the formation of the more complex molecules observed (cf. also the CH results toward Sgr A; Gardner and Robinson 1974).

The N_{CH}/N_{CO} ratio shows a behavior similar to the N_{CH}/N_{OH} and N_{CH}/N_{H_2CO} ratios for different regions, but the increase from dense to thin regions may be somewhat greater, which would illustrate the underabundance of carbon monoxide in the less dense regions (^{12}CO has been detected in the Orion and Perseus arms toward Cas A, while only an upper limit has been obtained for ^{13}CO. This is not astonishing, since CO very probably is collisionally excited and needs high particle densities for its detection).

The dark dust clouds fit very well into this pattern, as their abundance ratios fall in between those of the very dense molecular clouds and the H I regions. This is true for both sets of values given in Table 8, i.e., whether the CH transitions are population-inverted or not. The extended clouds associated with H II regions assume abundance ratio values quite similar to those of the dark dust clouds, except that the N_{CH}/N_{CO} ratio may be somewhat lower.

The situation for the N_{CH}/N_{HI} ratio is not so clear, as the data are less complete for this case, and also because of the discrepancy between the radio and optical data for the dark dust clouds. The radio data may be uncertain due to differences in beam sizes for the CH and H I observations. If we use the optically determined value, which does not suffer from such effects, we find that $N_{CH}/N_{HI} \approx 3 \times 10^{-8}$ for all kinds of regions for which data are available. This probably reflects the fact that hydrogen appears more in molecular form with increasing density (Carruthers 1970; Hollenbach *et al.* 1971; de Jong 1972; Spitzer *et al.* 1973). Even so, the apparent constancy of this ratio must be accounted for when theories of CH formation are developed.

b) *Theories of* CH *Formation; Comparison with Observations*

Recent theories of interstellar CH formation include radiative association, inverse predissociation, ion-molecule reactions, and surface reactions on interstellar grains (e.g., Watson and Salpeter 1972; Solomon and Klemperer 1972; Julienne and Krauss 1973; Black and Dalgarno 1973; Herbst and Klemperer 1973; Aannestad 1973*a*, *b*; Watson 1974; Stecher and Williams 1974). A brief discussion of some of the more elaborate theories of molecule formation will be given here. The general lack of basic laboratory data is a serious drawback and introduces a speculative feature to the formation problem. However, it seems that formation of CH in interstellar H I clouds by diatomic processes alone can be ruled out, since the inverse predissociation process has been found to have insufficient rate (Julienne and Krauss 1973), while an abundance ratio $[CH]/[H] \approx 10^{-10}$ has been derived from radiative association (Smith, Liszt, and Lutz 1973; Brooks and Smith 1974). This value clearly falls short of our observed values given in Table 8 by several orders of magnitude.

The uncertainties in rate coefficients, e.g. for the associative reaction between C^+ and H_2 and for the dissociative recombination rate of CH^+ (Stecher and Williams 1974), which are crucial for the ion-molecule reaction schemes of Black and Dalgarno (1973) and Watson (1974), make it difficult to decide upon the significance of these theories. For instance, Watson predicts a ratio $[CH]/[H + 2H_2] \approx 5 \times 10^{-9}$ for clouds with $n_{H_2}/(n_H + 2n_{H_2}) \leqslant 0.1$ and $n_H + 2n_{H_2} \geqslant 10^2$ cm^{-3}. As the dissociative recombination rate of CH^+ may be underestimated (Stecher and Williams 1974), even this value may be too large, in which case the abundance ratios for H I regions observed by us cannot be explained by Watson's model.

The extensive ion-molecule reaction scheme presented by Herbst and Klemperer (1973) predicts $n_{CH} \approx 10^{-6}$ cm^{-3} for clouds with $n_{H_2} = 10^4$ cm^{-3}, typical for dark dust clouds (Heiles and Gordon 1973). If we take L134 as an example (radius $\approx$0.5 pc; Sancisi 1971), we observe $n_{CH} \approx 10^{-5}$ cm^{-3}, if we use the lowest column-density alternative (0.4×10^{14} cm^{-2}) in Table 5. Furthermore, the theory predicts $[CH]/[OH] \approx 10^{-2}$ and $[CH]/[H_2CO] \approx 10^{-1}$, while according to Table 8 we observe abundance ratios [CH]/[OH] between 0.04 and 0.5 and $[CH]/[H_2CO]$ between 1 and 6, with mean ratios of about 0.2 and 3, respectively. These values are based on the lowest CH column-density alternatives in Table 5, calculated with a negative excitation temperature. The disagreement becomes worse if CH is nonmasing in the dark dust clouds (see Table 8). Herbst and Klemperer's theory is also in disagreement with observations for the molecular clouds. For $n_{H_2} = 10^6$ cm^{-3}, typical for such clouds (Zuckerman and Palmer 1974), a value of about 10^{-3} is predicted for [CH]/[OH] and $[CH]/[H_2CO]$. From Table 8 we find the values $[CH]/[OH] \approx 0.06$ and $[CH]/[H_2CO] \approx 1$.

The calculations of Watson and Salpeter (1972), which include formation on grains and gas-phase reactions, predict abundance ratios $[CH]/[H] \approx 10^{-9}$ and $[CH]/[OH] \approx 5 \times 10^{-2}$ for "normal" H I clouds. These values are about one order of magnitude smaller than those observed (see Table 8). For these clouds the ξ factor of Watson and Salpeter, which is a measure of both gas density and shielding from ultraviolet radiation, is about unity. For the dark dust clouds ξ exceeds the value (10^4) for which the theory applies, but it is interesting, nonetheless, to see that for the most dense regions considered by Watson and Salpeter $[CH]/[CO] \approx 3 \times 10^{-4}$; for $N_{CO} = 10^{18}$ cm^{-2} (Penzias *et al.* 1972) we roughly get $[CH]/[CO] \approx 10^{-4}$ from our observations.

Aannestad (1973*a*, *b*) found, including both gas-phase reactions and catalytic surface reactions on interstellar grains, that the calculated CH column densities for H I clouds are sensitive to the degree of depletion of cooling elements (principally O, C^+, Fe^+, Si^+) on grains. The highest column densities were found for fairly young clouds with small depletion. His calculations are, however, hard pressed to account for the column densities of about 10^{14} cm^{-2} which we find for the H I clouds. Aannestad also interpreted typical H I clouds where OH has been found in absorption (cf. Davies and Matthews 1972) as "old" clouds where the depletion is relatively large. In his model the ratio [CH]/[OH] decreases by several orders of magnitude, depending on the increasing depletion of the cooling elements on the grains with time. The scatter in our observed [CH]/[OH] ratios (see Table 8) could then, apart from observational uncertainties, reflect different ages of the clouds.

We may say in conclusion that our observed CH column densities for the H I clouds might be marginally explained by the theories of interstellar CH formation that include gas-phase and surface reactions on interstellar grains. For the denser regions, and especially for the dense molecular clouds, no satisfactory theory of CH formation appears to have been developed.

IX. SUMMARY AND CONCLUSIONS

This paper contains the results of more than eight months of almost continuous, high-sensitivity, observations of the three hyperfine transitions in the $^2\Pi_{1/2}, J = 1/2$ state of CH. Detailed discussions of the CH spectra, including comparison with most available observational data on other species, are presented in source descriptions and tables. Radiative-transfer considerations and discussions of CH excitation mechanisms are also included. The following points may serve as a brief summary of our results:

1. CH is found to be widespread in the Galaxy (cf. Fig. 2). It has been observed in H I regions, in dark dust clouds, and both in extended areas around H II (and far-infrared) regions as well as in compact "molecular" clouds associated with them (cf. Tables 1–5).

2. The three CH transitions are observed in emission almost everywhere, and exhibit weak maser characteristics, probably even in the cold dark dust clouds. However, our observations are not entirely conclusive on this point for the latter objects.

3. From observations toward and around Cas A the CH main ($F = 1$–1) line excitation temperature in the Orion and Perseus arm H I clouds is estimated to be $-15(+10, -30)$ K. The error bounds are due to observational uncertainties ($\sim \pm 5$ K) and estimated cloud inhomogeneities. The satellite line excitation temperatures assume values between -12 and -6 K, for the various velocity features. This illustrates that the satellite transitions are more inverted than the main line, a situation *generally* found in our observations.

4. Similarly, the excitation temperature of the 1667 MHz ($F = 2$–2) OH ground-state transition was estimated to be about $+4$ K in the H I clouds toward Cas A.

5. Our Cas A observations reveal a conspicuous congruence in shape between the CH emission spectra and the Orion and Perseus arm absorption features of the 1_{11}–1_{10} H_2CO transition, as well as those of the ground-state OH main lines (cf. Fig. 3). This indicates that CH, OH, and H_2CO are "well mixed" in these—in detail unknown—spiral-arm cloud configurations. Such similarities in spectral shape appear for these species in many of our observations toward stronger background sources.

6. From observations toward and around W12 we estimate the CH main line excitation temperature in this "molecular" cloud to be about -10 K. However, the observed presence of large cloud inhomogeneities means that the uncertainty is considerable.

7. In view of the good agreement between the main line excitation temperatures of these two different cloud categories, we adopt -15 K as a reasonable value for *all* observed clouds. We can then calculate excitation temperatures for the satellite lines, optical depths, and, which is very important, CH column densities, in all observed directions (cf. Table 1). For the dark dust clouds we also present column densities under the assumption of LTE (Table 5).

8. The CH lower ($F = 0$–1) satellite transition seems to be a very sensitive far-infrared indicator. Striking examples of enhanced lower satellite features are found in the CH clouds associated with the H II complexes W3, W10, W12, M17, W43, W44, W49, W51, K3–50, and DR 21, which are also observed to be luminous far-infrared sources (cf. Table 3, and e.g., Figs. 15 and 17). Suitable far-infrared pumping schemes are proposed, which cause the necessary population transfer between the hyperfine levels ($F = 1 \rightarrow 0$) within each half of the CH ground-state Λ doublet. "Interlocking" levels in the nearest rotationally excited states are involved (cf. Fig. 36 and § VII). Far-infrared "overlap" of the lowest ground-state hyperfine levels seems to be important in this context.

9. We have observed CH in absorption, in the upper satellite and main lines, only toward the strong H II/IR source M17. The lower satellite transition still is an anomalously enhanced, weak maser feature. These results can also be explained by the proposed far-infrared pumping.

10. Our observations toward H I and H II regions indicate that it should be possible, with sufficient integration times, to map at least fractions of the galactic CH "spiral arm" structure.

11. Our CH dark dust cloud data originally appeared to exhibit LTE characteristics. The satellite-to-main line intensity ratios were all close to 1/2, within the observational uncertainties. However, this is to be expected also for the weak maser case, whenever the background radiation is faint. Finally, after long and careful integration,

a notable exception was found in the position G174.3−13.4 of Heiles's Cloud 2. Here the observed satellite-to-main line intensity ratios were greater than 1/2, and definitely different for the two satellite lines, which would exclude LTE.

12. Recent observations toward and around the extragalactic source 3C 123, which is behind Lynds's dark dust cloud L1500, seem to indicate that the CH gas, in all three transitions, weakly amplifies the background radiation. The main line excitation temperature in this dark cloud is estimated to be about −10 K, while the satellite transitions are somewhat more population-inverted. This result, which will be treated in a separate paper, is not entirely conclusive, however, since the observed 3C 123 background radiation is weak.

13. Another indication of CH weak maser behavior in a foreground cool (dust) cloud is found in our spectra toward the strong M17 continuum source. The CH emission feature at about +24 km s^{-1}, by far the narrowest that we have observed (width $\approx$0.3 km s^{-1}, i.e., a Doppler temperature $\lesssim$30 K), even including the dark dust clouds, probably arises from amplification of the background radiation.

14. We have theoretically considered possible methods of determination of excitation temperatures and optical depths for cases where no on/off background source observations are available. Applications are found in the most reliable dark dust cloud spectra (see § VI).

15. By means of the observed transition frequencies in the CH $^2\Pi_{1/2}$, $J = 1/2$ ground state, we have (in § VII) estimated the Λ doublet frequencies of rotationally excited CH states in the $^2\Pi_{1/2}$ and $^2\Pi_{3/2}$ ladders (see Table 7, and Fig. 35, where parities are also entered).

16. The problem of CH excitation is considered in § VII. We suggest that the nearest rotationally excited state ($^2\Pi_{1/2}$, $J = 3/2$), only 26 K above the ground state, may serve as a "population transformer," since the parities of these two states appear to be the same (cf. Fig. 36). This may also explain the possible negative excitation temperatures in the dark dust clouds.

17. The abundance information on CH, OH, H_2CO, CO, and H I (contained in Tables 1 and 5) seems to be very interesting from an "astrochemical" point of view. In spite of all inherent uncertainties, we find a very systematic behavior of the abundance ratios (cf. Table 8). In average we obtain [CH]/[OH] $\approx$ 0.06 for the compact "molecular" clouds, and 0.4 for the dilute H I clouds, while [CH]/[H_2CO] $\approx$ 1 and 10, respectively. The dark dust cloud abundance ratios fit in between these values. A similar behavior is obtained for [CH]/[CO], which changes from about 6×10^{-6} to greater than about 10^{-4}. The reason for the apparent CH deficiency in the densest clouds may be that this highly reactive radical is consumed by the formation of the observed, more complex molecules. The ratio [CH]/[H I] $\approx 3 \times 10^{-8}$ does not seem to vary much. This probably reflects the (observed) fact that hydrogen appears more in molecular form with increasing density.

18. The estimated CH column densities fall in the range 10^{13} to 3×10^{14} cm^{-2}, and seem to be large compared with those predicted by current theories of interstellar molecule formation. Also, the observed and theoretically deduced abundance ratios of CH to other molecular species appear to disagree considerably. We hope that our results concerning this "missing link" of interstellar organic chemistry—observed in dilute H I regions, as well as in denser dark dust clouds and compact "molecular" clouds—will further stimulate astrochemists in their efforts.

19. We have been able to compare optical and radio CH observations in one case, *viz.* toward the open cluster IC 348 (G160.5−17.8), which is only 6′ away from the star o Per, in the extended Per OB 2 dust cloud. Our radio estimated CH column density is of the order of 10^{14} cm^{-2}, while the optically determined value is about 2×10^{13} cm^{-2}. This indicates that the dust cloud is mainly located behind o Per, in agreement with other optical data.

20. Negative results are presented in Table 6. We have not detected CH toward OH/IR stars, or in the direction of stars where CH has been detected optically in absorption in foreground H I clouds. Obviously these observations should be repeated with considerably increased integration times.

X. RECENT OBSERVATIONS

After the observations described in the present paper were completed, we performed a CH survey at Onsala (1974 October–1975 March) including more than one hundred positions, mainly of dust cloud–type regions. This survey embraced Lynds's clouds, Barnard objects, clouds in front of extragalactic objects (3C 123, 3C 353), as well as clouds associated with nebulosity (NGC 2264) and far-infrared radiation (L1641). The results toward L1500 (3C 123) have been discussed somewhat in the present paper. More details about this and the other observed regions will be published in a separate paper (Hjalmarson *et al.* 1975).

A limited survey for CH has also recently been reported by Zuckerman and Turner (1975). There is general agreement with our results for those sources for which a detection was possible with their equipment.

We would like to thank Dr. R. D. Davies for providing us with OH and H_2CO spectra toward Cas A, Drs. J. R. Dickel, C. Heiles, and B. J. Robinson for sending us data prior to publication, Dr. H. J. Wendker for supplying a continuum map of the Cyg X region, Mr. C.-O. Lindström of our Quantum Electronics Group for valuable technical assistance, Mr. L. E. B. Johansson and C. Andersson for help with the observations, and an anonymous referee for helpful suggestions. W. I. gratefully acknowledges the hospitality of Professor O. E. H. Rydbeck and the staff at the Onsala Space Observatory during the period 1973 September to 1974 July.

The Onsala Space Observatory is operated by the Research Laboratory of Electronics, Chalmers University of Technology, Gothenburg, Sweden. This research was partly supported by the Swedish Natural Science Research Council, and by the Swedish Board for Technical Development.

REFERENCES

Aannestad, P. A. 1973*a*, *Ap. J. Suppl.*, **25**, 205.
———. 1973*b*, in *Molecules in the Galactic Environment*, ed. M. A. Gordon and L. E. Snyder (New York: Wiley-Interscience), p. 409.
Ackermann, G. 1970, *Astr. and Ap.*, **8**, 315.
Andersson, C., Johansson, L. E. B., Goss, W. M., Winnberg, A., and Nguyen-Quang-Rieu. 1974, *Astr. and Ap.*, **30**, 475.
Balick, B. 1972, *Ap. J.*, **176**, 353.
Balick, B., Gammon, R. H., and Doherty, L. H. 1974, *Ap. J.*, **188**, 45.
Barrett, A. H., Meeks, M. L., and Weinreb, S. 1964, *Nature*, **202**, 475.
Baudry, A. 1974, *Astr. and Ap.*, **33**, 381.
Becklin, E. E., Neugebauer, G., and Wynn-Wiliams, C. G. 1973, *Ap. Letters*, **13**, 147.
Berkhuijsen, E. M. 1972, *Astr. and Ap. Suppl.*, **5**, 263.
Blaauw, A. 1952, *Bull. Astr. Inst. Netherlands*, **11**, 405.
Black, J. H., Chaisson, E. J., Ball, J. A., Penfield, H., and Lilley, A. E. 1974, *Ap. J. (Letters)*, **191**, L45.
Black, J. H., and Dalgarno, A. 1973, *Ap. Letters*, **15**, 79.
Botterud, I., Lofthus, A., and Veseth, L. 1973, *Phys. Scripta*, **8**, 218.
Bridle, A. H., and Kesteven, M. J. L. 1970, *A.J.*, **75**, 902.
Brooks, N. H., and Smith, W. H. 1974, *Ap. J.*, **194**, 513.
Brown, R. L., Knapp, G. R., Kuiper, T. B. H., and Kuiper, E. N. R. 1975, *Ap. J. (Letters)*, **195**, L23.
Buhl, D., and Snyder, L. E. 1970, *Nature*, **228**, 267.
———. 1973, *Ap. J.*, **180**, 791.
Buhl, D., Snyder, L. E., Lovas, F. J., and Johnson, D. R. 1974, *Ap. J. (Letters)*, **192**, L97.
Burdyuzha, V. V., and Varshalovich, D. A. 1973, *Soviet Astr.—AJ*, **16**, 980.
Caroff, L. J., Petrosian, V., Salpeter, E. E., Wagoner, R. V., and Werner, M. W. 1973, *M.N.R.A.S.*, **164**, 295.
Carruthers, G. R. 1970, *Ap. J. (Letters)*, **161**, L81.
Caswell, J. L., and Goss, W. M. 1974, *Astr. and Ap.*, **32**, 209.
Cato, T., Elldér, J., Höglund, B., Rydbeck, O. E. H., Rönnäng, B., and Sume, A. 1972, *Astr. and Ap.*, **21**, 435.
Cato, B. T., Rönnäng, B. O., Lewin, P. T., Rydbeck, O. E. H., Yngvesson, K. S., Cardiasmenos, A. G., Shanley, J. F. 1975, Res. Rept. No. 123, Res. Lab. of Electronics, Chalmers University of Technology, Gothenburg.
Chaffee, F. H. 1974, *Ap. J.*, **189**, 427.
Chaisson, E. J. 1974, *A.J.*, **79**, 555.
Chaisson, E. J., and Ball, J. A. 1971, *Ap. J.*, **169**, 495.
Chaisson, E. J., and Goad, L. E. 1972, *Ap. J. (Letters)*, **171**, L61.
Cheung, A. C., Chui, M. F., Matsakis, D., Townes, C. H., and Yngvesson, K. S. 1973, *Ap. J. (Letters)*, **186**, L73.
Chui, M. F., Cheung, A. C., Matsakis, D., Townes, C. H., and Cardiasmenos, A. G. 1974, *Ap. J. (Letters)*, **187**, L19.
Clark, B. G. 1965, *Ap. J.*, **142**, 1398.
Clark, F. O., and Johnson, D. R. 1974, *Ap. J. (Letters)*, **191**, L87.
Cohen, J. G. 1973, *Ap. J.*, **186**, 149.
Crutcher, R. M. 1973, *Ap. J.*, **185**, 857.
Cudaback, D. D., and Heiles, C. 1969, *Ap. J. (Letters)*, **155**, L21.
Davies, R. D. 1973, in *IAU Symposium No. 52, Interstellar Dust and Related Topics*, ed. J. M. Greenberg and H. C. van de Hulst (Dordrecht: Reidel), p. 251.
Davies, R. D., and Matthews, H. E. 1972, *M.N.R.A.S.*, **156**, 253.
de Jong, T. 1972, *Astr. and Ap.*, **20**, 263.
Dickel, H. R. 1968, *Ap. J.*, **152**, 651.
Dickel, H. R., Dickel, J. R., Wilson, W. J., and Epstein, E. E. 1974, *Bull. AAS*, **6**, 221.
Dickel, H. R., Wendker, H., and Bieritz, J. H. 1969, *Astr. and Ap.*, **1**, 270.
Dickel, H. R., Wendker, H., and Bieritz, J. H. 1970, in *IAU Symposium No. 38, The Spiral Structure of Our Galaxy*, ed. W. Becker and G. Contopoulos (Dordrecht: Reidel), p. 213.
Dickel, J. R., and Milne, D. K. 1972, *Australian J. Phys.*, **25**, 539.
Dickinson, D. F. 1972, *Ap. J. (Letters)*, **175**, L43.
Dickinson, D. F., Bechis, K. P., and Barrett, A. H. 1973, *Ap. J.*, **180**, 831.
Dickinson, D. F., Kojoian, G., and Strom, S. E. 1974, *Ap. J. (Letters)*, **194**, L93.
Dieke, G. H., and Crosswhite, R. M. 1948, Bumblebee Rept. No. 87, Johns Hopkins University.
Dieter, N. H. 1973, *Ap. J.*, **183**, 449.
Douglas, A. E., and Elliott, G. A. 1965, *Canadian J. Phys.*, **43**, 496.
Dousmanis, G. C., Sanders, T. M., and Townes, C. H. 1955, *Phys. Rev.*, **100**, 1735.
Downes, D. 1970, *Ap. Letters*, **5**, 53.
Downes, D., and Rinehart, R. 1966, *Ap. J.*, **144**, 937.
Downes, D., and Wilson, T. L. 1974*a*, *Ap. J. (Letters)*, **191**, L77.
———. 1974*b*, *Astr. and Ap.*, **34**, 133.
Elldér, J., Rönnäng, B., and Winnberg, A. 1969, *Nature*, **222**, 67.
Elldér, J., Rydbeck, O. E. H., and Sume, A. 1973, Res. Rept. No. 117, Res. Lab. of Electronics, Chalmers University of Technology, Gothenburg.
Emerson, J. P., Jennings, R. E., and Moorwood, F. M. 1973, *Ap. J.*, **184**, 401.
Erickson, E. F., Swift, C. D., Witteborn, F. C., Mord, A. J., Augason, G. C., Caroff, L. J., Kunz, L. W., and Giver, L. P. 1973, *Ap. J.*, **183**, 535.
Evans, N. J., Cheung, A. C., and Sloanaker, R. M. 1970, *Ap. J. (Letters)*, **159**, L9.
Evans, N. J., Zuckerman, B., Morris, G., and Sato, T. 1975, *Ap. J.*, **196**, 433.
Evenson, K. M., Radford, H. E., and Moran, M. M. 1971, *Appl. Phys. Letters*, **18**, 426.
Fazio, G. G., Kleinmann, D. E., Noyes, R. W., Wright, E. L., and Zeilik, M. 1974, *Ap. J. (Letters)*, **192**, L23.
Fomalont, E. B., and Weliachew, L. 1973, *Ap. J.*, **181**, 781.
Fourikis, N., Takagi, K., and Morimoto, M. 1974, *Ap. J. (Letters)*, **191**, L139.
Frisch, P. 1972, *Ap. J.*, **173**, 301.
Gardner, F. F., and McGee, R. X. 1971, *Ap. Letters*, **8**, 83.
Gardner, F. F., and Robinson, B. J. 1974, *Proc. Astr. Soc. Australia*, **2**, 253.
Gardner, F. F., and Whiteoak, J. B. 1974, *Nature*, **247**, 526.
Gatley, I., Becklin, E. E., Matthews, K., Neugebauer, G., Penston, M. V., and Scoville, N. 1974, *Ap. J. (Letters)*, **191**, L121.
Geballe, T. R., Wollman, E. R., and Rank, D. M. 1973, *Ap. J.*, **183**, 499.
Gezari, D. Y., Joyce, R. R., Righini, G., Simon, M. 1974, *Ap. J. (Letters)*, **191**, L33.
Goss, W. M. 1968, *Ap. J. Suppl.*, **15**, 131.
Goss, W. M., Johansson, L. E. B., Elldér, J., Höglund, B., Nguyen-Quang-Rieu, and Winnberg, A. 1973, *Astr. and Ap.*, **28**, 89.
Goss, W. M., and Shaver, P. A. 1970, *Australian J. Phys., Ap. Suppl.*, No. 14, 1.
Goss, W. M., Winnberg, A., Johansson, L. E. B., and Fournier, A. 1975, preprint.
Gottesman, S. T., Davies, R. D., and Reddish, V. C. 1966, *M.N.R.A.S.*, **133**, 359.
Gottlieb, C. A., and Ball, J. A. 1973, *Ap. J. (Letters)*, **184**, L59.
Grasdalen, G. L. 1974, *Ap. J.*, **193**, 373.
Greisen, E. W. 1973*a*, *Ap. J.*, **184**, 363.
———. 1973*b*, *ibid.*, p. 379.

Gull, T. R., and Balick, B. 1974, *Ap. J.*, **192**, 63.
Gwinn, W. D., Turner, B. E., Goss, W. M., Blackman, G. L. 1973, *Ap. J.*, **179**, 789.
Habing, H. J., Goss, W. M., Matthews, H. E., and Winnberg, A. 1974, *Astr. and Ap.*, **35**, 1.
Habing, H. J., Israel, F. P., and de Jong, T. 1972, *Astr. and Ap.*, **17**, 329.
Hammersley, R. E., and Richards, W. G. 1974, *Nature*, **251**, 597.
Hardebeck, E. G. 1971, *Ap. J.*, **170**, 281.
———. 1972, *ibid.*, **172**, 583.
Hardebeck, E. G., and Wilson, W. J. 1971, *Ap. J.* (*Letters*), **169**, L123.
Harper, D. A. 1974, *Ap. J.*, **192**, 557.
Harper, D. A., and Low, F. J. 1971, *Ap. J.* (*Letters*), **165**, L9.
Harris, S. 1973, *M.N.R.A.S.*, **162**, 5P.
———. 1974, *ibid.*, **166**, 29P.
———. 1975, *ibid.*, **170**, 139.
Harvey, P. M., Gatley, I., Werner, M. W., Elias, J. H., Evans, N. J., Zuckerman, B., Morris, G., Sato, T., and Litvak, M. M. 1974, *Ap. J.* (*Letters*), **189**, L87.
Heiles, C. 1968, *Ap. J.*, **151**, 919.
———. 1969, *ibid.*, **157**, 123.
———. 1970, *ibid.*, **160**, 51.
———. 1973, *ibid.*, **183**, 441.
Heiles, C., and Gordon, M. A. 1973, in *IAU Symposium No. 52, Interstellar Dust and Related Topics*, ed. J. M. Greenberg and H. C. van de Hulst (Dordrecht: Reidel), p. 375.
———. 1974, preprint.
Herbig, G. H. 1968, *Zs. f. Ap.*, **68**, 243.
Herbst, E., and Klemperer, W. 1973, *Ap. J.*, **185**, 505.
Herzberg, G., and Johns, J. W. C. 1969, *Ap. J.*, **158**, 399.
———. 1971, *J. Chem. Phys.*, **54**, 2276.
Higgs, L. A. 1970, *Ap. Letters*, **6**, 11.
Hill, E., and Van Vleck, J. H. 1928, *Phys. Rev.*, **32**, 250.
Hippelein, H. H. 1973, *Astr. and Ap.*, **25**, 59.
Hjalmarson, Å., Sume, A., Elldér, J., Rydbeck, O. E. H., Moore, E., Huguenin, R., Sandqvist, A. A., Lindblad, P. O., and Lindroos, P. 1975, Res. Rept. No. 124, Res. Lab. of Electronics, Chalmers University of Technology, Gothenburg.
Hoffmann, W. F., Frederick, C. L., and Emery, R. J. 1971, *Ap. J.* (*Letters*), **170**, L89.
Höglund, B., and Andersson, C. 1974, *Astr. and Ap.*, **33**, 389.
Hollenbach, D. J., Werner, M. W., and Salpeter, E. E. 1971, *Ap. J.*, **163**, 165.
Hyland, A. R., Becklin, E. E., Frogel, J. A., and Neugebauer, G. 1972, *Astr. and Ap.*, **16**, 204.
Israel, F. P., Habing, H. J., and de Jong, T. 1973, *Astr. and Ap.*, **27**, 143.
Jefferts, K. B., Penzias, A. A., and Wilson, R. W. 1970, *Ap. J.* (*Letters*), **161**, L87.
Jenkins, E. B., Drake, J. F., Morton, D. C., Rogerson, J. B., Spitzer, L., and York, D. G. 1973, *Ap. J.* (*Letters*), **181**, L122.
Jenkins, E. B., and Savage, B. D. 1974, *Ap. J.*, **187**, 243.
Jennings, R. E. 1973, *Pub. Roy. Obs. Edinburgh*, **9**, 36.
Johansson, L. E. B., Höglund, B., Winnberg, A., Nguyen-Quang-Rieu, and Goss, W. M. 1974, *Ap. J.*, **189**, 455.
Johnson, H. M. 1973, *Ap. J.*, **182**, 497.
Johnston, K. J., Sloanaker, R. M., and Bologna, J. M. 1973, *Ap. J.*, **182**, 67.
Julienne, P. S., and Krauss, M. 1973, in *Molecules in the Galactic Environment*, ed. M. A. Gordon and L. E. Snyder (New York: Wiley-Interscience), p. 353.
Kaifu, N., Morimoto, M., Nagane, K., Akabane, K., Iguchi, T., and Takagi, K. 1974, *Ap. J.* (*Letters*), **191**, L135.
Kap-herr, A. v., and Wendker, H. J. 1972, *Astr. and Ap.*, **20**, 313.
Knapp, G. R. 1974, *A.J.*, **79**, 527.
Knowles, S. H., Mayer, C. H., Cheung, A. C., Rank, D. M., and Townes, C. H. 1969, *Science*, **163**, 1055.
Kollberg, E. L. 1973, *Proc. I.E.E.E.*, **61**, 1323.
Kutner, M., and Thaddeus, P. 1971, *Ap. J.* (*Letters*), **168**, L67.
Kutner, M., Thaddeus, P., Jefferts, K. B., Penzias, A. A., and Wilson, R. W. 1971, *Ap. J.* (*Letters*), **164**, L49.
Kutner, M. L., Thaddeus, P., Penzias, A. A., Wilson, R. W., and Jefferts, K. B. 1973, *Ap. J.* (*Letters*), **183**, L27.
Lada, C., and Chaisson, E. J. 1975, *Ap. J.*, **195**, 367.
Lada, C., Dickinson, D. F., and Penfield, H. 1974*a*, *Ap. J.* (*Letters*), **189**, L35.
Lada, C. J., Gottlieb, C. A., Litvak, M. M., and Lilley, A. E. 1974*b*, *Ap. J.*, **194**, 609.
Lauqué, R., Lequeux, J., and Nguyen-Quang-Rieu. 1973, *Nature Phys. Sci.*, **241**, 94.
Lemke, D., and Low, F. J. 1972, *Ap. J.* (*Letters*), **177**, L53.
Levy, D. H., and Hinze, J. 1975, *Ap. J.*, **200**, 236.
Linke, R. A., and Wannier, P. G. 1974, *Ap. J.* (*Letters*), **193**, L41.
Liszt, H. S., Wilson, R. W., Penzias, A. A., Jefferts, K. B., Wannier, P. G., and Solomon, P. M. 1974, *Ap. J.*, **190**, 557.
Litvak, M. M. 1969, *Ap. J.*, **156**, 471.
———. 1972, in *Atoms and Molecules in Astrophysics*, ed. T. R. Carson and M. J. Roberts (London: Academic Press), p. 201.
Lozinskaya, T. A. 1974, *Soviet Astr.—AJ*, **17**, 603.
Lynds, B. T. 1962, *Ap. J. Suppl.*, **7**, 1
———. 1968, in *Nebulae and Interstellar Matter, Stars and Stellar Systems*, Vol. **7**, ed. B. M. Middlehurst and L. H. Aller (Chicago: University of Chicago Press), p. 119.
MacLeod, J. M., and Doherty, L. H. 1968, *Ap. J.*, **154**, 833.
Manchester, R. N., and Gordon, M. A. 1971, *Ap. J.*, **169**, 507.
Manchester, R. N., Robinson, B. J., and Goss, W. M. 1970, *Australian J. Phys.*, **23**, 751.
Martin, A. H. M. 1972, *M.N.R.A.S.*, **157**, 31.
———. 1973, *ibid.*, **163**, 141.
Masheder, M. R. W., Booth, R. S., and Davies, R. D. 1974, *M.N.R.A.S.*, **166**, 561.
Matthews, H. E., Goss, W. M., Winnberg, A., and Habing, H. J. 1973, *Astr. and Ap.*, **29**, 309.
Mayer, C. H., Waak, J. A., Cheung, A. C., and Chui, M. F. 1973, *Ap. J.* (*Letters*), **182**, L65.
McCutcheon, W. H., and Shuter, W. L. H. 1970, *A.J.*, **75**, 910.
McGee, R. X., and Gardner, F. F. 1968, *Australian J. Phys.*, **21**, 149.
McGee, R. X., Gardner, F. F., and Robinson, B. J. 1967, *Australian J. Phys.*, **20**, 407.
Menon, T. K. 1970, *Ap. Letters*, **7**, 55.
Mezger, P. G. 1970, in *IAU Symposium No. 39, Interstellar Gas Dynamics*, ed. H. J. Habing (Dordrecht: Reidel), p. 336.
Mezger, P. G., Altenhoff, W., Schraml, J., Burke, B. F., Reifenstein, E. C., and Wilson, T. L. 1967, *Ap. J.* (*Letters*), **150**, L157.
Miller, F. D. 1937, *Ann. Harvard Coll. Obs.*, **105**, 297.
Milman, A. S. 1974, *Ap. J.* (*Letters*), **193**, L93.
Milne, D. K. 1970, *Australian J. Phys.*, **23**, 425.
Milne, D. K., and Hill, E. R. 1969, *Australian J. Phys.*, **22**, 211.
Milne, D. K., and Wilson, T. L. 1971, *Astr. and Ap.*, **10**, 220.
Minkowski, R. 1968, in *Nebulae and Interstellar Matter*, ed. B. M. Middlehurst and L. H. Aller (Chicago: University of Chicago Press), p. 623.
Minn, Y. K., and Greenberg, J. M. 1973*a*, *Astr. and Ap.*, **22**, 13.
———. 1973*b*, *Ap. Letters*, **13**, 39.
———. 1975, *Ap. J.*, **196**, 161.
Morris, M., Palmer, P., Turner, B. E., and Zuckerman, B. 1973*a*, in *IAU Symposium No. 52, Interstellar Dust and Related Topics*, ed. J. M. Greenberg and H. C. van de Hulst (Dordrecht: Reidel), p. 381.
———. 1974*a*, *Ap. J.*, **191**, 349.
Morris, M., Zuckerman, B., Palmer, P., and Turner, B. E. 1973*b*, *Ap. J.*, **186**, 501.
Morris, M., Zuckerman, B., Turner, B. E., and Palmer, P. 1974*b*, *Ap. J.* (*Letters*), **192**, L27.
Mulliken, R. S., and Christy, A. 1931, *Phys. Rev.*, **38**, 87.
Münch, G. 1964, *Ap. J.*, **140**, 107.
Neckel, T. 1966, *Zs. f. Ap.*, **63**, 221.
Neugebauer, G., Becklin, E., and Hyland, A. R. 1971, *Ann. Rev. Astr. and Ap.*, **9**, 67.
Neugebauer, G., and Garmire, G. 1970, *Ap. J.* (*Letters*), **161**, L91.
Olthof, H. 1974, *Astr. and Ap.*, **33**, 471.

Palmer, P., Zuckerman, B., Buhl, D., and Snyder, L. E. 1969, *Ap. J.* (*Letters*), **156**, L147.
Panagia, N. 1974, *Ap. J.*, **192**, 221.
Pankonin, V., Parrish, A., and Terzian, Y. 1973, *Ap. J.* (*Letters*), **180**, L113.
Parrish, A., Pankonin, V., Heiles, C. E., Rankin, J. M., and Terzian, Y. 1972, *Ap. J.*, **178**, 673.
Pashchenko, M. I. 1974, *Soviet Astr.—AJ*, **17**, 438.
Pastchenko, M. I., and Slysh, V. I. 1973, *Astr. and Ap.*, **26**, 349.
———. 1974, *ibid.*, **35**, 153.
Pedlar, A., and Hart, L. 1974, *M.N.R.A.S.*, **168**, 577.
Pedlar, A., and Matthews, H. E. 1973, *M.N.R.A.S.*, **165**, 381.
Penzias, A. A., Solomon, P. M., Jefferts, K. B., and Wilson, R. W. 1972, *Ap. J.* (*Letters*), **174**, L43.
Penzias, A. A., Wilson, R. W., and Jefferts, K. B. 1974, *Phys. Rev. Letters*, **32**, 701.
Persson, S. E., and Frogel, J. A. 1974, *Ap. J.*, **188**, 523.
Phillips, T. G., Jefferts, K. B., Wannier, P. G., and Ade, P. A. R. 1974, *Ap. J.* (*Letters*), **191**, L31.
Pike, E. M., and Drake, F. D. 1964, *Ap. J.*, **139**, 545.
Pipher, J. H., Grasdalen, G. L., and Soifer, B. T. 1974, *Ap. J.*, **193**, 283.
Pottasch, S. R. 1974, *Astr. and Ap.*, **30**, 371.
Radhakrishnan, V., Brooks, J. W., Goss, W. M., Murray, J. D., and Schwarz, U. J. 1972*a*, *Ap. J. Suppl.*, **24**, 1.
Radhakrishnan, V., Goss, W. M., Murray, J. D., and Brooks, J. W. 1972*b*, *Ap. J. Suppl.*, **24**, 49.
Reifenstein, E. C., Wilson, T. L., Burke, B. F., Mezger, P. G., and Altenhoff, W. J. 1970, *Astr. and Ap.*, **4**, 357.
Rickard, L. J., Zuckerman, B., and Palmer, P. 1972, *Bull. AAS*, **4**, 307.
———. 1973, *ibid.*, **5**, 331.
Rieke, G. H., Harper, D. A., Low, F. J., and Armstrong, K. R. 1973, *Ap. J.* (*Letters*), **183**, L67.
Robinson, B. J. 1967, in *IAU Symposium No. 31, Radio Astronomy and the Galactic System*, ed. H. van Woerden (London: Academic Press), p. 49.
Robinson, B. J., Gardner, F. F., Sinclair, M. W., and Whiteoak, J. B. 1974, *Nature*, **248**, 31.
Robinson, B. J., Goss, W. M., and Manchester, R. N. 1970, *Australian J. Phys.*, **23**, 363.
Rogers, A. E. E., and Barrett, A. H. 1967, in *IAU Symposium No. 31, Radio Astronomy and the Galactic System*, ed. H. van Woerden (London: Academic Press), p. 77.
Rosenberg, I. 1970*a*, *M.N.R.A.S.*, **147**, 215.
———. 1970*b*, *ibid.*, **151**, 109.
Rubin, R. H., and Turner, B. E. 1969, *Ap. J.* (*Letters*), **157**, L41.
———. 1971, *Ap. J.*, **165**, 471.
Rydbeck, O. E. H. 1974, *Abhandlungen der Matematisch-Naturwissenschaftlichen Klasse*, No. 1 (Mainz: Akademie der Wissenschaften und der Literatur).
Rydbeck, O. E. H., Elldér, J., and Irvine, W. M. 1973*a*, *Nature*, **246**, 466.
———. 1974, *Bull. AAS*, **6**, 221.
Rydbeck, O. E. H., Elldér, J., Irvine, W. M., Rönnäng, B., Godfrey, P. D., Fourikis, N., and Sinclair, M. W. 1974*a*, *Icarus*, **23**, 595.
Rydbeck, O. E. H., Elldér, J., Irvine, W. M., Sume, A., and Hjalmarson, Å. 1974*b*, *Astr. and Ap.*, **33**, 315.
———. 1974*c*, *ibid.*, **34**, 479.
Rydbeck, O. E. H., Elldér, J., and Kollberg, E. 1969, *Ap. J.* (*Letters*), **156**, L141.
Rydbeck, O. E. H., Elldér, J., Kollberg, E., and Höglund, B. 1972, *Mém. Soc. Roy. Sci. Liège*, 6th Ser., **3**, 507.
Rydbeck, O. E. H., Elldér, J., and Yngvesson, K. S. 1973*b*, Rept. No. P15, Dept. of Electrical and Computer Engineering, University of Mass., Amherst.
Rydbeck, O. E. H., and Kollberg, E. 1968, *I.E.E.E. Trans. Microwave Theory and Techniques*, MTT-16, 799.
Rydbeck, O. E. H., Kollberg, E., and Elldér, J. 1970, *Ap. J.* (*Letters*), **161**, L25.
Rydbeck, O. E. H., Kollberg, E., Hjalmarson, Å., Sume, A., Elldér, J., and Irvine, W. M. 1975, Res. Rept. No. 120, Res. Lab. of Electronics, Chalmers University of Technology, Gothenburg.
Sancisi, R. 1971, *Astr. and Ap.*, **12**, 323.
Sancisi, R., Goss, W. M., Andersson, C., Johansson, L. E. B., and Winnberg, A. 1974, *Astr. and Ap.*, **35**, 445.
Sato, F. 1968, *Pub. Astr. Soc. Japan*, **20**, 303.
———. 1973, *ibid.*, **25**, 135.
Sato, F., and Akabane, K. 1974, *Ann. Tokyo Astr. Obs.*, 2nd Ser., **14**, 120.
Schmidt, M. 1965, in *Galactic Structure, Stars and Stellars Systems*, Vol. **5**, ed. A. Blaauw and M. Schmidt (Chicago: University of Chicago Press), p. 513.
Schraml, J., and Mezger, P. G. 1969, *Ap. J.*, **156**, 269.
Schwartz, P. R., Wilson, W. J., and Epstein, E. E. 1973, *Ap. J.*, **186**, 529.
Scoville, N. Z., and Solomon, P. M. 1973, *Ap. J.*, **180**, 31.
Seeger, C. L., Westerhout, G., Conway, R. G., and Hoekema, T. 1965, *Bull. Astr. Inst. Netherlands*, **18**, 11.
Shaver, P. A. 1969, *M.N.R.A.S.*, **142**, 273.
Shaver, P. A., and Goss, W. M. 1970, *Australian J. Phys., Ap. Suppl.*, No. 14, 133.
Slysh, V. I. 1975, *Soviet Astr.—AJ*, **18**, 278, 405.
Smith, W. H., Liszt, H. S., and Lutz, B. L. 1973, *Ap. J.*, **183**, 69.
Snyder, L. E., and Buhl, D. 1971, *Ap. J.* (*Letters*), **163**, L47.
———. 1972*a*, *Ap. J.*, **177**, 619.
———. 1972*b*, *Bull. AAS*, **4**, 227.
———. 1972*c*, *Ann. N.Y. Acad. Sci.*, **194**, 17.
———. 1973, *Ap. J.* (*Letters*), **185**, L79.
Snyder, L. E., Buhl, D., Schwartz, P. R., Clark, F. O., Johnson, D. R., Lovas, F. J., and Giguere, P. T. 1974, *Ap. J.* (*Letters*), **191**, L79.
Soifer, B. T., and Hudson, H. S. 1974, *Ap. J.* (*Letters*), **191**, L83.
Solomon, P. M., and Klemperer, W. 1972, *Ap. J.*, **178**, 389.
Spitzer, L., Drake, J. F., Jenkins, E. B., Morton, D. C., Rogerson, J. B., and York, D. G. 1973, *Ap. J.* (*Letters*), **181**, L116.
Stecher, T. P., and Williams, D. A. 1974, *M.N.R.A.S.*, **168**, 23P.
Strom, K. M., Strom, S. E., Carrasco, L., and Vrba, F. J. 1975, *Ap. J.*, **196**, 489.
Sullivan, W. T. 1973, *Ap. J. Suppl.*, **25**, 393.
Sullivan, W. T., and Downes, D. 1973, *Astr. and Ap.*, **29**, 369.
Sume, A., Downes, D., and Wilson, T. L. 1975, *Astr. and Ap.*, **39**, 435.
ter Haar, D., and Pelling, M. A. 1974, *Rept. Progr. Phys.*, **37**, 481.
ter Meulen, J. J., and Dymanus, A. 1972, *Ap. J.* (*Letters*), **172**, L21.
Terzian, Y., and Balick, B. 1972, *Ap. Letters*, **10**, 41.
Terzian, Y., Dennison, B., and Balick, B. 1973, *Pub. A.S.P.*, **85**, 806.
Terzian, Y., and Parrish, A. 1973, *A.J.*, **78**, 894.
Thaddeus, P., Kutner, M. L., Penzias, A. A., Wilson, R. W., and Jefferts, K. B. 1972, *Ap. J.* (*Letters*), **176**, L73.
Thaddeus, P., Mather, J., Davis, J. H., and Blair, G. N. 1974, *Ap. J.* (*Letters*), **192**, L33.
Thaddeus, P., Wilson, R. W., Kutner, M., Penzias, A. A., and Jefferts, K. B. 1971, *Ap. J.* (*Letters*), **168**, L59.
Thompson, A. R., Colvin, R. S., and Hughes, M. P. 1969, *Ap. J.*, **158**, 939.
Townes, C. H. 1968, paper presented at Quantum Electronics Conference, Miami, Florida.
Troland, T. H., and Heiles, C. 1974, *Ap. J.*, **194**, 43.
Tucker, K. D., Kutner, M. L., and Thaddeus, P. 1973, *Ap. J.* (*Letters*), **186**, L13.
———. 1974, *ibid.*, **193**, L115.
Tucker, K. D., Tomasevich, G. R., and Thaddeus, P. 1971, *Ap. J.*, **169**, 429.
Turner, B. E. 1969*a*, *Ap. J.*, **157**, 103.
———. 1969*b*, *A.J.*, **74**, 985.
———. 1970, *Ap. Letters*, **6**, 99.
———. 1972*a*, *Ap. J.*, **171**, 503.
———. 1972*b*, *Nature Phys. Sci.*, **239**, 132.
———. 1973, *Ap. J.*, **186**, 357.
———. 1974, *Ap. J.* (*Letters*), **193**, L83.
Turner, B. E., Balick, B., Cudaback, D. D., Heiles, C., and Boyle, R. J. 1974*a*, *Ap. J.*, **194**, 279.

Turner, B. E., Buhl, D., Churchwell, E. B., Mezger, P. G., and Snyder, L. E. 1970*a*, *Astr. and Ap.*, **4**, 165.
Turner, B. E., Palmer, P., and Zuckerman, B. 1970*b*, *Ap. J. (Letters)*, **160**, L125.
Turner, B. E., and Zuckerman, B. 1974, *Ap. J. (Letters)*, **187**, L59.
Turner, B. E., Zuckerman, B., Fourikis, N., Palmer, P., and Morris, M. 1974*b*, *Bull. AAS*, **6**, 443.
Turner, B. E., Zuckerman, B., Palmer, P., and Morris, M. 1973, *Ap. J.*, **186**, 123.
Van Vleck, J. H. 1929, *Phys. Rev.*, **33**, 467.
Watson, W. D. 1974, *Ap. J.*, **189**, 221.
Watson, W. D., and Salpeter, E. E. 1972, *Ap. J.*, **175**, 659.
Weaver, H., Dieter, N. H., and Williams, D. R. W. 1968, *Ap. J. Suppl.*, **16**, 219.
Webster, W. J., and Altenhoff, W. J. 1970, *A.J.*, **75**, 896.
Weinreb, S., Barrett, A. H., Meeks, M. L., and Henry, J. C. 1963, *Nature*, **200**, 829.
Weliachew, L. 1971, *Ap. J. (Letters)*, **167**, L47.
Wendker, H. J. 1970, *Astr. and Ap.*, **4**, 378.
Werner, M. W., Elias, J. H., Gezari, D. Y., and Westbrook, W. E. 1974, *Ap. J. (Letters)*, **192**, L31.
Westerhout, G. 1969, Maryland-Greenbank Galactic 21-cm Line Survey (2d ed.; College Park, Maryland: University of Maryland).
Whiteoak, J. B., and Gardner, F. F. 1970, *Ap. Letters*, **5**, 5.
Willis, A. G. 1973, *Astr. and Ap.*, **26**, 237.
Wilson, R. W., Penzias, A. A., Jefferts, K. B., and Solomon, P. M. 1973, *Ap. J. (Letters)*, **179**, L107.
Wilson, T. L. 1970, *Ap. Letters*, **7**, 95.
———. 1972, *Astr. and Ap.*, **19**, 354.
———. 1973, *ibid.*, **25**, 329.
———. 1974, *ibid.*, **31**, 83.
Wilson, T. L., Mezger, P. G., Gardner, F. F., and Milne, D. K. 1970*a*, *Ap. Letters*, **5**, 99.
———. 1970*b*, *Astr. and Ap.*, **6**, 364.
Wilson, W. J., and Barrett, A. H. 1972, *Astr. and Ap.*, **17**, 385.
Wilson, W. J., Schwartz, P. R., Epstein, E. E., Johnson, W. A., Etcheverry, R. D., Mori, T. T., Berry, G. G., and Dyson, H. B. 1974, *Ap. J.*, **191**, 357.
Wilson, W. J., Schwartz, P. R., Neugebauer, G., Harvey, P. M., and Becklin, E. E. 1972, *Ap. J.*, **177**, 523.
Winnberg, A. 1970, *Astr. and Ap.*, **9**, 259.
Winnberg, A., Habing, H. J., and Goss, W. M. 1973, *Nature Phys. Sci.*, **243**, 78.
Winnberg, A., and Lundahl, L. 1970, *Astr. and Ap.*, **9**, 321.
Wurm, K. 1961, *Zs. f. Ap.*, **52**, 149.
Wynn-Williams, C. G. 1969, *Ap. Letters*, **3**, 195.
———. 1971, *M.N.R.A.S.*, **151**, 397.
Wynn-Williams, C. G., and Becklin, E. E. 1974, *Pub. A.S.P.*, **86**, 5.
Wynn-Williams, C. G., Becklin, E. E., and Neugebauer, G. 1972, *M.N.R.A.S.*, **160**, 1.
———. 1974*a*, *Ap. J.*, **187**, 473.
Wynn-Williams, C. G., Werner, M. W., and Wilson, W. J. 1974*b*, *Ap. J.*, **187**, 41.
Yngvesson, K. S., Cardiasmenos, A. G., Shanley, J. F., Rydbeck, O. E. H., and Elldér, J. 1973, Rept. No. P19, Dept. of Electrical and Computer Engineering, University of Mass., Amherst.
———. 1975, *Ap. J.*, **195**, 91.
Zuckerman, B. 1973, *Ap. J.*, **183**, 863.
Zuckerman, B., and Ball, J. A. 1974, *Ap. J.*, **190**, 35.
Zuckerman, B., Ball, J. A., Dickinson, D. F., and Penfield, H. 1969, *Ap. Letters*, **3**, 97.
Zuckerman, B., Buhl, D., Palmer, P., and Snyder, L. E. 1970, *Ap. J.*, **160**, 485.
Zuckerman, B., and Palmer, P. 1974, *Ann. Rev. Astr. and Ap.*, **12**, 279.
Zuckerman, B., and Turner, B. E. 1975, *Ap. J.*, **197**, 123.
Zuckerman, B., Yen, J. L., Gottlieb, C. A., and Palmer, P. 1972, *Ap. J.*, **177**, 59.

J. Elldér, Å. Hjalmarson, O. E. H. Rydbeck, and A. Sume: Onsala Space Observatory, S-43034 Onsala, Sweden

E. Kollberg: Research Laboratory of Electronics, Chalmers University of Technology, Fack, S-40220 Göteborg, Sweden

W. M. Irvine: Department of Physics and Astronomy, Astronomy—GRC Tower B, University of Massachusetts, Amherst, MA 01002